An investigation into full-ring radial-gap air-riding seals for aeroengines



Shubham Kumar

Department of Mechanical Engineering
The University of Nottingham

This dissertation is submitted for the degree of
Doctor of Philosophy

Department of Materials, Mechanics
and Structures

October 2019

I would like to dedicate this thesis to my grandparents, parents, and my wife …

Declaration

I hereby declare that except where specific reference is made to the work of others, the contents of this dissertation are original and have not been submitted in whole or in part for consideration for any other degree or qualification in this, or any other university. This dissertation is my own work and contains nothing which is the outcome of work done in collaboration with others, except as specified in the text and Acknowledgements. This dissertation contains fewer than 65,000 words including appendices, bibliography, footnotes, tables and equations and has fewer than 150 figures.

Shubham Kumar
October 2019

Acknowledgements

The research leading to these results was carried out at the Institute for Aerospace Technology (IAT), University of Nottingham and has received funding from the People Programme (Marie Curie Actions) of the European Union's Seventh Framework Programme (FP7/2007-2013). I am grateful to these organisations for providing me the funding and infrastructure to carry out this research work.

I would like to express my sincere thanks and gratitude to my supervisors Seamus Garvey and Hervé Morvan for their continued guidance and support throughout the course of this study. I truly appreciate their valuable inputs and guidance at each stage of this research.

I am also extremely thankful to my whole family for the different ways in which they have supported and guided me. I am also grateful to them for their unwavering faith in my abilities and their love, encouragement and motivation throughout this course of study.

Special thanks to my colleagues and friends at the IAT, especially Adrian Marinescu, Nicolas Schneider and Laura Pasquale, for always being eager to help me and for making my stay here so enjoyable.

Finally, I want to thank my wife, Shilpa, for her continued love and encouragement during the last three years. Thank you for always being there for me and looking after me.

Abstract

This thesis focuses on a study carried out for modelling, designing and testing a full-ring radial-gap air-riding seal configuration for applications in a Gas Turbine Engine.

On reviewing the open literature in the field of air-riding seals, it was realised that the majority of existing seal designs were axial-gap type seals. One of the key challenges faced by axial-gap seals is that they have to contend with the differential thermal growth of the engine parts which results in net motions of the order of 1 cm. A radial-gap seal would benefit from the lower net travel that it would need to accommodate. The existing radial gap seals are circumferential seals with segmented seal ring. The segmented seal ring design faces issues like leakage in between segments, improper mating of segments, rubbing between parts etc., as the seal ring is segmented. A full-ring design would eliminate these issues, but one of the key challenge for this seal will be maintaining a positive clearance with the rotor for all operating conditions.

This thesis discusses the design of a radial-gap seal, with a full-ring configuration. The characteristics of the thin fluid film in the seal was determined by carrying out 1-D and 2-D simulations. This helped in determining the stiffness coefficients of the fluid film. It was observed that most of the lift generated in the fluid film was by hydrostatic means. Studies carried out were able to confirm that a converging seal gap is necessary for achieving positive film stiffness.

Steady state CFD analyses of the fluid film were offset shaft positions to generate the stiffness matrix of the film. This was followed by coupled Fluid-Structure Interaction analyses to determine the damping coefficients and the response of the fluid film to different shaft excitations.

The 3 analysis methods were found to have good correlation with each other in predicting the seal performance for different operating conditions. There was some discrepancy found in the experimental test data which meant that the experimental stiffness values did not correlate well with the simulation results, which, among other factors, might have been caused due to manufacturing error or faulty installation.

Nomenclature

ρ	Density of the fluid
u	Velocity along X
v	Velocity along Y
w	Velocity along Z
μ	Dynamic viscosity
L	Total seal length
W	Width of the seal
h_1	Height of first step
h_n	Height of n^{th} step
P_{in}	Inlet Pressure
P_{out}	Outlet Pressure
g_x	Acceleration due to gravity along X
g_y	Acceleration due to gravity along Y
g_z	Acceleration due to gravity along Z
Q	Volumetric flow rate
P_1	Pressure at step inlet

P_2	Pressure at step outlet
$\dot{m}$	Mass flow rate
D	Shaft diameter
K	Stiffness
ΔF	Lift force
Δδ	Offset
Kn	Knudsen number
λ	Mean free path
k_b	Boltzmann constant
h	Seal height
R_g	Gas constant
T	Temperature
L*	Characteristic length
Λ	Speed number
M	Mass matrix
C	Damping matrix
K	Stiffness matrix
F	Force vector
M_c	Critical mass

κ_{eq}	Dynamic damping stiffness
$\bar{\omega}$	Whirl frequency
E	Internal energy
k	Turbulent kinetic energy
ε	Dissipation rate
Ω_{mean}	Mean shaft angular velocity
ν_{shaft}	Damped natural frequency of shaft
ς	Damping ratio
A	Amplitude
Y_{shaft}	Specified shaft displacement in Y
Z_{shaft}	Specified shaft displacement in Y
ω_{seal}	Seal natural frequency
Ω_{max_shaft}	Max. shaft unbalanced frequency
$k_{air\text{-}film}$	Stiffness of the air-film
m_{seal}	Mass of the seal
k_{eff}	Effective stiffness
$k_{sec\text{-}seal}$	Secondary seal stiffness
k_{shaft}	Shaft stiffness
ω_{avg}	Average frequency

Table of contents

List of figures **xv**

1 Introduction **1**

1.1 Research Motivation 4

1.1.1 An overview on face seals and the challenges involved in aero-engine application 4

1.1.2 An overview on circumferential seals and their shortcomings 5

1.1.3 A discussion on full-ring radial-gap seal: Expected advantages, challenges and limitations 6

1.2 Objectives 8

1.3 Novel contributions 8

1.4 Thesis structure 9

2 Literature Review **11**

2.1 Seals 11

2.2 Air-Riding Technology 15

2.3 Air-Riding Seals 17

2.3.1 Face Seals 17

2.3.2 Circumferential seals 22

2.4 Modelling Air-Riding Fluid Films 25

2.5 Summary 28

3 1-D and 2-D Analysis of the Thin Fluid Film **31**

3.1 Seal Geometry and Seal Assembly Schematics 31

3.2 1-D Analysis 33

3.2.1 1-D Numerical Modelling 35

3.3 2-D Analysis 40

3.3.1 Reynolds Equation for Fluid Film Modelling 41

3.3.2 Numerical Modelling of the Reynolds Equation model 43

3.3.3 Stiffness Matrix 49

3.3.4 Dynamic Coefficients of the fluid film 52

3.4 Summary and Discussion 52

4 CFD Modelling - Overview and Verification Study **55**

4.1 Flow Equations 55

4.1.1 Overview 55

4.1.2 Continuity Equation 56

4.1.3 Momentum Equation 56

4.1.4 Energy Equation 57

4.2 Turbulence Modelling 57

4.2.1 The Reynolds-Averaged Navier-Stokes (RANS) Equations 57

4.2.2 The $k-\varepsilon$ model 59

4.2.3 The RNG $k-\varepsilon$ model 60

4.2.4 The $k-\omega$ model 61

4.2.5 The SST $k-\omega$ model 62

4.2.6 Near Wall Modelling 63

4.3 Preliminary Modelling and Verification Study 64

4.3.1 Grid Independence Study 67

4.4 Summary and Discussion 70

5 CFD Modelling - Steady State and Transient Analyses 71

5.1 Steady-State Analysis 72

5.1.1 Fluid Domain Settings 72

5.1.2 Solver Settings 73

5.2 Steady-State Simulation Results 74

5.3 Stiffness Matrix 77

5.4 Fluid-Structure Interaction Analysis 78

5.4.1 Study-1: Response to Shaft Motions 78

5.4.2 Study-1: Results 80

5.4.3 Direct Stiffness and Damping Coefficients 85

5.4.4 Study-2: Petal Curve Study 86

5.4.5 Study-2: Results 88

5.4.6 Dynamic Coefficients of the fluid film - 2 93

5.5 Comparison between 1-D, 2-D and CFD analyses 93

5.6 Summary and Discussion 96

6 Seal Design and Experimental Results 99

6.1 Routh-Hurwitz Stability Analysis 99

6.2 Whirl Frequency Ratio 102

6.3 Practical Operability Criteria for Dynamic Operation 102

6.4 Seal System Design 105

6.5 Integrated Test-Rig 110

6.6 Experiment-1: Weight Test 112

6.6.1 Methodology 113

6.6.2 Observation 114

6.6.3 Conclusion 120

6.7 Experiment-2: Strike Test 121

6.7.1 Methodology 122

6.7.2 Observation 122
6.7.3 Conclusion 124
6.8 Summary and Discussion 126

7 Conclusions and Suggested Future Research 127
7.1 Conclusions 127
7.2 Suggested Future Research 130

References 133

Appendix A Appendix 139

List of figures

1.1 Seal locations for Fan and HPC in a typical Gas Turbine Engine 2

1.2 Seal locations for Turbine in a typical Gas Turbine Engine 2

1.3 Schematic diagram of a typical face seal 4

1.4 Schematic diagram of a typical circumferential seal 5

1.5 Envisaged design of a full-ring radial-gap air-riding seal 7

2.1 Geometry of a convergent type stepped labyrinth seal 12

2.2 Waukesha brush seal used in aero-engines 14

2.3 Schematics of a gas bearing 15

2.4 Spiral groove seal developed by Pennink 18

2.5 Schematics of the seal developed by Garrison and McNickle 21

2.6 Segmented seal ring in Stein's design 22

3.1 Seal assembly schematic 32

3.2 Seal gap geometry 33

3.3 Seal nodes 35

3.4 Fitted curve on the pressure-difference data 37

3.5 Pressure variation across the seal 37

3.6 Shaft off-centred by an amount δ 38

3.7 Pressure profiles for the centred and off-centred shaft, and variation of lift force generated across the seal length when the shaft is off-centred by 2μm . 39

3.8 Geometry of the air film 42

3.9 Discretisation method for the Finite Difference model 44
3.10 Pressure boundary condition applied to the finite difference model 46
3.11 Pressure profile of the fluid film for a non-rotating and centred shaft 47
3.12 Pressure profile of the fluid film when the shaft is static and it is off-centred by 5 µm 47
3.13 Pressure profile of the fluid film for a centred shaft rotating at 10000 rpm . . 48
3.14 Pressure profile of the fluid film when the shaft is rotating at 10000 rpm and it is offset by 5µm 48
3.15 Comparison of the axial pressure drop obtained from the 1-D and 2-D analysis 49
3.16 Variation of film stiffness with increasing pressure ratio 51
3.17 Variation of film stiffness with varying seal outlet height for a pressure ratio of 4 51

4.1 Simplified fluid and structural model set-up in ANSYS Design Modeler . . 65
4.2 Structured hexahedral meshing of the fluid domain 66
4.3 Zoomed-in view showing the mesh at the interface between seal air-film outlet and the outlet volume 66
4.4 Variation of mass flow rate at the inlet and outlet through the steady state CFD simulation 68
4.5 y^+ values on the seal air-film surface 69
4.6 Variation of direct film stiffness with inlet temperature 70

5.1 Boundary conditions for the CFD simulations 72
5.2 Velocity variation across an axial section of the full seal assembly 74
5.3 Zoomed-in view of the velocity contour at the seal outlet 75
5.4 Pressure variation near the seal outlet 75
5.5 Comparison of the the pressure variation plots evaluated from 1-D, 2-D and CFD analysis 76
5.6 Resultant displacement from F_{ext} applied along Y 81
5.7 Displaced mesh during a transient timestep 81

5.8 Fitted curve on the plot of the calculated displacement values 82
5.9 Fitted curve for 200Hz 83
5.10 Fitted curve for 1kHz 83
5.11 Fitted curve for 1.5kHz 84
5.12 Fitted curve for 2kHz 84
5.13 Petal curve traced by the shaft 86
5.14 Petal curve - shaft displacement plots along Y and Z 87
5.15 Resultant force along Y and Z for shaft displacements governed by the petal equation (for 2 cycles) 88
5.16 Comparison of $F_{Y petal}$ and $F_{Z petal}$ (for 2 cycles) 89
5.17 Comparison between the actual force values and the fitted model (for 2 cycles) 91
5.18 Comparison between the actual force values and the fitted model (for 3 cycles) 91
5.19 Comparison between the actual force values and the fitted model (for 4 cycles) 92
5.20 Comparison between the actual force values and the fitted model (for 2 cycles) 93
5.21 Comparison between stiffness values from 1-D, 2-D and CFD analyses for varying seal outlet height, for a pressure ratio of 4, shaft rotation speed of 10000 rpm and a fixed seal inlet height of 50 μm 94
5.22 Comparison between stiffness values from 1-D, 2-D and CFD analyses for varying pressure ratio, for a fixed shaft rotation speed of 10000 rpm and a seal inlet and outlet height of 50 μm and 14 μm respectively 94
5.23 Comparison between stiffness values from 1-D, 2-D and CFD analyses for varying shaft rotation speeds at 4 bar, for a seal inlet and outlet height of 50 μm and 14 μm respectively 95

6.1 Schematic of the seal-shaft system 103
6.2 Seal ring design 106
6.3 Seal ring design - front and back view 106
6.4 Schematic of the bellows 107
6.5 Secondary seal- bellows and flexure arrangement 108
6.6 Seal system assembly (model) 108

6.7 Outlet chamber 109
6.8 Seal Assembly 110
6.9 Test-rig model 111
6.10 Test-rig assembly 111
6.11 Weight test 112
6.12 Weight test - sensor and sensor mount 113
6.13 An exaple of the curve fit excercise, for a pressure of 2 bar 116
6.14 Variation of measured stiffness with angular position of the shaft 117
6.15 Variation of measured stiffness with angular position of the shaft 117
6.16 Weight test - Seal adapter pulled out 118
6.17 Comparison between the simulation and experimental results, for determining shaft stiffness 119
6.18 Variation of air-film stiffness with shaft angular position 120
6.19 Solenoid striker used to strike the seal ring 122
6.20 Sensor Holders and solenoid striker used for the strike test 123
6.21 Strike Test - readings from the sensor 123
6.22 Strike Test - Sensor readings (zoomed-in on one of the strikes) 124
6.23 Strike Test - Truncated data 125
6.24 Strike Test - Fourier Transform 125

A.1 Sensor spedification data 139
A.2 Solenoid Specification 140

Chapter 1

Introduction

The aviation industry has been one of the most prolific sectors of development over the last two decades. According to Boeing's Current Market Outlook [1], passenger traffic as measured by revenue passenger kilometers (RPK) is expected to rise by 4.8% each year for the next two decades, thus leading to a need for over 39,600 airplanes valued at more than $5.9 trillion. The rise in aircraft demand would also imply a significant rise in aero-engine demand to power these aircraft.

Most of the aero-engine manufacturers are in pursuit of technologies that show promise of high performance to cost benefit ratios. To achieve the lower Specific Fuel Consumption (SFC) desired for the next-generation engines, more progress must be made in increasing core efficiencies. Better core efficiencies can be obtained by high cycle pressure ratios and compressor exit temperature, higher turbine inlet temperature, and improved component efficiencies including better sealing and secondary air flow management.

In a modern aircraft gas turbine engine there are numerous sealing locations, all of which are significant with respect to the performance and reliability of the engine. The types of seal locations may be classified into two broad categories:

1. The mainshaft seals - The primary function of these seals is to protect the bearing compartments from the potentially damaging outside engine environment. Generally positive contact seal designs are used as mainshaft seals, though sometimes non-contacting labyrinth seals may be employed.

2. The gas path seals - These seals, generally non-contacting (like labyrinth seals), are used to reduce loss of high pressure gas from the engine cycle, control the cooling air

flow through the hot section of the engine, and to maintain pressure balance on the rotor shaft system.

Another extremely important sealing location where gas path seals are utilised are the outer gas path seal locations over compressor and turbine blade tips. The outer gas path seals are intended to maintain close operating clearance between the rotating blade tips and the stationary seal components, thereby improving engine efficiency. Fig.1.1 and Fig.1.2, respectively, show the sealing locations (indicated by arrows) in the Fan & Compressor, and the Turbine stage of a Gas Turbine Engine.

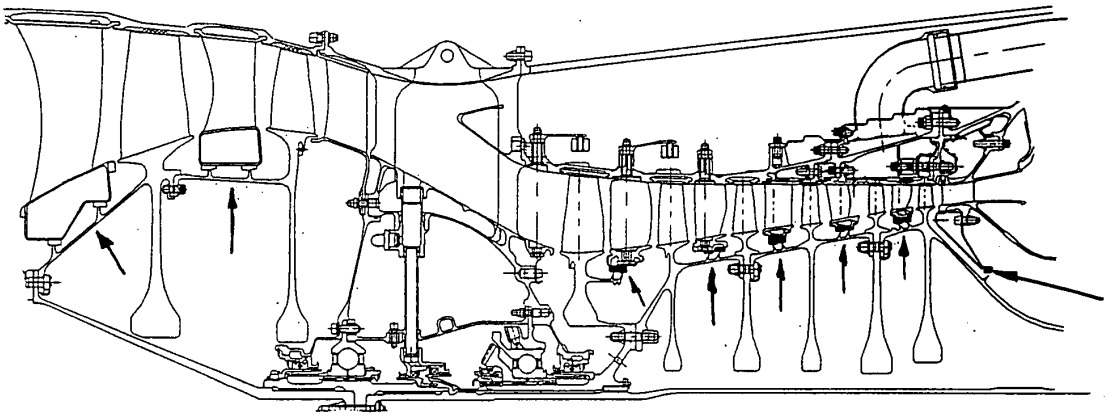


Fig. 1.1 Seal locations for Fan and HPC in a typical Gas Turbine Engine [2]

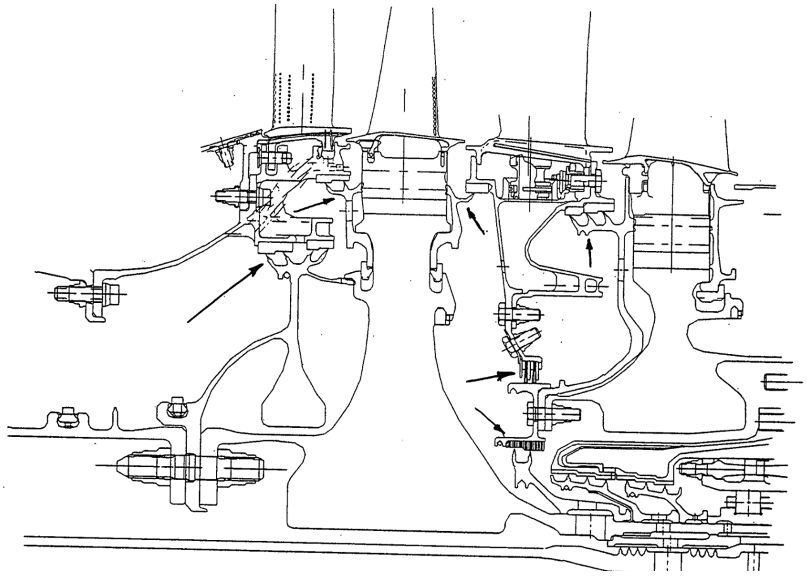


Fig. 1.2 Seal locations for Turbine in a typical Gas Turbine Engine [2]

Higher levels of compressor exit and turbine inlet temperature are key to both military and civilian advanced engine programs. Air bled from the engine is used to cool critical high temperature components particularly in the turbine. However, diverting this air to cool engine hardware rather than using in the engine cycle reduces thrust levels, lowers component efficiencies and adversely affects turbine inlet temperatures. Therefore, it becomes critical to minimize the amount of cooling air used for the turbine. This problem is compounded by the issue of coolant leakage, which results in both higher amounts of flow being bled off than is required for cooling, as well as a drop in the supply requirements for the hardware. This indicates that, in order to function properly, the ability to provide and maintain sealing throughout the engine is essential.

Advanced engine seals show promise of reducing engine losses and maintaining their performance benefits over the service interval of the engine. Studies performed by Stocker *et al.* [3] estimated that making the same performance improvements by improving seal technology would cost 4 to 5 times less than that brought about by improving the compressors or turbines by other means.

Aircraft engine manufacturers are now aiming for Operating Pressure Ratios (OPRs) in excess of 70:1 and operating speeds of up to 20,000 revolutions per minute (rpm) for future aircraft. Hence, the demands imposed by future technologies require seals that can maintain clearances of a few microns (for minimising the leakage) whilst being able to operate in these demanding conditions. Air-riding seals show promise of satisfying these requirements and hence they have emerged as potential sealing solutions for the next-generation aircraft engines.

Air-riding seals utilise a thin film of air to separate rotor and stator faces, and provide an effective sealing by minimising the flow of air between locations experiencing differential pressures. Most of the prior art in the field of air-riding seal comprises of axial gap seals (or face seals, as they are popularly called) and segmented ring-type radial seals (or circumferential seals). A detailed literature review of the prior-art and state-of-the-art in the field of air-riding seals has been presented in Chapter 2.

1.1 Research Motivation

1.1.1 An overview on face seals and the challenges involved in aero-engine application

Earliest face seal designs emerged in 1970s (Dobek's face seal designed in 1973 [4]) and there are evidences of their application in pipeline and process industries by mid 1980s. Fig. 1.3 shows the schematic diagram of a typical face sealing arrangement. A face seal is designed to obstruct or prevent gas from escaping from one region to another through a gap between the stator and rotor mating faces (shown as *Sealing dam* in Fig. 1.3). The performance of such a seal depends greatly on the clearance between the mating faces. A smaller gap between the faces allows less leakage and yields a better sealing performance, but zero gap (or contact between the rotor and stator) can prove detrimental because either the seal faces wear severely or it leads to seizure.

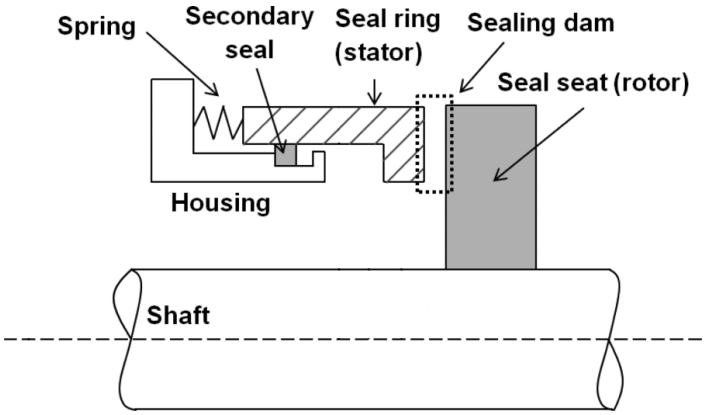


Fig. 1.3 Schematic diagram of a typical face seal [5]

The first efforts in designing face seals for gas turbine engines were recorded in early 1990s (as seen in the designs of Lahrman and Hwang *et al.* [6, 7]). However, some technical challenges were encountered during incorporation of air-riding face seals in gas turbine engines.

For aero-engine applications, typically a seal gap of less than 75 microns must be maintained in face seals (less than 20 microns for hydrodynamic seals). Such a specification must be met notwithstanding seal vibration, its aeroelastic interaction with the air film, thermal expansion, large deformations due to shaft motion and relative movement between various components. Studies carried out by Munson and Pecht [8] indicated that a number of seals failed due to contact occurring between seal faces. Gardner's paper [9] on high-speed,

high-temperature compressor discharge seal gives a good overview of previous experimental work on face seals and highlights the challenges associated with face seals for gas turbine application.

So, on reviewing the prior-art in the field of face seals it becomes quite evident that one of the key challenges faced by axial-gap seals in aero-engine application is maintaining the seal gap in expected operating conditions during normal operation of a gas turbine engine, including but not limited to differential thermal growth, seal vibrations, aeroelastic interactions etc., which can cause net motions of the order of 1 cm. This results in an added complexity in designing the seal components for aero-engine face seals. In this aspect, a radial-gap seal would have an added advantage over an axial-gap seal as it would benefit from lower net motions of engine parts, but one of the key challenges for these seals will be that they will have to contend with the unbalance vibrations.

1.1.2 An overview on circumferential seals and their shortcomings

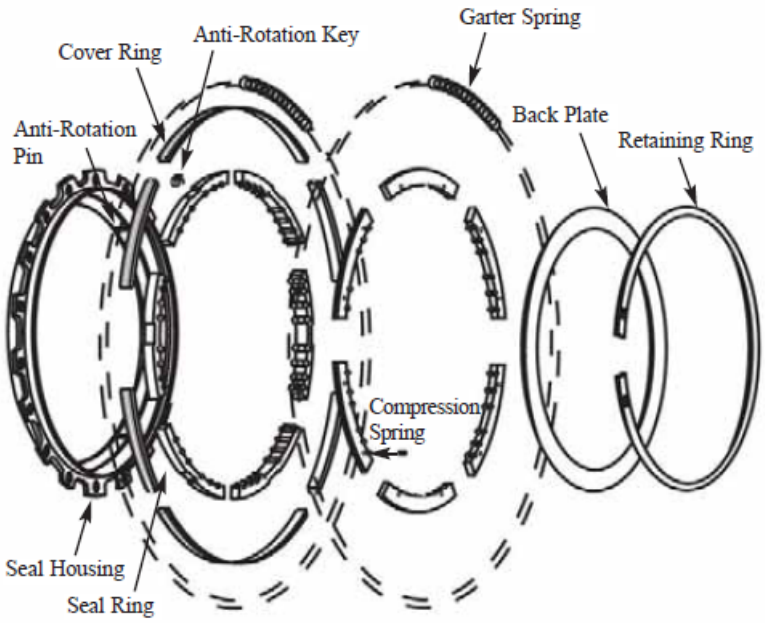


Fig. 1.4 Schematic diagram of a typical circumferential seal [10]

Circumferential seals or segmented seals are a generic type of sealing devices which primarily consist of a plurality of bow-shaped carbon material segments arranged circumferentially in abutting relationship to form a continuous ring which opposes a corresponding circumferential surface of a runner, thereby forming a seal or rubbing interface. In the

conventional circumferential sealing arrangement, as shown in Fig. 1.4, two segmented non-rotating carbon rings are secured to the seal housing structure, which are urged into contact with the outer circumferential surface of the runner by respective garter springs. The runner is connected to the main shaft and rotates therewith. Each garter spring encircles the outer diameter of the carbon segments of the respective sealing ring and provides a radially inwardly directed force. The carbon segment ends contain overlapping tongue and socket joints to restrict leakage at the end gaps.

Stein developed one of the first kind of circumferential seals in 1978 when he invented the segmented-ring type seal design [11]. One of the known issues with Stein's segmented-ring type seal design was the leakage along the radial path between adjacent segment, especially under certain specific operating conditions like employing the seal to operate in a pressurised oil mist atmosphere. Although the leakage between the segments was reduced in subsequent designed improvements, as shown in Borkiewicz's and Hwang's designs [12, 13], several other issues (like complexity in designing parts, differential thermal growth between parts, improper mating of ring segments during some operating conditions etc.) were identified in these seals which limited the utilisation of circumferential seals to a very few locations in aero-engines.

1.1.3 A discussion on full-ring radial-gap seal: Expected advantages, challenges and limitations

A full-ring radial-gap air-riding seal will use a continuous-ring as a seal ring to close the radial gap between the rotor and stator. In general, a radial-gap air-riding seal has an added advantage over axial-gap seal as the net motions of engine arts that it has to contend with is much lower as compared to axial-gap seals. A radial-gap seal can also be employed in many more locations in aero-engines. Segmented-ring seals have been widely used radial-gap seals in aero-engines, but added design and manufacturing complexity associated with the segmented design limits its application in aero-engines. A full-ring radial-gap air-riding seal will eliminate some key challenges encountered in the segmented-ring design, like leakage between the adjacent segments and improper mating of segments. It is expected that it will need less maintenance and it will have a longer operating life as compared to the segmented-ring design as it will not have to contend with the wear and tear in seal ring segments.

In spite of numerous design solutions in air-riding seals that various authors have explored, the literature does not provide any evidence of a full-ring radial-gap air-riding seal that has

been designed or analysed. One of the key challenges for a full-ring seal design will be maintaining a positive clearance from the rotor for all operating conditions. This implies that the air film between the rotor and seal ring should have sufficient stiffness to allow the seal ring to follow the rotor during its radial movement. Any contact between the rotor and the seal ring will cause wear and tear to the seal ring and substantially affect the seal performance. So maintaining a positive, yet low clearance ($\leq$ 20 µm), for the full-ring seal design during radial movement of the rotor is bound to be very challenging. The design of the supporting structure (or the secondary seal) will also play a key role in the seal design as it should not only be able to support the seal ring and withstand the flow of high pressure air, but also have a lower radial stiffness than the air film. The numerical modelling of air-riding seals might prove to be a formidable challenge as well as the analysis must be able to represent the dynamics of the fluid-structure interaction. It is also worth noting that although air-riding seal designs have been the subject of a large number of publications, broadly speaking, the research papers are either dedicated to the understanding of a particular failure mechanism, or they report detailed experimental observations for a class of seals. The absence of any record of a full-ring radial-gap air-riding seal design in open literature might be due to any of the above-mentioned factors.

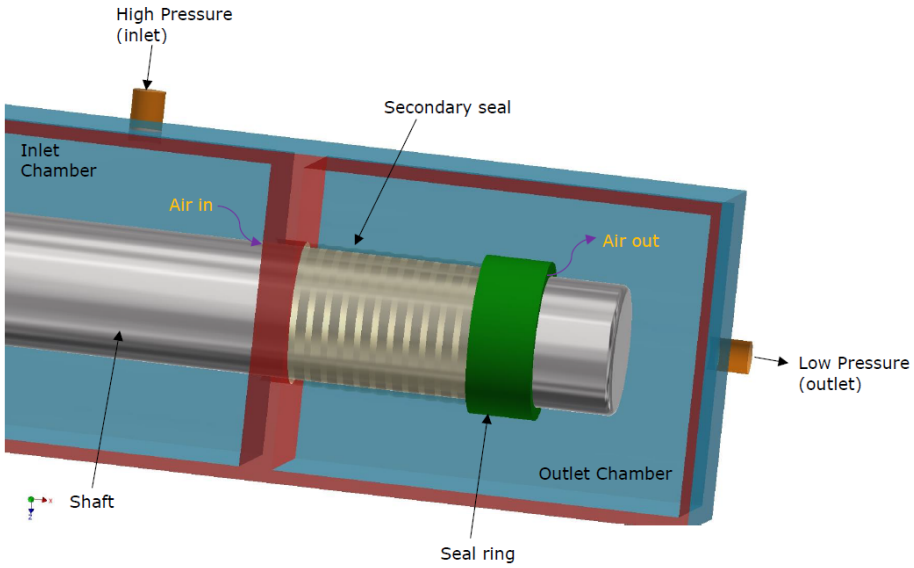


Fig. 1.5 Envisaged design of a full-ring radial-gap air-riding seal

Fig. 1.5 shows a model of the envisaged design of a full-ring radial-gap air-riding seal. High pressure air from a compressor is fed into the inlet chamber through the inlet port. The pressurized air then passes through the secondary seal and seal-ring to the outlet chamber, and

finally exits through the low pressure outlet port. The secondary seal arrangement supports and guides the primary seal ring along its axial and radial movements.

1.2 Objectives

The work presented in this thesis is aimed at developing a full-ring radial gap air-riding seal, and exploring the viability of utilising these seals for applications in an aircraft engine. The research objectives were laid out as follows:

1. Developing the modelling capability to predict the performance of this new category of seals.
2. Analysing the stability of the seal during its operation by evaluating its rotordynamic coefficients
3. Designing the seal and carrying out some rudimentary testing of the seal

1.3 Novel contributions

On reviewing the prior-art and the state-of-the-art in the field of air-riding seals, no evidence of a full-ring radial-gap air-riding seal was found in the open literature. So the primary focus of the work presented in this thesis was to assess the feasibility of developing a full-ring radial-gap seal for aero-engine application.

A novel kind of radial-gap air-riding seal, with a full-ring configuration, was designed. 1D and 2D analyses of fluid-film was carried out to determine the performance of the seal and evaluate the stiffness of the fluid-film. Fluid-Structure Interaction (FSI) analysis of the rotor-stator system was carried out through coupled CFD-Mechanical simulations in two different FSI studies to understand the transient behaviour of the air-film to shaft movements. The results from the FSI studies were analysed to evaluate the rotordynamic coefficients of the fluid film, which was then compared against 1D and 2D results. Stability analysis of the seal was carried out to verify if the seal system is stable. The novel radial-gap air-riding seal system was then designed, along with the test-rig, and the experimental results were compared against the simulation results.

1.4 Thesis structure

This section describes the overall structure of the thesis. It catalogues all the chapters of the thesis and gives a brief description of the contents of each chapter.

1. **Chapter 1 - Introduction:**
   This chapter gives a brief introduction about the research project, underlining the need to carry out a structured research work on a novel sealing technology which can be effectively employed in future GTEs. It outlines the aims & objectives of the project, and lists the novel contribution from the research project.

2. **Chapter 2 - Literature Review:**
   This chapter investigates the prior art in the field of gas bearings and air-riding technologies, with emphasis on air-riding seals. Some thin film modelling techniques for bearings and gas seals are also discussed.

3. **Chapter 3 - 1-D and 2-D Analysis of the Thin Fluid Film:**
   This chapter describes the seal ring geometry and presents 1-D and 2-D modelling techniques for modelling the fluid film. Poiseuille's flow equation is derived from the Navier-Stokes equations and it is then used to generate the pressure profile through the seal. Compressible form of Reynolds equation is solved using a finite difference modelling approach to carry out a 2-D analysis of the fluid flow through the full seal geometry. Stiffness coefficients of the fluid film are evaluated based on small perturbation technique.

4. **Chapter 4 - CFD Modelling - Overview and Verification Study:**
   Chapter 4 is dedicated towards understanding the underlying concepts in a CFD simulation. This chapter also discusses about the details of the verification study carried out for establishing grid independence of the simulation model.

5. **Chapter 5 - CFD Modelling - Steady State and Transient Analyses:**
   Chapter 5 gives a detailed description of CFD simulations carried out to analyse the performance of the thin film. CFD simulation for the full seal geometry is carried out on ANSYS CFX. The full set-up of the ANSYS CFX model is explained in detail. Steady state analyses are carried out to understand the fluid film characteristics, followed by coupled ANSYS CFX-Mechanical transient analyses to understand the stiffness and damping coefficients of the system by carrying out a 2-way Fluid-Structure Interaction (FSI) analysis. FSI analysis is also used to determine the frequency response of the fluid film to shaft perturbations.

6. **Chapter 6 - Seal Design and Experimental Results:**
   This chapter analyses the stability of the seal during its operation. It also gives a detailed description of the design of the full seal system and set-up of the test rig designed to test the performance of the seals. Results from the some preliminary experiments are also discussed in this chapter.

7. **Chapter 7 - Conclusion and Suggested Future Research:**
   The final chapter is dedicated to describing the conclusions drawn from the project and exploring the possibilities of future research work arising from the results of this research.

Chapter 2

Literature Review

The motivation of the research and the objectives of the project were discussed in Chapter 1. This chapter provides a detailed overview of different sealing technologies and identifies gap in the literature that could be explored during this research.

2.1 Seals

Seals can be broadly subdivided in two categories:

- Static Seals, where there is no relative motion between the two sealing surfaces
- Dynamic Seals, where sealing takes place between surfaces which have a relative motion with respect to each other, e.g. rotary movement of a shaft relative to a housing, or reciprocating movement of a rod piston in a cylinder.

As this project investigates the viability of developing a novel kind of seal for gas turbine machinery, which seals the radial gap between a rotor(shaft) and a stator(casing), the scope of this study has been limited to the study of dynamic seals used in gas turbine engines.

Dynamic seals can be further subdivided into two main categories, as described by Warring [14] :

- Contacting seals, where the seal bears against its mating surface under positive pressure
- Clearance seals which operate with a positive clearance

Perhaps the most widely used clearance type seal in the aviation industry is the labyrinth seal. Labyrinth seals operate with positive clearance and provide sealing by virtue of a

lengthy, torturous gap path. A labyrinth seal generally constitutes of a series of cavities formed along the adjacent surfaces of two members which have a relative motion with respect to one another. At successive steps along the seal, the adjacent surfaces of these rotatable members are situated in close proximity to each other in such a way that they form annular slit-like orifices. Pressure energy of a fluid is converted into velocity energy as the fluid is forced to pass through the narrow orifices and as the fluid enters the larger cavities, velocity of the fluid is dissipated as turbulence. Fig. 2.1 shows the geometry of a convergent type stepped labyrinth seal.

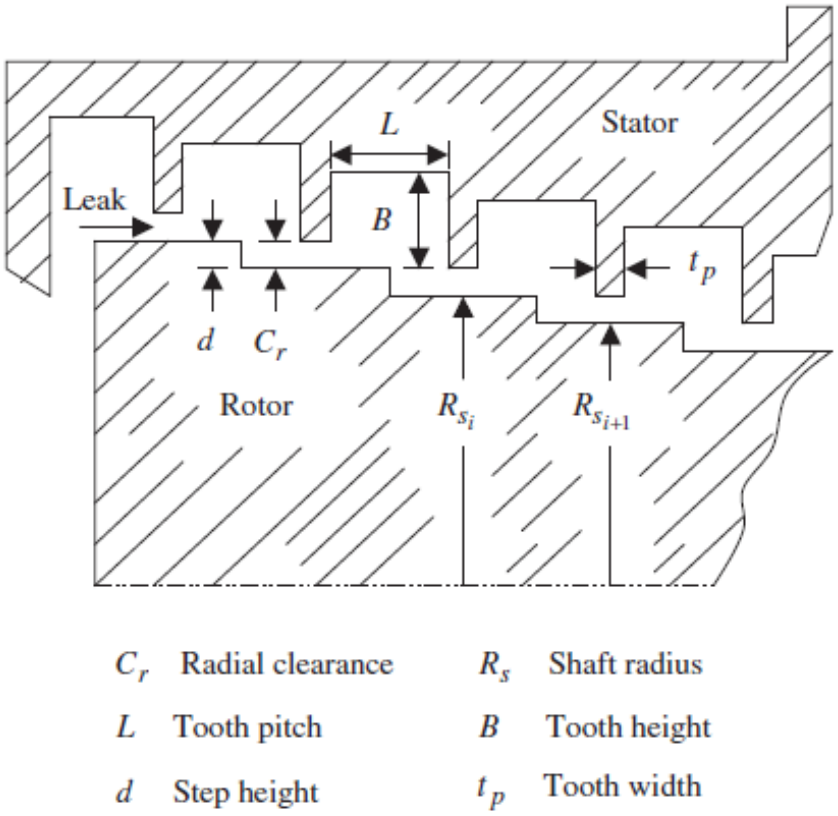


Fig. 2.1 Geometry of a convergent type stepped labyrinth seal

Since 1924, when the labyrith seal was first developed by Charles and Alfred [15], it has been extensively used in a wide range of turbomachinery, including Gas Turbine Engines (GTEs). One of the major challenges for successful operation of labyrinth seals in GTEs is to provide positive clearance during all points of engine operation. So, the radial clearance needs to account for thermal expansion, shaft vibrations, runouts etc., but an increase in clearance comes at an expense of increasing the leakage flow [16]. Many contemporary labyrinth seals have been quite expensive to produce due to the intricate machining required

to finish each sealing surface. Such complex sealing surfaces have also been somewhat fragile and thus prone to failure in rigorous application. The size of the gap within a labyrinth seal is proportional to the diameter of the seal, typically resulting in more leakage and lower efficiency as the size of the seal increases [17].

Clearance in a labyrinth seal can be reduced by making use of an abradable labyrinth seal. Abradable labyrinth seals are rotoric labyrinth seals in which the stator-like portion that opposes the rotoric teeth is formed of an abradable material. Although small clearances in both the labyrinth seals in stator and rotor can reduce leakage, they also negatively influence rotor stability due to inlet swirl at the entrance to the labyrinth seal and circumferential flow created inside the labyrinth seal by centrifugal force due to rotation [18]. Stepped labyrinth seals were developed in 1980s to further reduce their leakage rate through the labyrinth seal and to improve its efficiency. The advantage of the stepped seal is obvious when the clearance is large but the advantage significantly diminishes when the clearance is very small. As the marginal performance gain over the straight seal cannot sufficiently justify the increased fabrication cost, the application of the stepped seal does not seem very feasible in instances where the running clearance needs to be very small [19]. Labyrinth seals are also prone to develop cross-coupled forces with the potential of inducing rotordynamic instability [20]. Moreover, labyrinth seals by design include significant redundancies, which greatly increase the weight of larger diameter turbines. While these seals have been in use for many years, they have reached their limit in terms of leakage reduction. In addition, it is now generally recognized that their performance deteriorates over time, resulting in ever increasing flow leakage over the life of the seal.

The most commonly used contacting type seal in aviation industry is the brush seal. Brush seals improve power and efficiency in turbomachinery by overcoming the limitations associated with labyrinth seals. Typically a brush seal comprises of a stack of resilient bristles that are fixed to one of the components and are in a sliding relationship with the other component. One of the first brush seals was developed in 1959 by R.O.Peterson [21], whereby this novel kind of seal was envisioned for various annular relative movement applications, like in bearings. Adaptability of brush seals in managing the air flows inside a gas turbine engine was illustrated in [22–24]. In 1998, Skinner *et al.* [25] demonstrated the possibility of having a combined brush-labyrinth seal by retrofitting brush seals into labyrinth seals segmented for movement radially by spring or pressure forces.

The primary limitation of conventional brush seals is the excessive bristle wear, which was identified by Proctor *et al.* [27]. They also exhibit localised heat generation during shaft rotation [28] and they have an inherent inability to withstand high pressure differentials. The

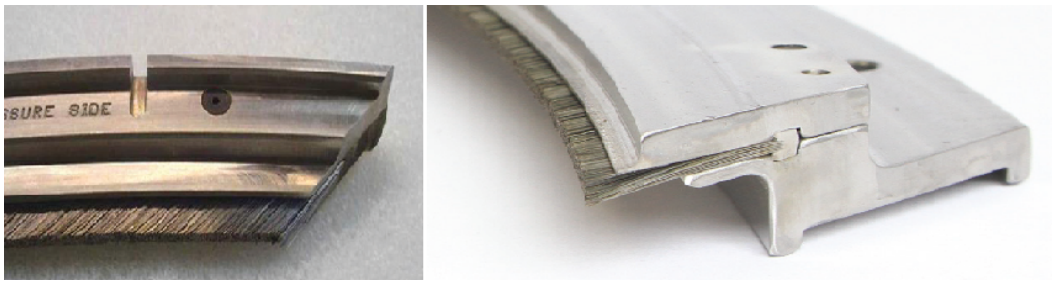


Fig. 2.2 Waukesha brush seal used in aero-engines [26]

pressure and temperature considerations limit the applicability of the seals to compressor and turbine interstages in a GTE. They also exhibit accelerated wear during transients and the brush wires are susceptible to high cycle fatigue and creep.

Wearing of seals is a very important factor which affects an engine's Mean Time Before Failure (MTBF). Though non-contacting seals are not intended to rub during operation, engine structural distortions, thermal response effects, and dynamic loads inevitably lead to transient rub interactions between seal components. Wear to the tips of high pressure turbine blades can initiate sites of rapid corrosive attack to the blade through disruption of protective blade coatings. In the compressor, rapid heating of titanium alloy blade tip during adverse rub interactions can potentially lead to severe thermal damage.

Future gas turbine engine designs would subject fluid seals to a far more hostile environment, in terms of greater pressure differentials, higher temperatures, larger seal diameters and increased velocity of the rotor. Seal clearances would then have to be increased to account for manufacturing tolerances, possible eccentricity of the members, and material growth due to temperature and centrifugal loading. This would lead to excessive fluid leakage in a labyrinth and brush seals, which in turn would decrease the efficiency of the engine and increase SFC. If these seals are employed near the engine bearing chamber to restrict leakage of high temperature working gas into engine bearing compartments or sumps, any lubricating oil in or near the seal can produce coke build-up which further degrades seal effectiveness.

As there is little scope for significant improvements in existing seal designs of these seals (labyrinth and brush), and with increased efficiency requirements for future seal technologies, new seal technologies are being investigated which would be able to operate in increasingly demanding working environments.

Air-riding seals show the promise of meeting the sealing requirements for future aircraft engines. In order to develop an understanding of these seals, it is important explore the literature on air-riding technology.

2.2 Air-Riding Technology

In the last 3-4 decades, air-riding technology has been successfully used in a range of different applications. On exploring the literature about this technology, it was interesting to note that this technology has been referred-to as different names by different authors. Some of the common terminology used are film-riding, gas-lubricated and non-contacting. The bearings utilising air-riding technology are generally called air bearings or gas bearings. The term squeeze-film can also be found in the literature, usually used for squeezed-film dampers or bearings. Gas film bearings have been successfully employed in many commercial applications, such as navigation systems, computer disk drives, high-precision instruments and sensors, turbocompressors etc.

In spite of the varied applications of this technology, from small scale precision engineering environments [29] to large scale gas turbine engines [30], the underlying principle that characterises the formation and dynamics of the thin film are very similar.

Gas bearing technology was first developed in the 1960's to support high speed rotating shaft systems that could not be operated using conventional oil-lubricated bearings [31]. Gas bearings are also extremely useful when used with precision instruments, because of their low noise and near-zero friction characteristics. Compared with oil bearings, gas bearings have less heat generation, lower contamination, and higher accuracy [32]. The main disadvantage of gas bearings is their low load carrying capacity and low damping ratios, which often limits the range of their application.

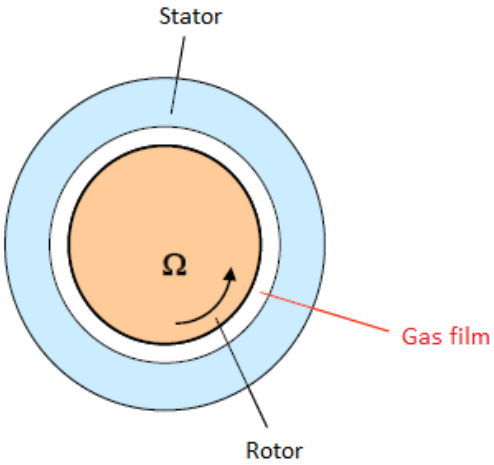


Fig. 2.3 Schematics of a gas bearing

Fig. 2.3 shows the schematics of a gas bearing. In a gas bearing, a film of gas (or lubricant), separates the rotating component (rotor) from the stationary component (stator). Hydrodynamic shear action from the moving component enables the generation of the lubricant wedge where a hydrodynamic pressure is created which produces a reaction force opposing the externally applied load. Gas bearings operating under the hydrodynamic (self-acting) principle are of simple construction, although at times they are difficult to manufacture and install because of the required minute film clearances. On the other hand, hydrostatic bearings employ external pressurization supplied through orifices or slots to enable a hydrostatic action that separates the bearing surfaces. Although Hydrostatic bearings are mechanically more complex than hydrodynamic bearings, because of their additional supply ports and mechanisms, their major advantage lies in the fact that a separation of bearing surfaces can be maintained even when the rotor is static. This advantage must be weighed against the extra cost plus the need of an external source of pressurized gas.

In 1961, Gross [33] developed and applied perturbation solutions to steady, self-acting, infinitely long journal films. These bearings mainly rely on lift generated through the film to maintain the separation of bearing structures [34]. Ausman [35] solved the linearised Reynolds equation of self-acting bearings to investigate the stability of the static equilibrium position of the shaft. A method to solve the stability problem was presented in [36], where a numerical method was developed for solving the non-linear equations to derive the orbit of the rotor centre.

Squeeze-film thrust bearings make use of a thin gas film to separate a rotor disk from a coaxial stator disk. The concept of squeeze film bearings was introduced by Salbu [37] in 1964. He also demonstrated the presence of significant axial load on the bearing, when operated in highly vibrational environment. To identify the presence of an axial force, rotor-stator clearance was described by an oscillatory motion and the squeeze-film pressure distribution was computed using the theoretical model.

For small motions of the squeeze-film journal within its clearance circle, it was shown that it is possible to linearise the equations of motion and to represent the dynamic behaviour of the squeeze-film in terms of damping and inertial coefficients. Damping coefficients were evaluated by using the Reynolds equation and a perturbation technique was used to calculate the inertial coefficients of of a bearing with a finite Length-Diameter (L/D) ratio [38].

For the demanding operating environment of a GTE, squeeze-films bearings/dampers have been used to provide lubrication, damping and reduce some unwanted air-flow in the engine [39]. It has been demonstrated that self excited instabilities may develop in squeeze-film journal bearings operating in self-acting capacity [40]. Blech [41] was able to identify

the cut-off frequencies that result in stable damped motion, when the system is subject to oscillatory disturbances.

2.3 Air-Riding Seals

Air riding seals rely on a thin film of air to separate the seal faces and they show promise of reducing wear and leakage to their practical limit. These seals can be designed to operate at the high pressures and temperatures anticipated for next-generation gas turbine engines. Similar to gas bearings, there are two classes of film riding seals being developed for gas turbines:

- Hydrostatic seals - These port high pressure fluid to the sealing face to induce opening force and to maintain controlled face separation
- Hydrodynamic seals - These typically include spiral grooves or converging seal gap, and rely on the relative surface velocity between a rotor and the stator to establish the lift force required to form and maintain an air film

2.3.1 Face Seals

As mentioned in Chapter 1, one of the earliest efforts in designing an air-riding face seal, to be used as an advanced secondary seal for managing aeroengine flows, was carried out by Dobek in 1973 [4]. He was able to demonstrate a successful operation of the seal, without rubbing contact, over a range of conditions with a maximum pressure differential of 34.4 bar, a maximum speed of 152.4 m/s and a maximum temperature of 649 °C. He was also able to show that the seal was able to operate satisfactorily under the conditions of axial seat runout (maximum axial seal seat runout of 57.15 microns) and dirt ingestion anticipated in normal engine operation.

A self-aligning spiral groove face seal was developed by Sedy in 1979 [43]. He developed a mechanical end face seal in which one of the radially extending faces was provided with spiral grooves which, through pumping action, separated the faces to form a gap for controlled leakage. In his design, a force couple was applied to the seal ring to compensate for possible clockwise or counter-clockwise twist of the ring. Fig. 2.4 shows a variation of the spiral groove face seal design which was developed by Pennink [42] in 1985. He identified the principal advantages and disadvantages associated with the spiral groove design. He stated that the leakage and power loss was very low in the spiral groove design but high machining

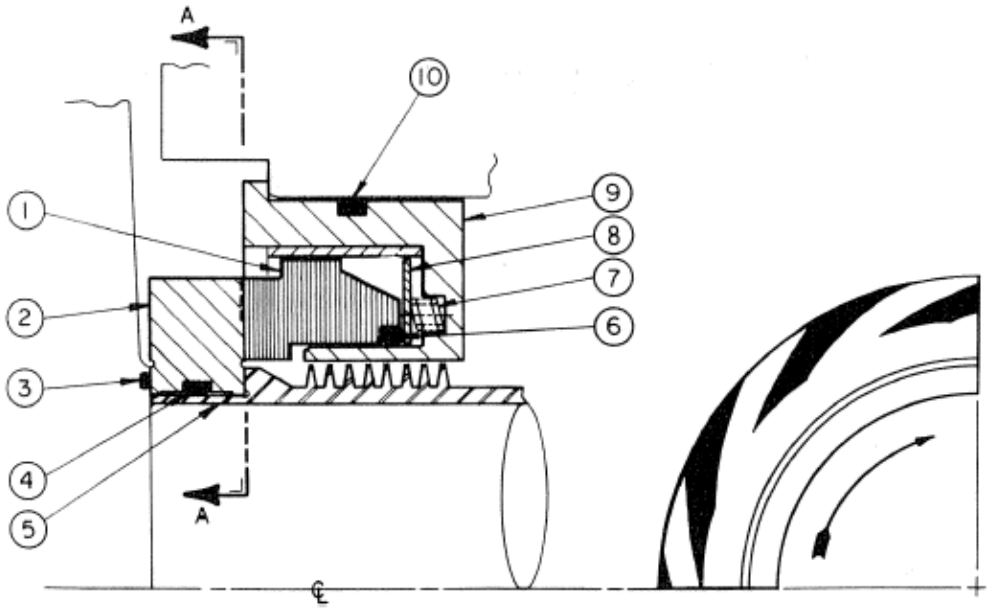


Fig. 2.4 Spiral groove seal developed by Pennink [42]. ① Primary seal ring (stationary), ② Mating ring (rotating), ③ O-ring, ④ O-ring, ⑤ Shaft sleeve, ⑥ O-ring, ⑦ Coil springs, ⑧ Dish, ⑨ Retainer assembly, ⑩ O-ring.

tolerances were needed for the mating ring seating on the shaft. In 1983, a hydrodynamic face seal was developed by Lipschitz [44], where the stator surface was provided with a plurality of spaced-apart weirs rising above the stator surface and extending between the low-pressure space and the high-pressure space.

Wentworth developed a self aligning spiral groove face seal where he used unbalanced forces for controlling the angle of convergence between the seal faces, thus regulating the thickness of lubricating film between the seal faces [45]. This was achieved by selectively arranging the support member in a predetermined lateral position on the outer cylindrical surface of one of the seal rings. The end portions of the seal ring, which were exposed to the pressurized pump, were subjected to differential pressures which caused the associated seal ring to distort. So, by selectively controlling the magnitude of seal ring distortion, he was able to regulate the face orientation of the supported seal ring relative to the other seal ring.

Lahrman presented an improved design of a face seal for applications in Gas Turbine Engines [6]. The face surface of the sealing ring was formed with a hydrostatic lift pad in the low pressure side of the seal dam. High pressure fluid was then directed to the hydrostatic lift pad to generate lift forces, which were particularly effective at slow speeds, to maintain separation of the sealing face surfaces when the lift forces achieved through the hydrodynamic pads were not sufficient to maintain a positive seal gap. Additionally, to

improve the sealing characteristics of the secondary seal, a secondary seal piston ring and a mating ring of high lubricity material, were mounted-in next to the housing. The purpose of using the mating ring was to reduce seating drag forces on the secondary seal ring as it is spring-biased into sealing engagement. Moreover, orifices were included in the design to ensure that the radial pressure forces of the working gas acting on the secondary seal piston ring are moment balanced to maintain proper sealing.

Munson and Pecht carried out experimental testing of a number of pressurised face seals subjected to high pressures and high shaft rotation speeds, similar to those found in gas turbine engine environment [8]. They suggested that engine performance can be improved by up to 6% by reducing sealing air losses, thereby reducing the overall operating cost of the aircraft by about 1%. Studies revealed that a number of seals failed unexpectedly due to contact occurring between seal faces, which indicated the need to consider some key features in the implementation of air-riding seals, including the designed seal clearance and rotor supports.

In 1990, Gardner developed an improved version of spiral groove gas lubricated seal, where he was successful in eliminating some shortcomings of a conventional spiral groove face seal [46]. In conventional designs, runout on the faces of rotating rings was found to be considerably greater than the gas film on which the seal faces used to ride. This indicated towards a need for improvement in dynamic tracking of the seal faces during rotation. He also addressed the known issue with conventional spiral groove gas seals, where they used to exhibit a substantial difference in gas film thickness between hydrostatic and hydrodynamic operation due to the significant lift force provided by the spiral grooves. As the film thickness was much larger at high rotation speed, it allowed for greater leakage across the sealing faces than would otherwise be desired. In his design, Gardner was successfully able to eliminate all these shortcomings of conventional spiral groove gas seals.

Pope underlined the importance of the concentricity of the ring member with respect to other seal components for proper seal operation [30]. He stated that concentricity helped to maintain concentric, balanced pressure forces on the seal components, which in turn resulted in good sealing characteristics while permitting the use of smaller, more lightweight seal components. In conventional seals, the ring member was pressurized radially inwardly by the higher pressure region, which led the ring to deform to an out-of-round shape. This could be avoided if the ring was made sufficiently massive and stiff, but the ring member should ideally have a low mass inertia and relatively high compliance for reduced seal weight and, more importantly, reduced hysteresis in the clearance between the radial sealing surface and

the restricting tooth. In his design, Pope was able to rectify this problem by providing a radially outwardly pressurized face seal ring member to maintain ring shape.

Another significant advantage posed by Pope's design [30] was a reduced mass inertia face seal member for reduced sealing clearance hysteresis. He was also able to control the clearance between a stationary seal housing and a translating face seal ring member to maintain pressure balance on seal components, notwithstanding differential growth of an engine stationary engine structure and seal housing relative to other seal components.

in 2000, Wang presented an improved design of spiral grooved face seal [47]. He was able to design a combined hydrodynamic and hydrostatic face seal with double spiral grooves, which formed a fluid film with greater thickness than the prior art under the same condition, or with greater stiffness under the same thickness of the fluid film. In his design, two spiral groove sets were provided at least on one of the faces of the rotating and the stationary rings, wherein one set disposed on the high pressure side, i.e. at the upstream, and the other set disposed on the low pressure side, i.e. at the downstream.

In comparison with a pure hydrodynamic face seal with double spiral grooves, in Wang's design [47], the radial length of an upstream spiral groove was always greater than that of the downstream one. Therefore, under the given rotational direction, the overall effect of these two spiral groove sets was to pump the sealing fluid from the high pressure side towards the low pressure side. Such kind of pumping had a tendency of producing a slight leakage. However, at the cost of the slight leakage, a significant improvement in fluid film thickness and stiffness could be achieved. Therefore, Wang's seal design was found to be more suitable for sealing fluids with low viscosity, such as gas, than the prior pure hydrodynamic face seal with double spiral grooves.

In 2005, Garrison and McNickle [48] presented an improved version of hydrostatic face seal for GTE, demonstrated a Technology Readiness Level (TRL) of level 6. Fig. 2.5 shows the schematics of the air-riding seal developed by Garrison and McNickle. Successful operation of this non-contacting hydrostatic seal was demonstrated for a maximum rotational speed of about 305 m/s., temperature of about 538 °C. and differential pressure of about 4.1 bar. The seal operated on a gas film clearance of the order of 38-64 microns. The face seal was normally retracted away from the rotor face during start-up and shut-down conditions when insufficient differential pressure existed. This eliminated any rubbing between the sealing surfaces. As pressure started building up in the engine, the seal started to close toward the rotor due to a thrust balance that developed across the area defined by the seal aspirator tooth and seal balance diameter. The seal continued to move towards the rotor until an operating gas film was established by the high pressure air flowing over the stepped seal

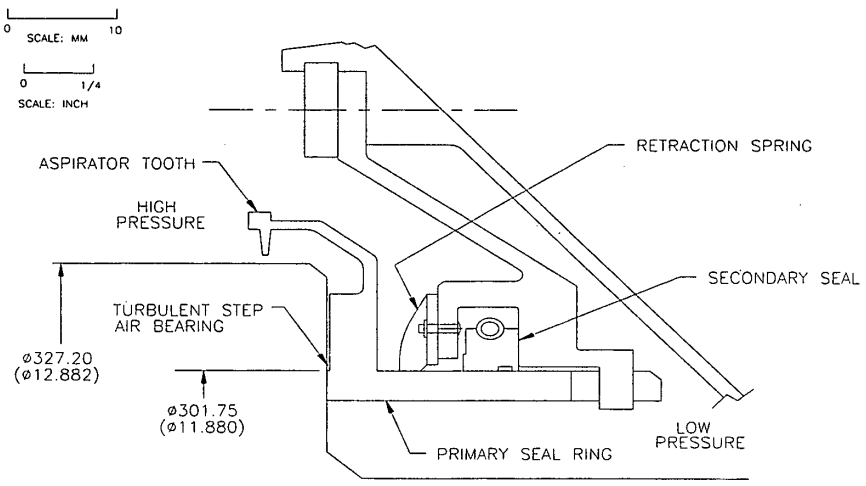


Fig. 2.5 Schematics of the seal developed by Garrison and McNickle [48]

face. The seal reached equilibrium when the force balance was satisfied, establishing an equilibrium film thickness.

In yet another design improvement, Garrison and McNickle [49] designed an air-riding seal system which included a primary seal assembly, a secondary seal assembly, and a structure that increased the stiffness of a thin film between the seal system and a moving part. The outermost circumferential surface along the seal runner included a notch that varied the gap depending on the relative position between the primary seal assembly and seal runner. The primary seal ring was composed of a ceramic, like silicon nitride and it included a plurality of arcuate seal segments which could be adjusted separately.

In this design, Garrison and McNickle [49] were able to demonstrate a positive sealing which was durable, predictable, and uniform over the lifespan of the seal. The seal leakage was minimised and it facilitated better fuel efficiency within gas turbine engines. This design improved the ability to track the runout of a rotor and to restore the thin film seal to equilibrium. The invention was demonstrated to be applicable to engines operating at temperatures of up to 815 °C and rotational speeds of about 450 m/s.

A problem associated with air-riding carbon seals arises from the difficulty of forming the rotor seal face so as to be perfectly flat. Any surface imperfections on the rotor seal face effectively form high points, and these impart an oscillating motion to the carbon sealing ring as the rotor rotates at high speed. The carbon sealing ring can thus be caused to lift and drop once per revolution of the rotor.

Jahn designed an air-riding seal which eliminated this issue [50]. In his design, the primary support arrangement accommodated relatively low frequency axial movements between said the primary and secondary seal members and secondary support arrangement accommodated relatively high frequency axial movements between the seal members. The arrangement was configured in such a way so that the air-riding film generated between the seal surfaces was sufficient to overcome the biasing force and any pressure forces acting on the seal members.

2.3.2 Circumferential seals

Circumferential seals or segmented-ring seals have been discussed briefly in Chapter 1. In Gas Turbine Engines, circumferential seals are used to separate ambient areas of high pressure air from an oil wetted area at lower pressures and serve two major functions. First, circumferential seals prevent the leakage of oil from the lower pressure bearing compartment. Second, circumferential seals minimize the flow rate of the hot air from the high pressure area to the oil wetted sump.

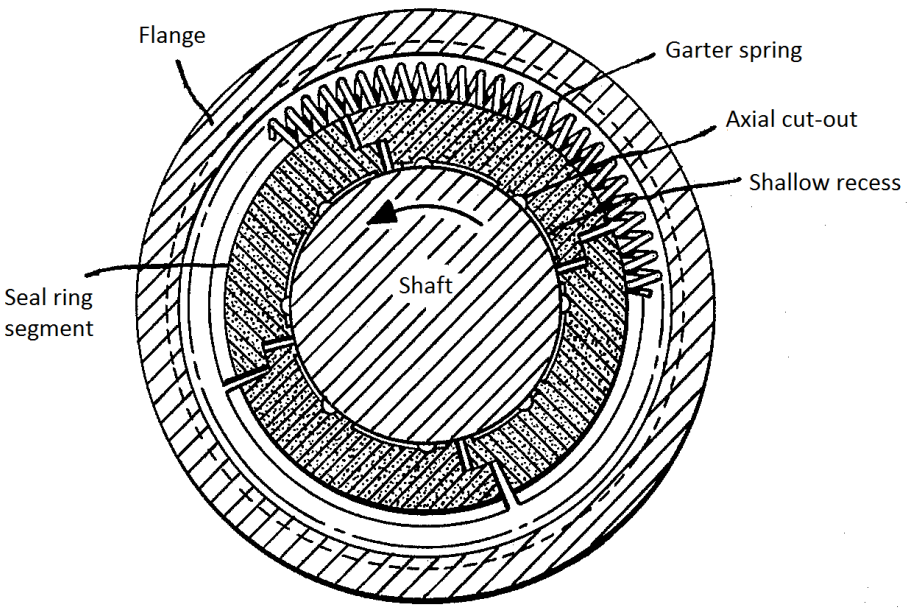


Fig. 2.6 Segmented seal ring in Stein's design [11]

In 1978, Stein invented the segmented ring-type seal design for sealing between a rotating member and a housing [11]. Fig. 2.6 shows the segmented seal ring in Stein's seal design.

The sealing members were provided in the form of a segmented seal ring mounted on a shaft. The seal ring was segmented by providing a plurality of end-to-end circumferential segments to form the seal ring, such that a seal is also effected in the radial direction between each segment. In the circumferential sealing face of each segment of the seal ring adjacent to the shaft, precise grooves were provided which produced a negative hydrodynamic lift force and forced the seal ring segments towards the rotating shaft in order to reduce the leakage. Thus, during shaft rotation, the fluid medium in which the seal was operating was swept out of the sealing grooves (marked as shallow recess in Fig. 2.6) through an axially disposed communication port (axial cut-out) by a pumping action to provide the negative hydrodynamic lift force and to move the seal ring toward the shaft to effectuate greater sealing.

For certain applications, especially when the seal was operating in a pressurised oil mist atmosphere, Stein's design [11] used to show leakage along the radial path between adjacent segments. This resulted from a pressure build up in the space between the tongue of one segment and the complementary groove in the adjacent segment. Borkiewicz was able to improve Stein's design by solving the problem of this leakage in the seal [12]. In his design, he provided a pressure relieving passageway in each segment, extending from a location in the radial space between segments to one of the recesses, thus providing a flow path for fluid in each radial space to pass into a recess, thereby preventing leakage of fluid through the radial space.

In 1994, Hwang and Pope provided a solution to the inefficient and insufficient oil cooling which was inherent in conventional circumferential seals having under-cooled runners [51]. They were also able to reduce the amount of heat generated at the rubbing interface of a circumferential seal. In their design, cooling oil was injected directly onto the outer circumferential surface of the runner and in the direction of the bearings. The runner shielded the seal interface from the cooling oil. A disk pump was mounted on the main shaft between the runner and the bearing to facilitate the scavenging of oil from the cavity between the bearings and seal assembly, thereby reducing the amount of oil reaching the seal interface.

In 1998, Hwang presented another variation of the circumferential seal design where he tried to address the issue of the complexity posed in manufacturing these seals [13]. In his design, a plurality of constant-depth elongated lift pockets or lift grooves are provided, extending parallel to each other from the inlet across a substantial portion of the bore region of each of the seal segments and terminating short of the trailing edge of the seal segment. Thus by providing a plurality of constant-depth, elongated, parallel lift pockets extending from a common inlet, a single machining depth for the pockets is established, which can

be performed in a single machining operation wherein the pockets may be cut concurrently. Moreover, the depth of the lift pockets was such that in the event of wear of the bore surface, resulting in a reduction of pocket depth, the force generated in the now shallower pocket was increased to increase the seal gap. Thus wear of the bore surface served to increase the pressure in the pockets to increase the seal gap, making the seal gap essentially self-regulating in size.

Vasagar *et al.* [52] designed a circumferential seal which comprised of a plurality of adjoining annularly sealing ring segments facing the rotating shaft, wherein each sealing ring segment included a dead end circumferential groove adjoined with a bore dam and at least one additional groove machined within a shaft-side face of each sealing ring segment. The additional groove(s) was designed to direct fluid flow into the dead end circumferential groove such that fluid directed into the dead end annular groove increased the fluid pressure within the dead end circumferential groove, thereby, forming a seal between the seal segments and the shaft.

In one design variation presented by Vasagar *et al.* [52], the additional grooves were composed of one or more hydrodynamic inclined pumping grooves. In operation, when the shaft rotated, the inclined grooves directed the fluid, generated by the rotation of the shaft, along the inclined grooves and into the dead end groove. As the air began to accumulate within the dead end circumferential groove, it increased the air pressure inside the groove, which was redirected towards the shaft creating a lift force on the seal segments. The lift force expanded the seal segments away from the shaft, creating a minute clearance between the shaft-face of the seal segments and the rotating shaft. This configuration had the advantages of creating an air seal that did not interfere with the rotation of the shaft, while reducing the wear on the shaft-side face seal as a result of the rotation of the shaft.

Most of the circumferential seal designs comprise of a seal runner that is associated with a rotating structure, which is formed from a different material. As a result, the seal runner and the rotating structure may have different coefficients of thermal expansion. If the rotating structure were to expand rapidly, it could result in relatively rapid expansion of the seal runner and the generation of hoop stresses in the seal runner [53]. If the seal runner is formed from a relatively hard material, it would therefore be desirable to support the seal runner radially, in such a manner so that it maintains its position relative to the rotating structure, but also accommodates relative size changes of the underlying rotating structure.

Munson addresses this problem in his circumferential seal design [53]. In his proposed design, the seal elements could be formed from carbon or any other material, but each of the seal elements and the corresponding static structure had a cumulative second coefficient of

thermal expansion, that could be different from the first coefficient of thermal of expansion. This arrangement allowed the sealing elements to expand or contract in response to differential thermal growth of the seal runner relative to the sealing elements and also compensated for wear.

In the literature, the experimental and theoretical studies carried out on air-riding seals provide an understanding of the structure of these seals and the dynamic behaviour of the fluid film during seal operation. Since the invention of these seals in early 1970s, the literature provides evidence of continuous growth of this technology through various design modifications, which has led to significant improvement in performance of these seals. Air-riding sealing technology is now widely considered as the technology which might be used as the non-contacting sealing solutions for future aircraft engines.

2.4 Modelling Air-Riding Fluid Films

The methodology of modelling air-riding films and the results from modelling analyses are presented in the literature by a number of authors. Analyses on Reynolds equation based models for analysing the properties and characteristics of compressible fluid films has been well detailed in the literature. The phenomenon of generation of a lift force on compressing the fluid film has led to the development of technologies (like gas bearings) which exploit this property of fluid films.

Following the work of Tower, Reynolds [54] used a reduced form of the Navier-Stokes equations to generate a second-order differential equation for evaluating the pressure in a narrow, converging gap between bearing surfaces. Models based on Reynolds equation have since been used to model incompressible and compressible flows for a variety of applications.

In 1956, Popper and Reiner [55] showed that when air is caused to flow between two parallel plates separated by a small distance and in relative rotational motion with respect to each other, a vertical force is generated. They also noticed a centripetal pressure difference in the fluid film. To explain these phenomena, they laid down the hypothesis that air could display non-Newtonian fluid properties. This later led to the use of lubrication equations for modelling compressible flows.

Elrod [56] derived the equation governing the steady-state pressure in a journal bearing lubricated by an incompressible fluid with constant viscosity. Laglois [57] adopted a similar approach Elrod's in order to derive the equation governing the pressure in a thin film of compressible fluid, when both lateral and relative normal motions of the surfaces are present.

He also showed that when the frequency of the squeeze motion is sufficiently high, the escape of the gas is effectively blocked by its own viscosity, or in other words, the bearing tends to behave like a bellows. For low squeeze motion frequency, the gas leaks out before it is significantly compressed. He carried out the squeeze film analysis for variety of different configurations like short and infinite rectangular films, axisymmetric disks etc.

Studies carried out by Salbu [37] and Minikes *et al.* [58] showed that full non-linear model of the Reynolds equation is required to account for the largest pressures in the fluid film. This argument was supported through the studies carried out by Fourka *et al.* [59] who concluded that non-linear compressibility effects had to be included in the Reynolds equation model to validate his finite element model against experimental results.

Stolarski and Chai [60] computed the squeeze film pressure profiles for an imposed normal motion of finite amplitude, by using Reynolds equation for compressible flow. They also investigated the effects of varying the amplitude and frequency of oscillation. Minikes *et al.* [58] carried out similar studies based on varying amplitude and frequency of normal oscillation. They observed that the analytical results for small amplitude oscillations did not result in positive squeeze film force, and they concluded that only large amplitude oscillations result in positive squeeze film force. Blech [41] demonstrated that the stiffness and damping properties of the fluid film is related to the forcing frequency. Forcing frequency was incorporated in the Reynolds equation through squeeze film number.

As most of the squeeze film analyses have been based on Reynolds equation, the effect of fluid inertial on the fluid film properties have been largely neglected, even though theoretical analyses which account for fluid inertia at moderate Reynolds numbers have predicted large discrepancies from classical lubrication theory. Different measurement techniques of fluid inertial forces in squeeze film configurations have been adopted by different authors, but these investigations have mainly been concerned with small amplitude motions.

Fritz [61] performed analyses and tests to investigate the added mass and damping forces of a fluid in a thin annulus surrounding a rotor vibrating due to unbalanced forces. Experimental results indicated that the added mass values were 25% lower than predicted, which was attributed to the axial leakage through the end seals of the test rig. Yang [62] carried out similar studies for vibrating rods in confined viscous fluids. He observed that there was excellent correlation between the theoretical and experimental results, although the clearance ratios tested were higher than those usually found in lubrication applications.

Constantinescu and Galetuse assumed in their studies [63] that the velocity profiles remain unaffected by the fluid inertia, with only the velocity magnitude varying. Several authors have adopted this approach for modelling hydrostatic seals. Based on [63], Brunetière

and Tournerie presented a theoretical model for axisymmetric laminar or turbulent radial flows, including fluid inertia [64]. They simplified and combined the Navier-Stokes and continuity equations to obtain a modified Reynolds equation. The model was then validated by comparing it to the analytical and experimental results, and then the model is applied to a hydrostatic seal.

On reviewing the literature about the effect of incorporating inertia it was observed that the overall effect of inertia is governed by both the geometry of the structure housing the air-riding film and the extent to which inertial components contribute towards the flow.

Gas film lubrication theory can be categorised into two different groups: thin film lubrication and ultra-thin film lubrication. The Knudsen number, K_n, defined as the ratio of the molecular free path to the film thickness, determines which model should be applied for analysing the characteristics of the fluid film. If $K_n < 10^{-3}$, the fluid can be considered as a continuum, and the classical Reynolds equation compressible fluids would be applicable for modelling the gas flow. For $10^{-3} \leq K_n \leq 10$, the fluid is considered as a rarefied gas, so a modified form of Reynolds equation should be used. For $K_n > 10$, the fluid is considered as a free molecular flow [65].

Another important parameter to be considered in gas film modelling is the compressibility number or bearing number, Λ, which describes the level of fluid compressibility as function of the sliding speed for hydrodynamic gas bearings. Closed form solutions for bearing number Λ are not readily available. Hence, predictions of bearing film pressure and its force reaction supporting an applied load must rely on numerical analysis. For low bearing numbers ($\Lambda < 100$), finite differences or finite element methods applicable to elliptical differential equations are quite adequate. However, it is well known that these numerical methods are inaccurate and numerically unstable for large speed numbers, since the advection fluid transport term starts to dominate the flow field, and the Reynolds equation takes a parabolic form [66].

In recent times, researchers have started using commercial computational fluid dynamics (CFD) programs for modelling fluid films. The main advantage of a CFD code is that it uses the full Navier–Stokes equations and provides a solution to the flow problem, whereas finite difference codes are based on the Reynolds equation. The results obtained by the two approaches are therefore likely to differ. Moreover, the CFD packages can be used to model the flow and fluid film in very complex geometries.

In 1998, Chen and Hahn [67] investigated the capability of CFD software to model thin fluid films in bearings. They concluded that CFD software was capable of accurately handling the steady state hydrodynamic lubrication problems pertaining to journal bearings, slider

bearings, and squeeze-film dampers. Guo *et al.* [39] used the CFD package called CFX-TASCflow to simulate the pressure field and calculate the static and dynamic characteristics of hydrodynamic, hydrostatic & hybrid bearings, and squeeze film dampers.

Gertzos *et al.* [68] examined the performance characteristics and the core formation in a hydrodynamic journal bearing lubricated with a Bingham fluid. The Navier–Stokes equations were solved using the FLUENT package. The results of the developed 3-D CFD model were compared with theoretical and experimental results of previous investigations, for both Newtonian and Bingham lubricants, and found to be in very good agreement.

Shenoy *et al.* [69] carried out an overall Elasto-hydrodynamic lubrication analysis of full journal bearing using the sequential application of CFD and Computational Structural Dynamics (CSD), in effect carrying out a coupled Fluid-Structure Interaction analysis (FSI). The simulation results of EHL were found to have a good agreement with that of the standard lubrication solutions. Using FSI, they were successful in finding the bearing surface deformation under static load and they argued that their approach could also be extended to predict the bearing performance under dynamic loading condition.

Although application of CFD software in solving thin film lubrication problems has been a recent development, there is sufficient proof in the literature to suggest that they are able to accurately predict the hydrodynamic and hydrostatic bearing performance for static and dynamic loading condition.

2.5 Summary

This chapter provides of a detailed literature review of different sealing arrangements. Prior-art and state-of-the-art in labyrinth seal and brush seals, the most commonly used seals in gas turbine engines were studied and their limitations were highlighted. On reviewing the open literature it was observed that several authors were of the opinion that air-riding technology could address the shortcomings of labyrinth and brush seals, and they show promise of meeting the requirements of future aircraft engines.

One of the earliest application of air-riding technology was seen in gas bearings. As more maturity was gained in the gas bearing design, the air-riding technology was investigated for sealing application. The first kind of air-riding seal was developed as a face seal. With advancement in face sealing technology more and more features, like double spiral groove, were incorporated by various inventors to make it more efficient and viable for wider range of operating conditions. In spite of the growth and advancement seen in this technology, the

challenges involved in axial-gap seal design have been highlighted in this chapter and the previous chapter.

Circumferential seals were radial-gap seal designs which were developed in late 1970s. Although they benefited from advantages of a radial-gap sealing design, their segmented design posed some issues and their operability was limited. This further highlighted the possible advantages of a full-ring seal design.

Various modelling techniques used model the air-riding film in the prior-art and present-art were investigated. It was realised that a number of authors used Reynold's equation for modelling the fluid film. It was observed that authors are now beginning to use commercial CFD codes for modelling the air-riding film.

Chapter 3

1-D and 2-D Analysis of the Thin Fluid Film

3.1 Seal Geometry and Seal Assembly Schematics

On reviewing the literature on air-riding seals, it was concluded that no prior art exists for a full-ring radial-gap air-riding seal. So, the first step was to envisage a possible seal geometry and a schematics of the seal assembly, utilising some of the fluid film generation properties being utilised in other air-riding technologies. The preliminary design criteria that should be considered for designing the radial gap seal are:

1. Sufficient lift force or pumping force should be generated from the fluid film to keep the seal ring afloat.

2. As the seal ring will float on the fluid film, the ring needs to be supported through a supporting arrangement.

3. The supporting arrangement should be able to withstand the force exerted by the high pressure fluid (so in effect, act like a secondary seal), but it should be less stiff than the fluid film, so that the fluid film is able to "drive" the seal ring.

As discussed in Section 2.3 and Section 2.4, lift force from a fluid film can be generated through two possible means - hydrodynamic and hydrostatic. As there would already be a high differential pressure across the two axial ends of the seal, the fluid film will be able to generate some hydrostatic lift.

For hydrodynamic lift generation, the two necessary conditions are: relative motion between the rotor and stator, and a converging gap geometry. The first condition is satisfied by virtue of a static seal ring(stator) and a rotating shaft(rotor). The second condition can be met by designing a seal ring with axially converging (from inlet to outlet) seal gap.

The design details of the supporting arrangement will be discussed in the subsequent chapters, the limiting stiffness criterion for the supporting arrangement can be estimated once the stiffness values of the fluid film are calculated.

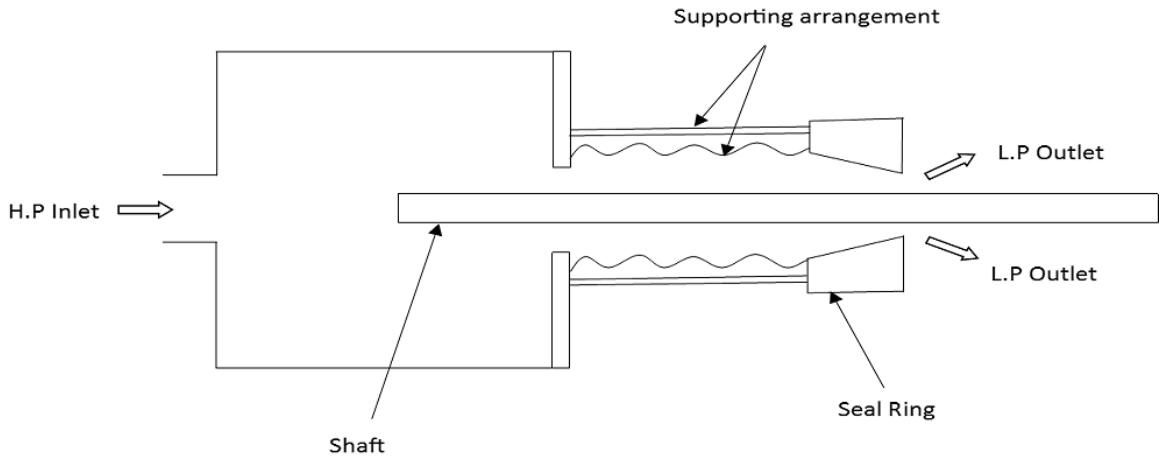


Fig. 3.1 Seal assembly schematic

Fig. 3.1 shows the designed schematic of the seal assembly. High Pressure air enters through the H.P inlet, passes through the secondary seal (supporting arrangement) and gets directed towards the seal ring inlet. After passing through the converging air gap of the seal ring, air exits the assembly through the L.P Outlet. A supporting arrangement, with one end fixed to the casing and the other end to inlet end of the seal ring, acts as a support for the seal ring.

Once a possible schematic of the seal assembly was developed, the next step was to model the fluid film of the seal ring. 1-D and 2-D analyses were carried out to determine the thin film characteristics.

3.2 1-D Analysis

As a part of the preliminary analysis to see the viability of the concept discussed above, an initial 1-D analysis of the fluid flow through the seal was carried out for a simplified seal geometry.

The short-cylindrical film geometry was spread-out like a wedge shaped film, and the converging gap was imagined to be composed of n equal steps, as shown in Fig. 3.2. In Fig. 3.2, L is the length in the axial direction, W is width of the wedge shaped film (i.e. circumference of the seal ring), P_{in} is the inlet pressure and P_{out} is the pressure at the seal outlet. h_1 denotes the seal height of the first step and h_n denoted the height of the seal gap for the n^{th} step.

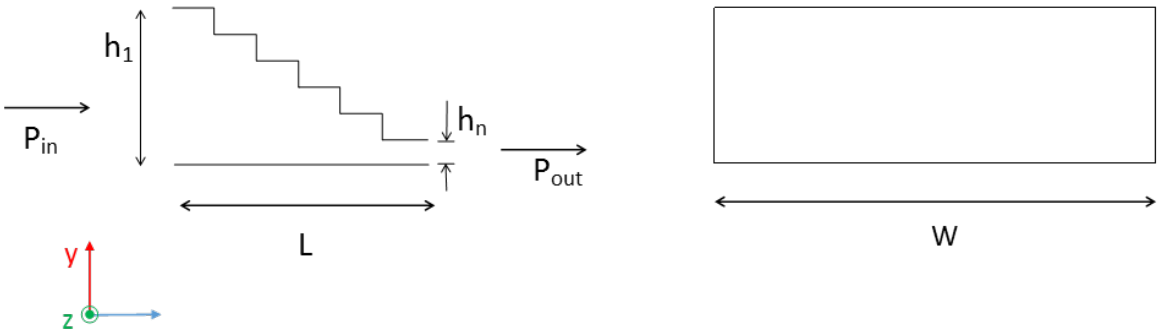


Fig. 3.2 Seal gap geometry

To analyse the flow through the seal, flow through each seal step was considered as flow between two parallel plates. Since the average seal height chosen for the seal was about 32 µm(will be discussed later in this section), which is further divided in a number of steps, the flow can safely assumed to be laminar and incompressible in each of these steps. Some of the key assumptions made for the preliminary analysis were:

1. Flow is considered to be steady, laminar and incompressible.
2. The flow is fully developed
3. No slip condition

The mass conservation equation can be written as:

$$\frac{\partial \rho}{\partial t} + \frac{\partial (\rho u)}{\partial x} + \frac{\partial (\rho v)}{\partial y} + \frac{\partial (\rho w)}{\partial z} = 0 \tag{3.1}$$

On applying the first assumption (listed above) to Eq. 3.1, and considering the flow in only 'x' direction, Eq. 3.1 reduces to:

$$\frac{\partial u}{\partial x} = 0 \tag{3.2}$$

Navier-Stokes momentum equations are written as:

$$\rho\left(\frac{\partial u}{\partial t} + u\frac{\partial u}{\partial x} + v\frac{\partial u}{\partial y} + z\frac{\partial u}{\partial z}\right) = \rho g_x - \frac{\partial p}{\partial x} + \mu\left(\frac{\partial^2 u}{\partial x^2} + \frac{\partial^2 u}{\partial y^2} + \frac{\partial^2 u}{\partial z^2}\right) \tag{3.3}$$

$$\rho\left(\frac{\partial v}{\partial t} + u\frac{\partial v}{\partial x} + v\frac{\partial v}{\partial y} + z\frac{\partial v}{\partial z}\right) = \rho g_y - \frac{\partial p}{\partial y} + \mu\left(\frac{\partial^2 v}{\partial x^2} + \frac{\partial^2 v}{\partial y^2} + \frac{\partial^2 v}{\partial z^2}\right) \tag{3.4}$$

$$\rho\left(\frac{\partial w}{\partial t} + u\frac{\partial w}{\partial x} + v\frac{\partial w}{\partial y} + z\frac{\partial w}{\partial z}\right) = \rho g_z - \frac{\partial p}{\partial z} + \mu\left(\frac{\partial^2 w}{\partial x^2} + \frac{\partial^2 w}{\partial y^2} + \frac{\partial^2 w}{\partial z^2}\right) \tag{3.5}$$

On applying the assumptions stated before, the equations are reduced to:

$$\frac{\partial p}{\partial x} = \mu\frac{\partial^2 u}{\partial y^2} \tag{3.6}$$

$$\frac{\partial p}{\partial y} = -\rho g_y \tag{3.7}$$

$$\frac{\partial p}{\partial z} = 0 \tag{3.8}$$

On integrating Eq. 3.7:

$$p = -\rho g_y y + g_1(x) \tag{3.9}$$

On integrating Eq. 3.6 twice with respect to y :

$$u = \frac{1}{2\mu}\frac{\partial p}{\partial x}y^2 + C_1(y) + C_2 \tag{3.10}$$

After applying the no-slip condition to calculate the values of C_1 and C_2, and on putting their values in Eq. 3.10, the velocity profile u is obtained as:

$$u = \frac{1}{2\mu}\frac{\partial p}{\partial x}\left(y^2 - \left(\frac{h}{2}\right)^2\right) \tag{3.11}$$

Volumetric flow per unit depth can be calculated as:

$$\frac{Q}{w} = \int_{\frac{-h}{2}}^{\frac{h}{2}} u \, dy = -\frac{h^3}{12\mu} \frac{\partial p}{\partial x} \tag{3.12}$$

$$Q = \frac{w h_i^3 (P_2 - P_1)}{12 \mu L_{eq}} \tag{3.13}$$

where, P_1 and P_2 are the pressures at seal step inlet and seal step outlet respectively,h_i is the height of i^{th} step and L_{eq} is the length of each seal step.

So, from Eq. 3.13, the pressure at the step outlet can be calculated by:

$$\boxed{P_2 = P_1 - \frac{12 \mu Q L}{w h_i^3}} \tag{3.14}$$

3.2.1 1-D Numerical Modelling

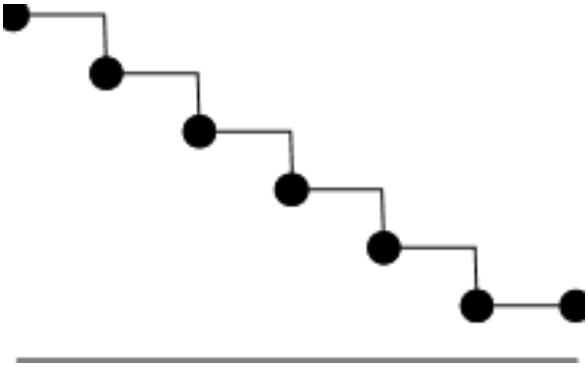


Fig. 3.3 Seal steps with seal nodes

A Matlab code is written to calculate the pressure values at all seal steps. For ease of calculation and understanding, the ends of the seal steps are considered as nodes, as shown in Fig. 3.3. So, for n seal steps, there will be $n+1$ seal nodes. Eq. 3.14 can be expressed in the following form:

$$P_{i+1} = P_i - \frac{12 \mu \dot{m} L}{\rho_i w h_i^3} \tag{3.15}$$

Table 3.1 Input parameters for the 1-D numerical model

Parameter	Symbol	Value
Axial length	L	20 mm
Shaft diameter	D	40 mm
Inlet Pressure	P_{in}	4 bar
Outlet Pressure	P_{out}	1 bar
Seal inlet height	h_{in}	50 µm
Seal outlet height	h_{out}	14 µm
Number of axial nodes	n	101
Density of air (at 25 °C)	ρ	1.184 kg/m^3
Dynamic viscosity of air (at 25 °C)	μ	1.86×10^{-5} Pa-s

where, $\dot{m}$ is the mass flow rate through the seal and ρ_i is the average density of the fluid at the i^{th} step. Eq. 3.15 will be used as the governing equation for calculating the pressure at each seal step.

Table 3.1 includes all the input parameters and boundary conditions needed to carry out the 1-D simulations on Matlab. The methodology followed for the 1D analysis has been described below:

- **Step 1:**
  The inlet pressure is kept constant at 4 bar and the pressure at each seal node is calculated for a range of mass flow rate values (from 10^{-5} kg/s to 10^{-1} kg/s) using Eq. 3.15, till the calculated pressure ratio is more than 4.

- **Step 2:**
  For the fluid flow analysis through the seal, the inlet and outlet pressures are known but the mass flow rate is unknown. So, a curve fitting approach is adopted to evaluate the mass flow rate the seal that is needed to achieve a pressure difference of 3 bar across the seal. Fig. 3.4 shows the curve fitted to the pressure difference values obtained for a range of mass flow rate values.

- **Step 3:**
  The pressure values at the seal nodes are then calculated again, based on the inlet pressure and the mass flow rate determined from the previous step.

From the curve fitting exercise (as shown in Fig. 3.4), it was calculated that for a pressure difference of 3 bar, the mass flow rate of air flowing through the seal is 1.2×10^{-4} kg/s. Fig. 3.5 shows the pressure drop across the seal length from inlet to outlet.

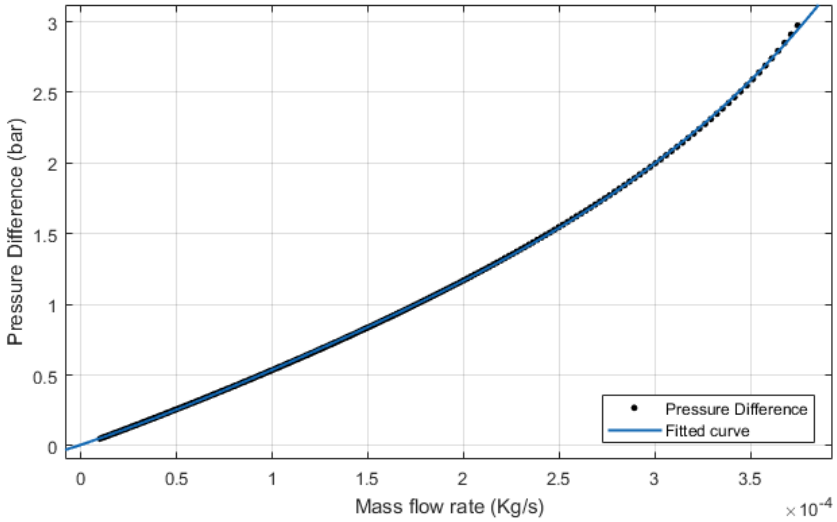


Fig. 3.4 Fitted curve on the pressure-difference data

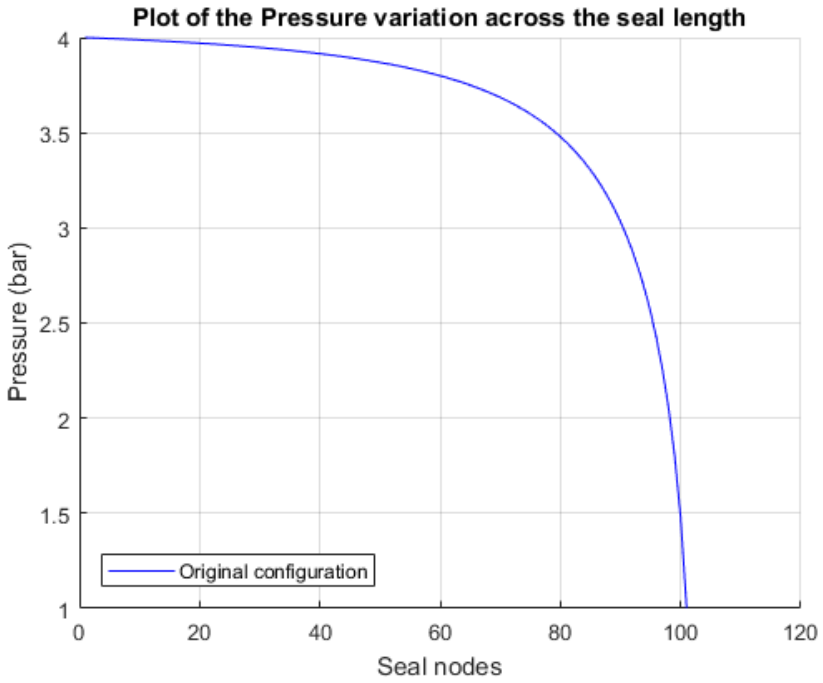


Fig. 3.5 Pressure variation across the seal

Film Stiffness Analysis

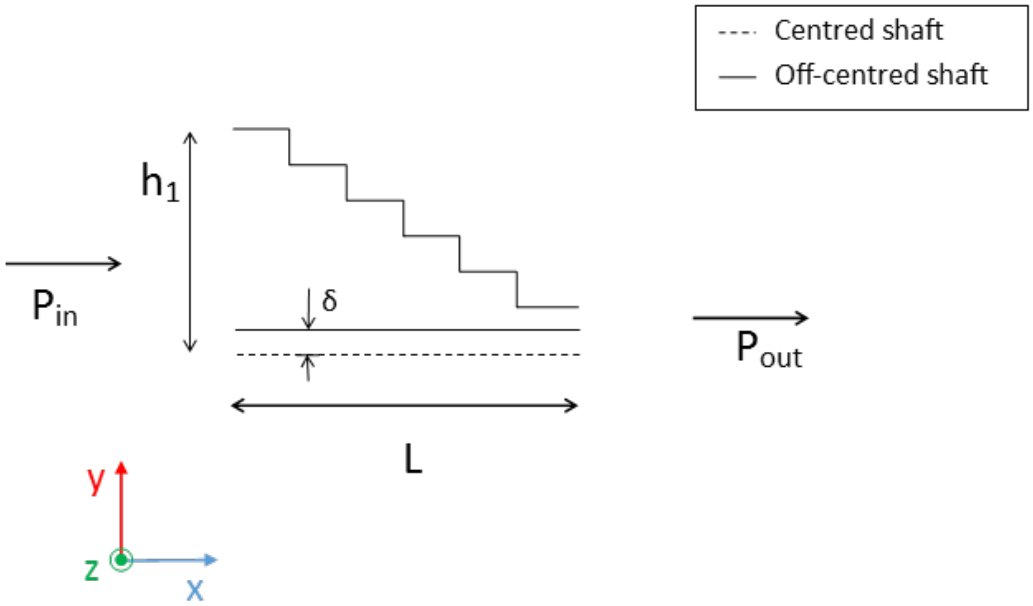


Fig. 3.6 Shaft off-centred by an amount δ

To calculate the air film stiffness, the shaft is imagined to be off-centred in Y by an amount $\pm\delta$. Fig. 3.6 shows a schematic of the axial cross-section of the seal, when the shaft is off-centred in Y by an amount δ. The methodology to calculate air film stiffness is described below:

- **Step 1 to Step 3:**
  To calculate the pressure profile through the off-centred seal geometry, the same 3-step procedure is followed as described in Section 3.2.1

- **Step 4:**
  The differential pressure calculated for each step of the off-centred is then multiplied by the corresponding area of the step to obtain the net force in Y acting on the corresponding step.

- **Step 5:**
  The net force in Y acting on all steps are added to calculate the net lift force acting on seal due to the off-centred shaft.

- **Step 6:**
  The stiffness of the air film is then calculated using Eq. 3.16.

Fig. 3.7 shows the comparison of the pressure profile of the seal for the centred and the off-centred shaft (when $\delta = 2$ µm), and shows the variation of lift force generated across the seal for the off-centred shaft.

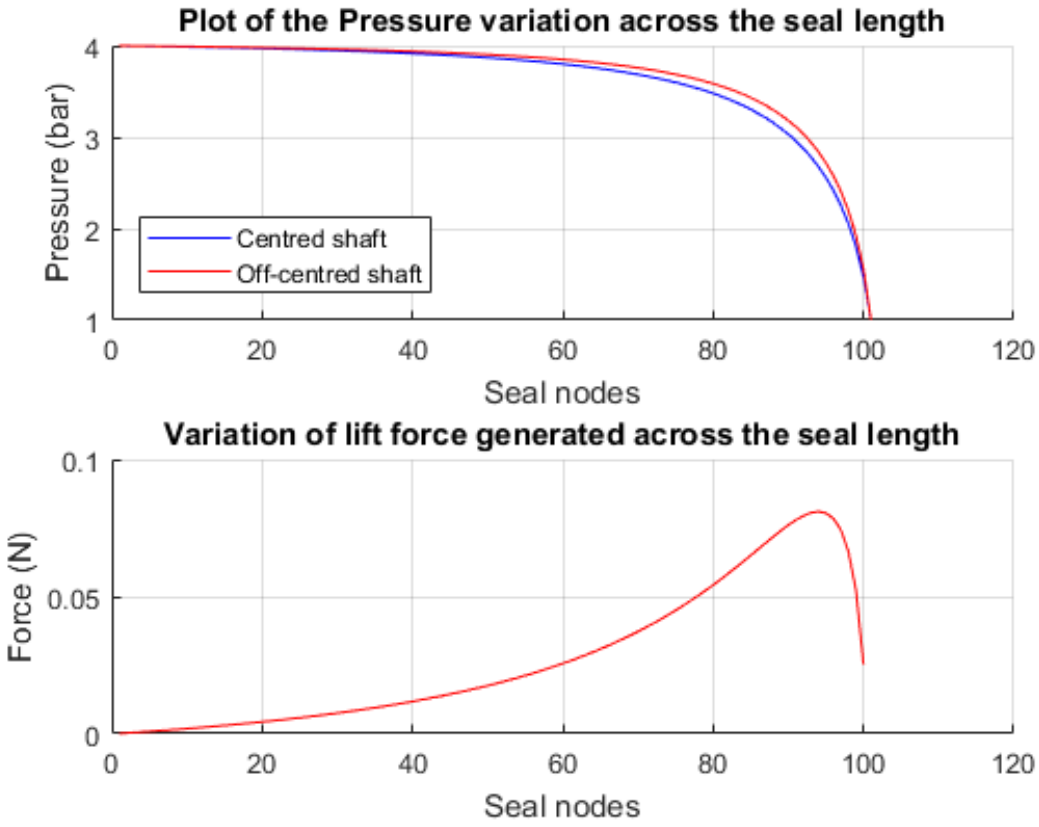


Fig. 3.7 Pressure profiles for the centred and off-centred shaft, and variation of lift force generated across the seal length when the shaft is off-centred by 2µm

Stiffness of the air-film is obtained from the equation:

$$K = \frac{\Delta F}{\Delta \delta} \tag{3.16}$$

$$K = 1.75 \times 10^6 \text{ N/m} \tag{3.17}$$

where, ΔF is the net lift force generated by the film.

The results from 1-D simulations of the fluid film properties of the seal can be summarised as shown in Table 3.2. Simulation results from the 1-D analysis clearly indicated that some significant hydrostatic film stiffness can be achieved from the selected geometry and input

Table 3.2 1-D simulation results

Property	Value
Leakage rate	1.2×10^{-4} kg/s
Film Stiffness	1.75×10^{6} N/m

parameters. This indicated towards a need for 2-D analysis of the fluid film to get more accurate values of hydrostatic and hydrodynamic stiffness.

3.3 2-D Analysis

As stated in Section 2.4, Reynolds equation based models have been widely used for determining the characteristics and properties of compressible fluid films, though it should be noted that inherent assumption of a no-slip condition in the derivation of the Reynolds equations restricts its applicability for all fluid films.

A preliminary investigation was carried out to explore the validity of the Reynolds modelling for analysing the flows through the radial gap of the air-riding seal. As discussed in Section 2.4, the validity of the Reynolds equation for a thin film can be determined by calculating the Knudsen number. The Knudsen number, K_n is defined as:

$$K_n = \frac{\lambda}{L} \tag{3.18}$$

where, λ is the mean free path of the fluid and L is the characteristic geometric scale of the flow domain, which in this case will be the seal gap height. From the kinetic theory of gases, λ can be determined from the equation:

$$\lambda = \frac{k_B T}{\sqrt{2}\pi d^2 p} \tag{3.19}$$

where, k_B is the Boltzmann constant, T is the temperature, d is the diameter of the fluid molecule, and p is the pressure.

The Navier-Stokes equations, which are valid for continuum flows, are applicable to flows where K_n values are less than 0.001. Higher values of K_n indicate that the continuum assumption of the Navier-Stokes equations is no longer valid. Studies carried out by Sayma *et al.* [70], for a given geometry and a pressure ratio of 2.33, indicated that a continuum flow

Table 3.3 Knudsen number as a function of the seal gap

Seal gap (microns)	Knudsen Number
14	4.13×10^{-4}
20	2.89×10^{-4}
30	1.93×10^{-4}
40	1.45×10^{-4}
50	1.16×10^{-4}

existed even for a seal gap of 20 μm, indicating that Navier-Stokes equations can safely be used for such a seal gap.

Similar approach was applied for determining the Knudsen number, K_n for the fluid film geometry and operating pressures in the radial gap air-riding seal. Table 3.18 shows the variation of Knudsen number with varying seal gap.

As the computed values are much lower than 10^{-3}, it can be concluded that Reynolds equation can safely be applied to model the fluid film in the radial gap air-riding seal.

3.3.1 Reynolds Equation for Fluid Film Modelling

Fig. 3.8 shows the geometry of the air-film in the radial-gap air riding seal. L_x and L_z are the length of the film in axial and circumferential direction respectively, and U denotes the velocity of the shaft with respect to the seal ring.

Reynolds equation for describing the pressures in a thin fluid film, neglecting the inertia effect, can be written as [71] :

$$\vec{\nabla}.\left(\frac{-h^3\rho}{12\mu}.\vec{\nabla}p\right)+\frac{U}{2}\frac{\partial}{\partial x}(\rho h)+\frac{\partial}{\partial t}(\rho h)=0 \tag{3.20}$$

For an isothermal process, the gas density (ρ) and pressure (p) are related by the ideal gas equation:

$$\rho=\frac{p}{R_g*T};$$

where, R_g is the gas constant and T is the operating temperature.

Eq. 3.20 is a non-linear equation, so the exact solution for this equation exists for very few cases. To derive an accurate, yet tractable, system of governing equations to model the

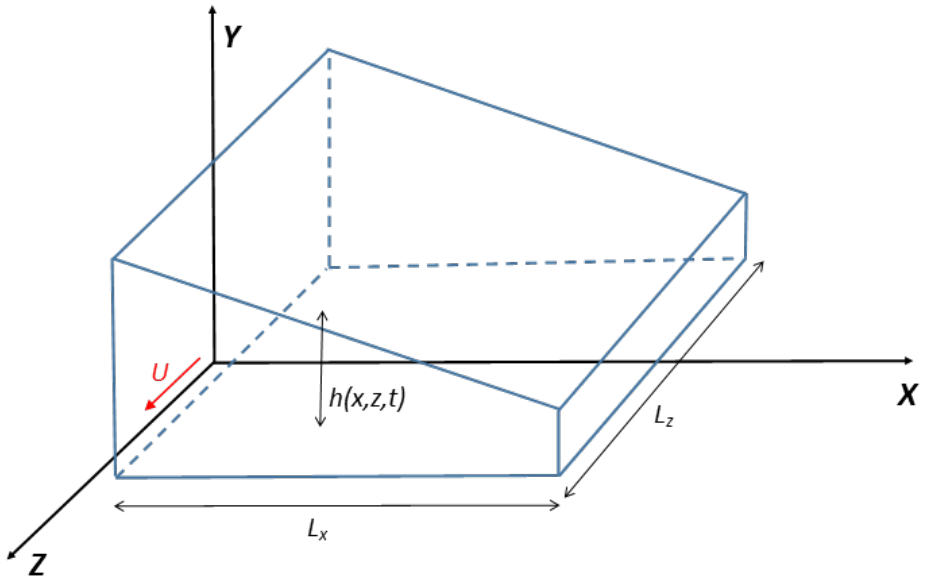


Fig. 3.8 Geometry of the air film

.

air-riding film the Eq. 3.20 is normalised using dimensionless variables and parameters:

$$\bar{x} = \frac{x}{L*}; \quad \bar{z} = \frac{z}{L*}; \quad \tau = \omega t; \quad H = \frac{h}{h*}; \quad P = \frac{p}{p_a}$$

where, $L*$ is the characteristic length of the seal surface, $h*$ is the characteristic film thickness, ω is the whirl frequency (for transient effects) and p_a is the ambient pressure.

So as shown by Castelli & Pirvics and Faria & San Andrés [72, 66], in an isothermal process, the Reynolds equation shown in Eq. 3.20 can be rewritten in a dimensionless form as:

$$\frac{\partial}{\partial \bar{x}}\left(PH^3\frac{\partial P}{\partial \bar{x}}\right) + \frac{\partial}{\partial \bar{z}}\left(PH^3\frac{\partial P}{\partial \bar{z}}\right) = \Lambda\frac{\partial}{\partial \bar{x}}(PH) + \sigma\frac{\partial}{\partial \tau}(PH) \tag{3.21}$$

where,

$$\Lambda = \frac{6\mu U L*}{p_a {h*}^2} \quad \sigma = \frac{12\mu\omega {L*}^2}{p_a {h*}^2} \tag{3.22}$$

Λ and σ are known as the speed number and frequency number respectively. For steady-state analysis, the film thickness (h) and pressure (p) do not vary with time. So there is no squeeze-film effect ($\sigma = 0$). So, Eq. 3.21 reduces to:

$$\frac{\partial}{\partial \bar{x}}\left(PH^3\frac{\partial P}{\partial \bar{x}}\right) + \frac{\partial}{\partial \bar{z}}\left(PH^3\frac{\partial P}{\partial \bar{z}}\right) = \Lambda\frac{\partial}{\partial \bar{x}}(PH) \tag{3.23}$$

For low speed numbers, dimensionless pressure can be expanded as $P = 1 + \Lambda\bar{P}$. So Eq. 3.23 can be simplified as:

$$\frac{\partial}{\partial\bar{x}}\left(H^3\frac{\partial\bar{P}}{\partial\bar{x}}\right)+\frac{\partial}{\partial\bar{z}}\left(H^3\frac{\partial\bar{P}}{\partial\bar{z}}\right)=\frac{\partial}{\partial\bar{x}}(H) \tag{3.24}$$

On the other hand, for large speed numbers Eq. 3.21 can be written as:

$$\frac{1}{\Lambda}\left[\frac{\partial}{\partial\bar{x}}\left(PH^3\frac{\partial P}{\partial\bar{x}}\right)+\frac{\partial}{\partial\bar{z}}\left(PH^3\frac{\partial P}{\partial\bar{z}}\right)\right]=\frac{\partial}{\partial\bar{x}}(PH) \tag{3.25}$$

3.3.2 Numerical Modelling of the Reynolds Equation model

For convenience in modelling analyses, Eq. 3.25 can also be written as:

$$\boxed{\frac{\partial}{\partial\bar{x}}\left(H^3\frac{\partial P^2}{\partial\bar{x}}\right)+\frac{\partial}{\partial\bar{z}}\left(H^3\frac{\partial P^2}{\partial\bar{z}}\right)=2\Lambda.\frac{\partial}{\partial\bar{x}}(PH)} \tag{3.26}$$

A centred finite difference model was used to numerically solve the above equation. Fig. 3.9 shows a hybrid form of 5-point discretisation method for the finite difference scheme.

Using a centred finite difference scheme, first order partial derivative of film-thickness, and first & second order partial derivatives of pressure, with respect to x, can be expressed as:

$$\frac{\partial P}{\partial\bar{x}}=\frac{P_{i+1,j}-P_{i-1,j}}{2\Delta\bar{x}};\quad \frac{\partial h}{\partial\bar{x}}=\frac{h_{i+0.5,j}-h_{i-0.5,j}}{\Delta\bar{x}}$$

$$\frac{\partial^2 P}{\partial\bar{x}^2}=\frac{P_{i+1,j}-2P_{i,j}+P_{i-1,j}}{(\Delta\bar{x})^2}$$

where, i and j are the node indices in the X and Z direction respectively.

For ease of understanding and demonstration, the modelling scheme was applied separately to the left-hand side and right-hand side of the Eq. 3.26.

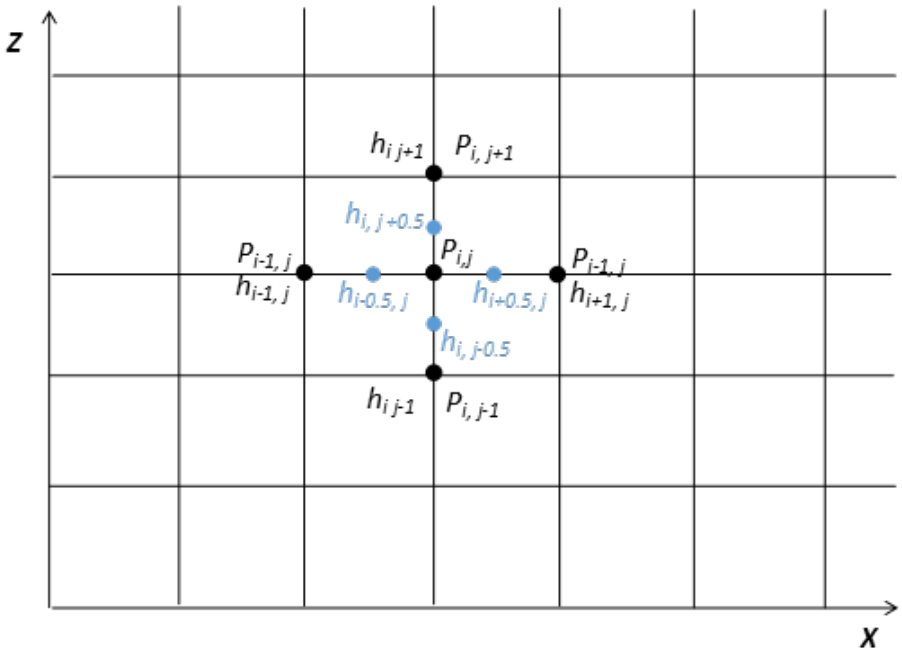


Fig. 3.9 Discretisation method for the Finite Difference model

.

Left-hand side:

$$\frac{h^3_{i+0.5,j}.P^2_{i+1,j}+h^3_{i-0.5,j}.P_{i-1,j}-(h^3_{i+0.5,j}+h^3_{i-0.5,j})P_{i,j}}{(\Delta\bar{x})^2}+\\ \frac{h^3_{i,j+0.5}.P^2_{i,j+1}+h^3_{i,j-0.5}.P_{i,j-1}-(h^3_{i,j+0.5}+h^3_{i,j-0.5})P_{i,j}}{(\Delta\bar{z})^2} \tag{3.27}$$

Right-hand side:

$$\Lambda.\left[P_{i,j}(h_{i+1,j}-h_{i-1,j})+P_{i+1,j}.\left(\frac{h_{i,j}}{\Delta\bar{x}}\right)-P_{i-1,j}.\left(\frac{h_{i,j}}{\Delta\bar{z}}\right)\right] \tag{3.28}$$

On equating the two sides and rewriting the equation by separating each variable and its coefficients:

$$P^2_{i,j}\left(\frac{h^3_{i+0.5,j}+h^3_{i-0.5,j}}{(\Delta\bar{x})^2}+\frac{h^3_{i,j+0.5}+h^3_{i,j-0.5}}{(\Delta\bar{z})^2}\right)+P_{i,j}\left(\Lambda.\frac{h_{i+1,j}-h_{i-1,j}}{\Delta\bar{x}}\right)-P^2_{i,j+1}\left(\frac{h^3_{i,j+0.5}}{((\Delta\bar{z})^2}\right)+\\ P^2_{i,j-1}\left(\frac{h^3_{i,j-0.5}}{(\Delta\bar{z})^2}\right)+P^2_{i+1,j}\left(\frac{h^3_{i+0.5,j}}{(\Delta\bar{x})^2}\right)+P^2_{i-1,j}\left(\frac{h^3_{i-0.5,j}}{(\Delta\bar{x})^2}\right)-P_{i+1,j}\left(\frac{\Lambda h_{i,j}}{\Delta\bar{x}}\right)+P_{i-1,j}\left(\frac{\Lambda h_{i,j}}{\Delta\bar{x}}\right)=0 \tag{3.29}$$

Table 3.4 shows the input parameters used for the analysis.

Table 3.4 Input parameters for Finite Difference Matlab model for 2-D analysis

Parameter	Symbol	Value
Axial length	L	20 mm
Shaft diameter	D	40 mm
Inlet Pressure	P_{in}	4 bar
Outlet Pressure	P_{out}	1 bar
Seal inlet height	h_{in}	50 µm
Seal outlet height	h_{out}	14 µm
Number of axial nodes	n_z	100
Number of circumferential nodes	n_x	100
Density of air (at 25 °C)	ρ	1.184 kg/m^3
Dynamic viscosity of air (at 25 °C)	μ	1.86×10^{-5} Pa-s
Speed Number (for 10000 rpm)	Λ	2.36
Maximum number of iterations	Iterations	3000

As the value of film-thickness is known for the full seal geometry, pressure boundary condition would be sufficient to close the finite difference equation derived in Eq. 3.26. For the numerical calculation, the space was discretised into 100 equally spaced nodal points each along X and Z, and the finite difference scheme is solved using Newton-Raphson method [72] in a Matlab code.

As shown in Fig. 3.10, the pressure values at the inlet and the outlet nodes were fixed at 4 bar and 1 bar respectively. An initial pressure value of 1 bar was allocated to all the other nodes and the pressure at those nodes were recalculated on an iterative manner using (Eq. 3.26).

Convergence criteria was defined as shown in Eq. 3.30. Error limit, ε, was set as 10^{-4}. Grid independence and convergence analysis was carried out to ensure that number of nodes selected and the selected error limit is correct.

$$\frac{\left|\left(\sum_{i=1}^{n_x}\sum_{j=1}^{n_z} P_{i,j}\right)_{iteration\ k} - \left(\sum_{i=1}^{n_x}\sum_{j=1}^{n_z} P_{i,j}\right)_{iteration\ k-1}\right|}{\left|\left(\sum_{i=1}^{n_x}\sum_{j=1}^{n_z} P_{i,j}\right)_{iteration\ k}\right|} \leq \varepsilon \tag{3.30}$$

Fig. 3.11 and Fig. 3.12, respectively, show the pressure profile of the fluid film for a non-rotating & centred shaft and a non-rotating and off-centred shaft (offset of 5 µm in Z). For a non-rotating and centred shaft, the air-film is axisymmetric, so no circumferential

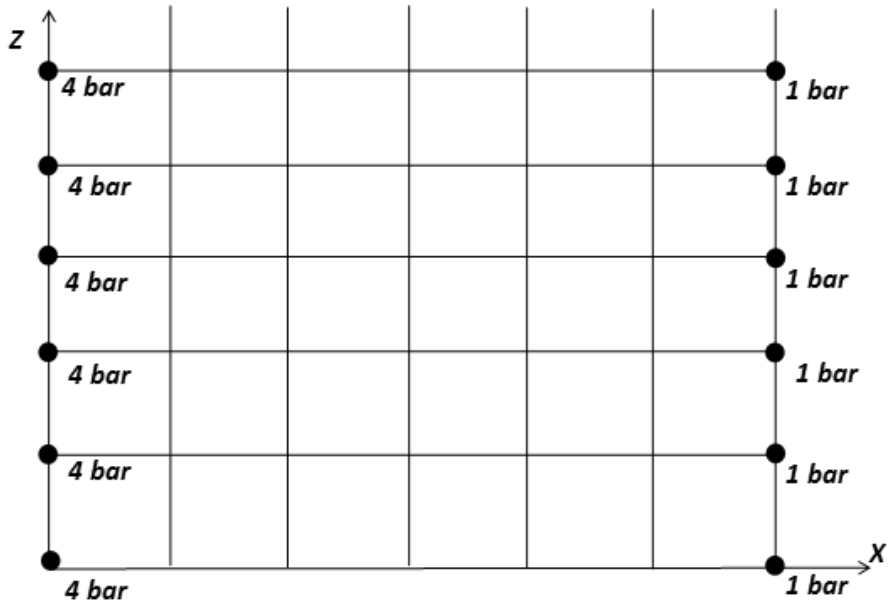


Fig. 3.10 Pressure boundary condition applied to the finite difference model

.

variation in pressure is expected for the same axial position, which is confirmed through the plot shown in Fig. 3.11. For a non-rotating but off-centred shaft, it is expected that there would be a pressure gradient in the circumferential direction as well (due to a change in air-film thickness), which is confirmed in the plot shown in Fig. 3.12. So the phenomenon of hydrostatic lift generation in the film can be observed from the increase in pressure values of the fluid film in Fig. 3.12, when the shaft is offset by 5 µm in Z.

The shaft is then set to rotate at a speed of 10000 rpm. Fig. 3.13 and Fig. 3.14, respectively, show the pressure distribution in the fluid film for a rotating shaft (10000 rpm) in a centred and offset condition. Although the presence of a lifting force can be observed from Fig. 3.14, the lack of any substantial difference in pressure profile between the static and dynamic case suggest that the observed lift is mostly generated by hydrostatic means.

To compare the pressure values obtained from the 1-D and 2-D analysis, the pressure values obtained from the 2-D analysis (for a centred shaft) was averaged in the circumferential direction, and the resultant 1-D pressure profile was compared to the one obtained from 1D analysis. As shown in Fig. 3.15, a significant rise in pressure values was observed in the 2-D analysis. This may be attributed to fact that not only does the 1-D model fail to account for the flow in the circumferential direction, the equation that was used was actually derived for incompressible flow and compressibility of the fluid was approximated by re-evaluating the density at every node (assuming the properties of an ideal gas).

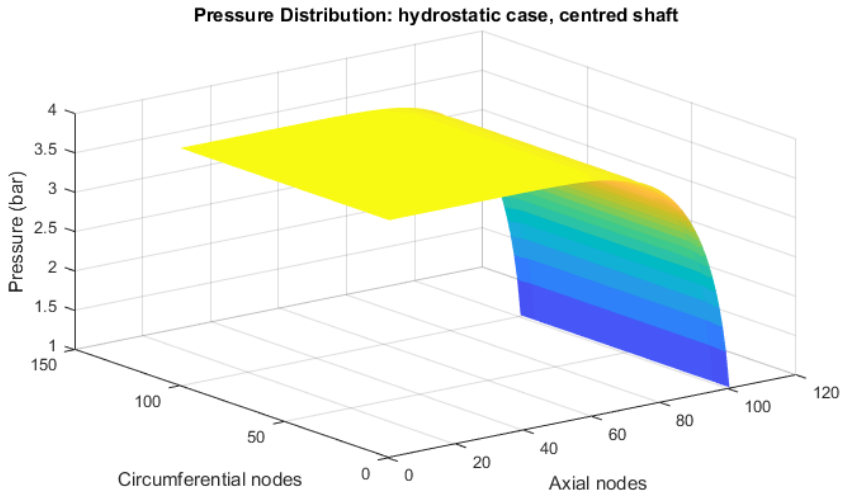


Fig. 3.11 Pressure profile of the fluid film for a non-rotating and centred shaft

.

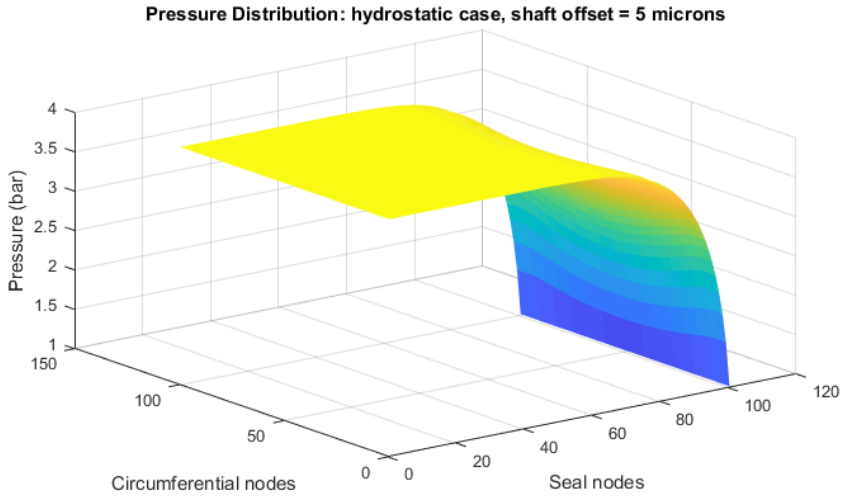


Fig. 3.12 Pressure profile of the fluid film when the shaft is non-rotating and it is off-centred by 5µm

.

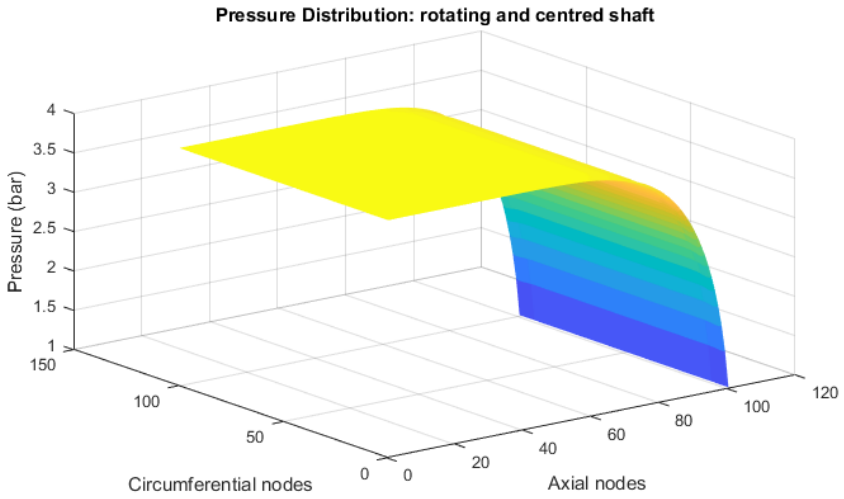


Fig. 3.13 Pressure profile of the fluid film for a centred shaft rotating at 10000 rpm

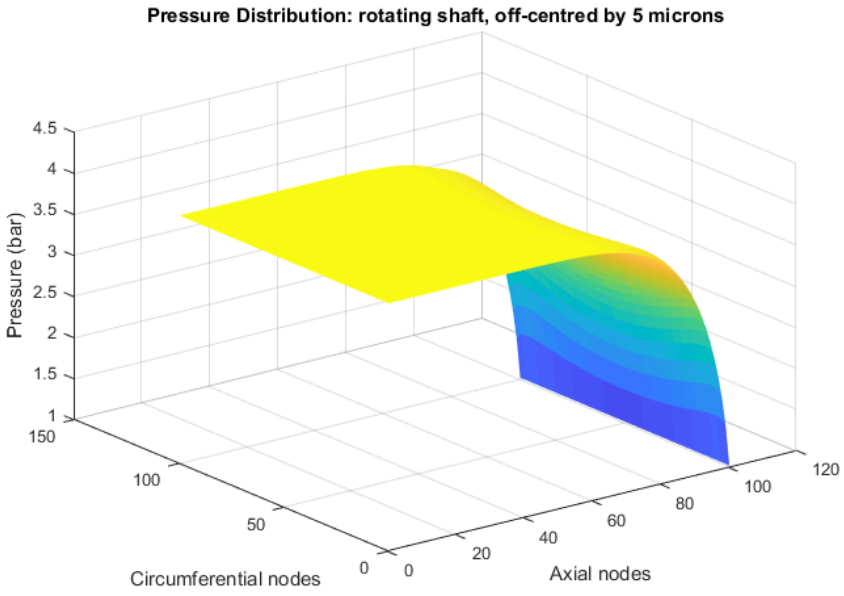


Fig. 3.14 Pressure profile of the fluid film when the shaft is rotating at 10000 rpm and it is offset by 5µm

.

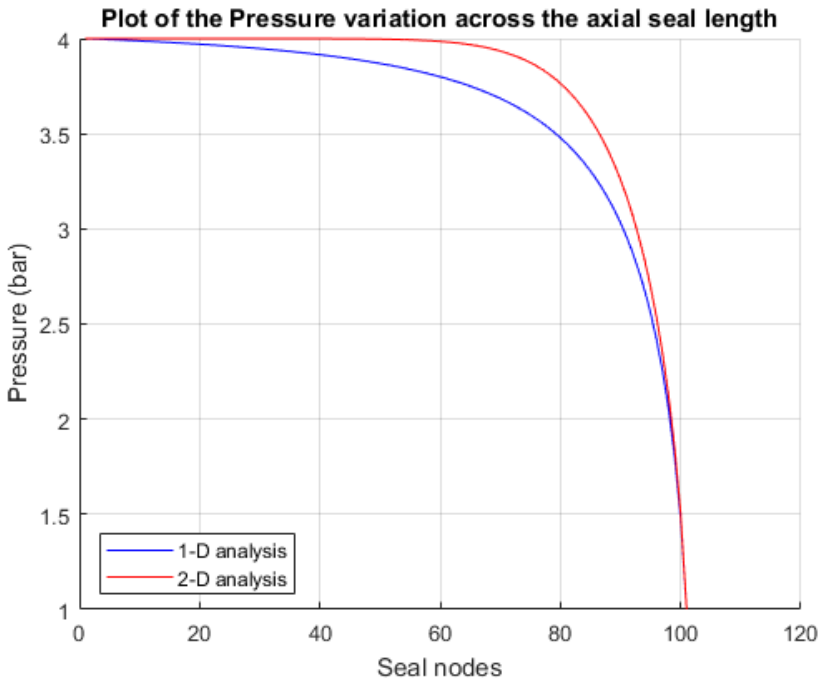


Fig. 3.15 Comparison of the axial pressure drop obtained from the 1-D and 2-D analysis

.

3.3.3 Stiffness Matrix

Most analyses consider gas bearings and seals as two degrees of freedom mechanical elements with lateral forces reacting to radial displacements in directions Y and Z. Bearing rotordynamic force coefficients are changes in reaction forces due to small amplitude motions about an equilibrium position. The equation of motion for linearised model of a gas bearing/gas seal can be written (in matrix notation) as:

$$\mathbf{M}\ddot{\mathbf{q}} + \mathbf{C}\dot{\mathbf{q}} + \mathbf{K}\mathbf{q} = \mathbf{F}(t) \tag{3.31}$$

where, M, C and K are referred to as the mass or inertia matrix, damping matrix and stiffness matrix, respectively. $\mathbf{q}(t)$ is generalised displacement and $\mathbf{F}(t)$ is the generalised force. The stiffness matrix, K can be evaluated from steady state analysis, as it is not time dependant. For small perturbations along Y and Z direction, the stiffness matrix can be expressed as:

$$K = \begin{bmatrix} K_{yy} & K_{yz} \\ K_{zy} & K_{zz} \end{bmatrix} \tag{3.32}$$

As the fluid film is axisymmetric, the stiffness matrix will be skew-symmetric. In other words, $K_{yy} = K_{zz}$ and $K_{yz} = -K_{zy}$. Similar to 1-D analysis, the lift force acting in the Y and Z direction was evaluated by calculating the difference of net forces acting in the Y and Z direction for the centred shaft and the offset shaft. The lift forces were then divided by the offset value to obtain the stiffness coefficients.

$$K = 1 \times 10^6. \begin{bmatrix} 1.85 & -0.02 \\ 0.02 & 1.85 \end{bmatrix} \mathrm{N/m} \tag{3.33}$$

It is observed that the direct film stiffness derived from the 2-D analysis is 1.85 MN/m is a bit higher than the value of 1.75 MN/m obtained from the 1-D analysis, but the values are quite comparable so it can be stated that the two analyses correlate well with each other and give comparable results. A further comparison with the results CFD simulations has been shown in Chapter 5.

The direct film stiffness value calculated from 1-D and 2-D equation was then computed for different pressure ratios. As observed from Fig. 3.16, direct film stiffness increases almost linearly with increasing pressure ratio. It is also interesting to note that the direct stiffness values of 2-D analysis seem to increase linearly throughout whereas the direct stiffness values from 1-D analysis seems to keep diverging from the 2-D analysis values.

Film stiffness was also computed for different seal outlet height, as shown in Fig. 3.17, for a constant seal inlet height of 50 µm. It can be observed that the film stiffness decreases progressively with increasing seal outlet height and it becomes negative for seal outlet height $\geq$ 50 µm, i.e. when the seal gap is diverging or near parallel. Based on this observation, it can be concluded that for generating a positive hydrostatic film stiffness, a converging seal gap is needed.

It is crucial to the stability of the seal that the fluid film has a positive stiffness. A negative stiffness would imply that negative lift force will act on the seal ring if the shaft is off-centred, which will move the seal ring towards the shaft and cause rubbing. As shown in 3.17 a diverging seal or near parallel seal gap can lead to a negative stiffness. Several factors may lead to a diverging seal gap like tilting of the seal ring, manufacturing errors, wear and tear etc. All these factors have prevented to ensure that a positive fluid film stiffness is maintained.

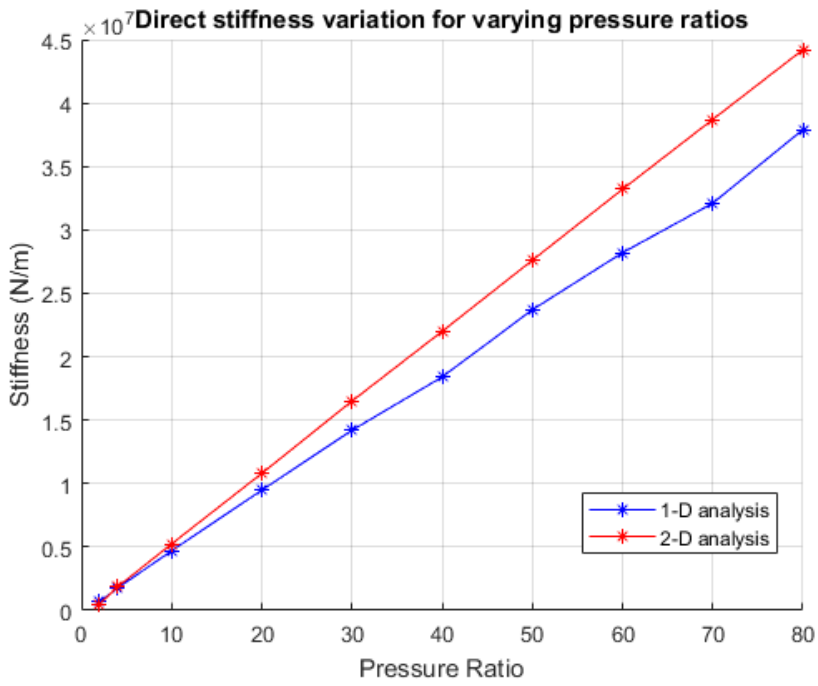


Fig. 3.16 Variation of film stiffness with increasing pressure ratio

.

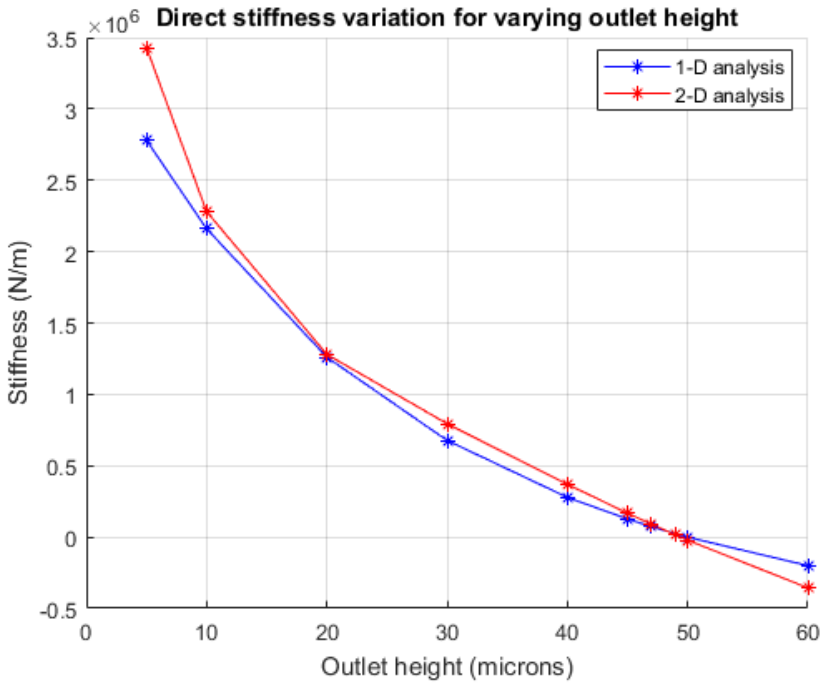


Fig. 3.17 Variation of film stiffness with varying seal outlet height for a pressure ratio of 4

.

3.3.4 Dynamic Coefficients of the fluid film

In addition to the static coefficients of the seal, it is important to consider the dynamic coefficients as well. In a gas bearing, instabilities occur at certain speeds where the static equilibrium position is no longer stable dynamically and the rotor begins to undergo a self-excited whirl in a small orbit around the equilibrium position. It has been seen that the whirl frequency, $\bar{\omega}$, usually coincides with the lowest natural frequency of the rotor system. Lund [38] stated that system critical mass M_c can be calculated as:

$$M_c = \frac{\kappa_{eq}}{(\bar{\omega})^2} \tag{3.34}$$

where, κ_{eq} is the equivalent dynamic stiffness. κ_{eq} can be derived from the equation:

$$\kappa_{eq} = \frac{K_{yy}C_{zz} + K_{zz}C_{yy} - K_{yz}C_{zy} - K_{zy}C_{yz}}{C_{yy} + C_{zz}} \tag{3.35}$$

where, $C_{yy}, C_{zz}, C_{yz}, C_{zy}$ are the coefficients of the damping matrix C.

$$C = \begin{bmatrix} C_{yy} & C_{yz} \\ C_{zy} & C_{zz} \end{bmatrix} \tag{3.36}$$

Eq. 3.35 will used to evaluate the dynamic coefficients in Section 5.4.6 in Chapter 5, once the damping coefficients have been derived.

3.4 Summary and Discussion

The methodology and results from 1-D and 2-D analysis of the fluid film were discussed in this chapter.

The seal geometry and seal assembly schematics were designed to match the operational requirements from a radial gap air-riding seal. Knudsen number analysis carried out on the fluid film geometry, with stated input parameters, confirmed the validity of applying Navier-Stokes equation for modelling the fluid film of the air-riding seal. 1-D analysis carried out on the fluid film geometry confirmed the hydrostatic lift generation feature of the fluid film, which was an essential requirement for generating a fluid film with positive stiffness. Stiffness of the air-film was calculated by offsetting the shaft and calculating the net lift force

generated by the squeezing action on the air film. From the 1-D analysis, the film stiffness was calculated as 1.75MN/m.

Reynolds equation was used as a governing equation to develop a 2-D model for the fluid film in the air-riding seal. A modified form of Reynolds equation, based on the seal geometry and input parameters, was derived from the classical Reynolds equation for fluid film bearings. A central finite difference modelling scheme was developed to numerically solve the derived form of Reynolds equation. The finite difference model was solved in an iterative manner using Newton-Raphson method in Matlab till the solution matched the required convergence criteria. Pressure profiles were calculated for rotating and non-rotating shafts for centred and off-centred condition. Significant hydrostatic lift was generated in the air-film but negligible lift force was generated through hydrodynamic means. The direct air-film stiffness was computed as 1.85 MN/m, which compared well against the direct stiffness value of 1.75 MN/m calculated from 1D analysis. The hydrostatic film stiffness, achieved through the high differential pressure across the axial ends of the seal, was considered to be sufficient to drive the seal ring during any perturbations in the system. The possibility of adding some grooves in the seal/shaft surface could be explored in future if additional film stiffness is desired.

On studying the variation of direct film stiffness with varying pressure ratios it was evident that stiffness varies linearly with pressure ratios. It was also noted that the direct stiffness values from 1-D analysis seem to diverge from the values calculated from 2-D analysis with increasing pressure ratio. On studying the variation of direct stiffness with varying seal outlet height, it was also observed that a converging seal gap is necessary for generating positive film stiffness.

Although the air film modelling based on Reynolds equation was able to provide a better estimation of the air film properties, it was still necessary to understand the transient performance of the air film for various shaft perturbations and movements. Chapter 4 explains the CFD analysis carried out on the full seal geometry to characterise the air film properties more accurately.

Chapter 4

CFD Modelling - Overview and Verification Study

In the previous chapter, the seal geometry design and a schematic of the radial gap air-riding seal assembly was established. 1-D and 2-D analyses were carried out for the air film in the seal to understand the properties of the thin film. The results indicated that sufficient air-film stiffness could be achieved to support the seal ring, but a need for developing a more detailed analysis was identified. So CFD modelling was carried out to develop a better understanding of the full seal system and to study the interaction between the seal ring and the fluid film.

This chapter gives an overview of the underlying concepts for the various parameters that will be employed for the CFD simulations, and explains the model set-up for the CFD analyses. ANSYS Workbench 16.1 was used as the platform to build and analyse the model, and all CFD simulations were carried out on ANSYS CFX.

4.1 Flow Equations

4.1.1 Overview

The governing equations describing fluid flows are basically a set of mathematical expressions underlining the conservation laws in physics. The conservation laws can be summarised as:

- The mass of each fluid particle is conserved.

- The rate of change of momentum on a fluid particle is equal to the sum of forces acting on it (Newton's second law of motion), which is the principle behind Navier-Stokes equations.
- The change of energy of a fluid particle is equal to the sum of the heat flux and work done on it (corollary to the first principle of thermodynamics)

The above equations when expressed in mathematical terms, are referred-to as continuity, momentum, and energy equations respectively. In the following subsections, each of the above equations is reported for a continuum fluid.

4.1.2 Continuity Equation

The continuity equation states that, for a given control volume, the rate of variation of mass within the volume is equal to the net rate of mass flow. This can be expressed as:

$$\frac{\partial \rho}{\partial t} + \nabla.(\rho \mathbf{u}) = 0 \tag{4.1}$$

where, ρ is the fluid density and $\mathbf{u}$ is the flow velocity vector. The first term on the left-hand side of Eq. 4.1 is the time derivative of the fluid density within the control volume, while the second term is the net outflux of mass from the control volume.

4.1.3 Momentum Equation

For an incompressible fluid, the conservation of momentum equation, as described by the convective form of Navier-Stokes equation, can be written as:

$$\frac{\partial \rho \mathbf{u}}{\partial t} + \nabla.(\rho u \mathbf{u}) = -\nabla p + \mu \nabla^2 \mathbf{u} + \frac{1}{3}\mu \nabla(\nabla.\mathbf{u}) + \rho g + S_m \tag{4.2}$$

In 4.2, the inertial terms on the left hand side are the unsteady and convective acceleration per unit volume, respectively. These are balanced by the pressure term (∇p), viscous stress terms ($\mu \nabla^2 \mathbf{u}$ & $\frac{1}{3}\mu \nabla(\nabla.\mathbf{u})$), the body force ($\rho g$), and the source term ($S_m$) which accounts for the effect of additional body forces.

4.1.4 Energy Equation

The energy conservation equation can be written in the following form:

$$\frac{\partial}{\partial t}(\rho E) + \nabla.(\mathbf{u}(\rho E + p)) = -\nabla.(k_{eff}\nabla T) + S_h \tag{4.3}$$

where, E is the internal energy of the given fluid particle, and k_eff the effective thermal conductivity, defined as

$$k_eff = k + k_t \tag{4.4}$$

where k is the fluid thermal conductivity and k_t its turbulent thermal conductivity, which depends on the turbulence model used.

4.2 Turbulence Modelling

4.2.1 The Reynolds-Averaged Navier-Stokes (RANS) Equations

In turbulent flows, flow fields such as velocity and pressure vary with time in a random manner. To completely model the turbulent fluctuations of the flow, for example using Detached Eddy Simulations (DES), would be very time consuming and would require large amounts of computational power. A popular approach for modelling the turbulent fluctuations is expressing the flow variables as the sum of their mean value and the statistical value of their fluctuations, as discussed in [73]. For instance, the velocity field is usually defined as:

$$u(t) = U + u'(t) \tag{4.5}$$

where U is the mean flow velocity and $u'(t)$ is the oscillating, time-dependent component. The introduction of this definition of the solution variables into the Navier-Stokes equations Eq. 4.2 leads to their turbulent form which cannot be solved in practical terms because of the typically wide ranges of eddy length scales and time scales required to describe the flow [73].

Therefore, mean flow equations are derived to account for the effect of turbulence without explicitly modelling every single oscillation in the flow field. The latter expressions, known as Reynolds equations, introduce additional unknowns in the form of normal and tangential stresses. The resulting flow equations are the Reynolds-Averaged Navier-Stokes (RANS) equations. A thorough discussion on their derivation can be found in the books of Versteeg

and Malalasekera [73] and Wilcox [74]. In the index notation, RANS can be written as:

$$\rho\frac{\partial U_i}{\partial t}+\rho U_j\frac{\partial U_i}{\partial x_j}=-\frac{\partial p}{\partial x_i}+\frac{\partial}{\partial x_j}\left(2\mu S_{ji}-\overline{\rho u'_j u'_i}\right) \tag{4.6}$$

where, S_{ji} is the mean strain rate tensor and $-\overline{\rho u'_j u'_i}=\tau_{ij}=\tau_{ji}$ is the Reynolds stress tensor. The latter introduces additional terms that do not permit the analytical closure of the turbulence problem [74], due to the non-linearity of the Navier-Stokes equations.

In Reynolds stress models, the correlations that are unknown in the computation of the Reynolds stress tensor are expressed as a function of known flow properties in order to close the turbulence problem. The underlying assumption is that the Reynolds stress tensor is the product between the mean strain rate tensor and an eddy viscosity (Boussinesq hypothesis).

Several models have been introduced over the years to compute the turbulent viscosity. These include zero-equation models such as Prandtl's mixing length model, (zero-equation indicates that no additional transport equations are needed), one-equation models such as the Spalart-Allmaras, and two-equation models, including the $k-\varepsilon$ and $k-\omega$ models. The Prandtl model relies on the concept of mixing length, in an analogy with the mean free path of molecules in a gas. It assumes that the turbulent viscosity is proportional to the mixing length scale, being valid for relatively simple cases where the latter flow-dependent quantity is known. The Spalart-Allmaras model solves one transport equation for a modified expression of the turbulent viscosity, known as kinematic eddy viscosity. The model performs well in general for external aerodynamic flows [75].

Two-equation models rely on the description of turbulence as composed of eddies, and on the consequent theory of energy cascade. The latter states that, in a turbulent flow, large eddies tend to break-up into progressively smaller eddies, characterised by lower kinetic energy. The energy content can be quantified as a function of the wave number $\kappa=\frac{2\pi}{\lambda}$ (where λ is the wavelength of the eddies) through the spectral energy $E(\kappa)$ [73]. The spectral energy is defined as the kinetic energy of the eddy per unit mass and per unit wave number at the given wave number κ.

Kolmogorov stated that, to maintain the energy balance in turbulent flows, the production rate of turbulent energy due to the generation of large vortices needs to be broadly in equilibrium with its rate of dissipation. Dimensional analysis led to find that the ratios between small and large velocity, length and time scales can be expressed as a function of the Reynolds number of the large eddies, thus relating microscopic flow properties with the physical behaviour at macroscopic scale. An example for these correlations can be found in [73]. Kolmogorov's work led to describe the turbulent viscosity as a function of the

turbulence kinetic energy k, associated with the large eddies, and the turbulence dissipation rate ε, describing the smallest eddies. Two-equation models rely on this theory. Notably, the $k-\varepsilon$ model describes the turbulent viscosity as proportional to k^2/ε, while the $k-\omega$ model describes it as proportional to k/ω, with ω defined as the specific turbulence dissipation rate.

One main limitation of RANS-based models is that the behaviour of all eddies is captured by one single turbulence model. The limitation lies in the fact that the evolution of the largest eddies is highly dependent on the nature of the problem, which makes the development of widely applicable RANS turbulence models challenging. The Large Eddy Simulation (LES) approach addresses this problem by solving the largest eddies with a time-dependent simulation, while modelling the smallest, isotropic eddies in a way analogous to the RANS models. A cut-off length scale separates the resolved and the unresolved eddies. The latter process is known also as 'filtering' of the Navier-Stokes equations. The effect of unresolved eddies on the large eddies is accounted for by sub-grid-scale (SGS) stresses, which are modelled separately.

The main limitations of the LES are the large computational overhead linked with the unsteady nature of the model, in particular when compared to two-equation models [73], and the strong dependency of the results on the definition of the error . The latter aspect implies that the model validation is case-specific, whereas there may be limitations on data available for particular flow cases. Alternative methods to the LES include the Unsteady Reynolds-Averaged Navier-Stokes (URANS) equations [76] and the Detached-Eddy Simulation [77].

As the simulation of two-phase flows adds a degree of complexity to the analyses performed in this thesis work, the application of turbulence models having a higher level of detail than two-equation models may lead to significant challenges in terms of computational requirements. Moreover, the lack of examples in the literature based on similar applications suggests that robust validation is yet to be achieved for the cases considered. For this reason, the modelling choices for this work have been limited to the widely-adopted two-equation models, namely the $k-\varepsilon$, $k-\omega$ and their variants.

4.2.2 The $k-\varepsilon$ model

The $k-\varepsilon$ model, usually defined as 'standard' in the form proposed by Launder and Spalding in 1974 [78] is a widely used two-equation model which relies on the computation of turbulence kinetic energy k and its dissipation rate ε. The main assumption is a fully turbulent flow. The model solves transport equations for both k and ε, with the first derived

from the exact equation, and the latter relying on closure approximations obtained through physical reasoning. The standard k-ε equations can be written as:

$$\frac{\partial}{\partial t}(\rho k)+U_i\frac{\partial}{\partial x_j}(\rho U_j k)=\frac{\partial}{\partial x_j}\left(\frac{\mu_t}{\sigma_\varepsilon}\frac{\partial k}{\partial x_j}\right)+\mu_t\frac{\partial U_i}{\partial x_j}\left(\frac{\partial U_i}{\partial x_j}+\frac{\partial U_j}{\partial x_i}\right)\frac{\partial U_i}{\partial x_j}-\rho\varepsilon \tag{4.7}$$

$$\frac{\partial}{\partial t}(\rho \varepsilon)+U_i\frac{\partial}{\partial x_j}(\rho U_j \varepsilon)=\frac{\partial}{\partial x_j}\left(\frac{\mu_t}{\sigma_\varepsilon}\frac{\partial \varepsilon}{\partial x_j}\right)+C_{\varepsilon 1}\frac{\varepsilon}{k}\mu_t\frac{\partial U_i}{\partial x_j}\left(\frac{\partial U_i}{\partial x_j}+\frac{\partial U_j}{\partial x_i}\right)-\rho C_{\varepsilon 2}\frac{\varepsilon^2}{k} \tag{4.8}$$

where,

$$\mu_t=\frac{\rho C_\mu k^2}{\varepsilon} \quad \omega=\frac{\varepsilon}{C_\mu k}$$

$$C_{\varepsilon 1}=1.44 \quad C_{\varepsilon 2}=1.92 \quad C_\mu=0.09 \quad \sigma_\varepsilon=1.3$$

The main concern with the $k-\varepsilon$ model is its treatment of the boundary layer. The boundary layer can be split into two sections, the viscous sub-layer by the wall and the logarithmic sub-layer. The $k-\varepsilon$ model is unable to resolve the flow through the viscous sub-layer of the boundary layer, and therefore has to use complex wall functions to produce a profile at the wall without it being resolved. So, for some situations, like for flows with adverse pressure gradients, this model can prove to be quite inaccurate.

4.2.3 The RNG $k-\varepsilon$ model

The RNG $k-\varepsilon$ model is a derivation of the standard $k-\varepsilon$ model that relies on the renormalization group (RNG) technique. RNG technique is a statistical method used to model physical systems in which the properties are described by formulae having a similar expression at different size scales. The underlying principle is that the problem can be renormalized to solve only a sample of the system, thus reducing the size of the model. The RNG method was first implemented in turbulence modelling by Forster *et al.* [79] in 1977, to study the effect of a Gaussian random force on the velocity fluctuations of a flow governed by the Navier-Stokes equation. A comprehensive description of the RNG theory and its application to turbulence modelling is given in Yakhot and Orszag [80].

In ANSYS CFX, the transport equations for RNG $k-\varepsilon$ model is the same as the $k-\varepsilon$ model, but the value of the constants change (as shown below).

$$C_{\varepsilon 1RNG} = 1.44 - f_n \qquad C_{\varepsilon 2RNG} = 1.68 \qquad C_{\mu RNG} = 0.085 \qquad \sigma_{\varepsilon RNG} = 0.7179$$

where,

$$f_n = \frac{\eta(1-\frac{\eta}{4.38})}{1+\beta_{RNG}\eta^3} \qquad \eta = \sqrt{\frac{P_k}{\rho C_{\mu RNG}\varepsilon}}$$

4.2.4 The $k-\omega$ model

The $k-\omega$ is a two-equation turbulence model based on the approach proposed by Wilcox [74]. It accounts for the effects of low Reynolds numbers, compressibility, and shear flow spreading. The basic structure of the model is similar to the $k-\varepsilon$ model, as two transport equations are solved to compute the turbulent viscosity needed to close the RANS equations Eq. 4.6. The major difference between the $k-\omega$ model and $k-\varepsilon$ model is that the specific dissipation rate ω is used in the $k-\omega$ instead of the dissipation rate ε used in the $k-\varepsilon$ model. The transport equations can be written as:

$$\frac{\partial}{\partial t}(\rho k) + U_i\frac{\partial}{\partial x_j}(\rho U_j k) = \frac{\partial}{\partial x_j}\left(\frac{\mu_t}{\sigma_\omega}\frac{\partial k}{\partial x_j}\right) + \mu_t\frac{\partial U_i}{\partial x_j}\left(\frac{\partial U_i}{\partial x_j}+\frac{\partial U_j}{\partial x_i}\right)\frac{\partial U_i}{\partial x_j} - \rho k\omega \tag{4.9}$$

$$\frac{\partial}{\partial t}(\rho \omega) + U_i\frac{\partial}{\partial x_j}(\rho U_j \omega) = \frac{\partial}{\partial x_j}\left(\frac{\mu_t}{\sigma_\omega}\frac{\partial \omega}{\partial x_j}\right) + \alpha\frac{\omega}{k}\mu_t\frac{\partial U_i}{\partial x_j}\left(\frac{\partial U_i}{\partial x_j}+\frac{\partial U_j}{\partial x_i}\right) - \beta\rho\omega^2 \tag{4.10}$$

where,

$$\mu_t = \frac{\rho k}{\omega} \qquad \varepsilon = \beta^*\omega k$$

$$\alpha = 5/9 \qquad \beta = 0.075 \qquad \beta^* = 0.09 \qquad \sigma_\omega = 2$$

The $k-\omega$ model is able to resolve through the viscous sub-layer and are known to provide good results for adverse pressure gradients as well. However, they require more boundary layer elements which leads to an increase in computational costs.

4.2.5 The SST $k-\omega$ model

The Shear Stress Transport (SST) modification of the $k-\omega$ model was introduced by Menter [81] to improve the prediction accuracy of flows where separation occurs and significant adverse pressure gradients are present. In principle, the SST model relies on blending functions to switch between the near-wall formulation of the $k-\omega$ model and the freestream formulation of the $k-\varepsilon$ model. Following this approach, the shortcomings of the $k-\varepsilon$ in the solution of the near-wall layers and those of the standard $k-\omega$ in the solution of freestream regions are overcome [82]. As the SST model is based on a zonal formulation, the computation of the wall distance is required, thus adding complexity to the model compared to the standard $k-\varepsilon$ and $k-\omega$.

The SST $k-\omega$ transport equations have a similar form to those of the standard $k-\omega$ model:

$$\frac{\partial}{\partial t}(\rho k)+U_i\frac{\partial}{\partial x_j}(\rho U_j k)=\frac{\partial}{\partial x_j}\left(\frac{\mu_t}{\sigma_\omega}\frac{\partial k}{\partial x_j}\right)+\mu_t\frac{\partial U_i}{\partial x_j}\left(\frac{\partial U_i}{\partial x_j}+\frac{\partial U_j}{\partial x_i}\right)\frac{\partial U_i}{\partial x_j}-\rho k\omega \tag{4.11}$$

$$\frac{\partial}{\partial t}(\rho \omega)+U_i\frac{\partial}{\partial x_j}(\rho U_j \omega)=\frac{\partial}{\partial x_j}\left(\frac{\mu_t}{\sigma_\omega}\frac{\partial \omega}{\partial x_j}\right)+\alpha\frac{\omega}{k}\mu_t\frac{\partial U_i}{\partial x_j}\left(\frac{\partial U_i}{\partial x_j}+\frac{\partial U_j}{\partial x_i}\right)-\beta\rho\omega^2+D_\omega \tag{4.12}$$

The only additional term in the SST $k-\omega$ transport equations is the cross-diffusion D_ω, which is defined to blend the $k-\varepsilon$ model into the $k-\omega$ formulation. It is expressed as:

$$D_\omega=2(1-F_1)\rho\frac{1}{\omega\sigma_{\omega,2}}\frac{\partial k}{\partial x_j}\frac{\partial \omega}{\partial x_j} \tag{4.13}$$

where,

$$F_1=\tanh({\Phi_1}^4) \tag{4.14}$$

$$\Phi_1=min\left[max\left(\frac{\sqrt{k}}{0.09\omega y},\frac{500\mu}{\rho y^2\omega}\right),\frac{4\rho k}{\sigma_{\omega,2}D_\omega^+ y^2}\right] \tag{4.15}$$

where, y is the distance to the next surface and D_ω^+ is the positive part of D_ω.

4.2.6 Near Wall Modelling

The presence of solid walls in contact with the fluid has a significant effect on turbulent flows. As on the wall surface the fluid is static, high velocity gradients are generally present in the region in proximity of the wall. This near-wall region is known as boundary layer, and can be divided into an inner region, composed of three sublayers, and an outer region.

In the first sublayer, i.e. the closest to the wall, the flow tends to behave as laminar due to the high viscosity linked with the high tangential velocity gradients. This region is normally referred as the viscous sublayer. Moving further from the wall, a buffer zone characterised by a transition from laminar to turbulent flow is found, followed by a region where turbulence has a significant effect on the flow behaviour. This part of the boundary layer is divided into the log-law region and the outer region.

To better evaluate the turbulent characteristics of the flow depending on the wall distance, the non-dimensional quantities y^+ and u^+ are typically used.

$$y^+ = \frac{\rho U_\tau y}{\mu} \tag{4.16}$$

where, U_τ is the shear velocity, proportional to the wall shear stress τ_ω

$$U_\tau = \sqrt{\frac{\tau_\omega}{\rho}} \tag{4.17}$$

Considering its formulation and meaning, the y^+ number can be regarded as a flow Reynolds number based on the distance from the wall. Low y^+ values ($y^+ < 30$) characterise the viscous sublayer, in which the mean flow velocity depends only on the variables defining y^+ in Eq. 4.16 [73]. Instead, in the region $30 < y^+ < 500$ the mean flow velocity is proportional to the natural logarithm of the wall distance, as shown below:

$$u^+ = \frac{1}{\kappa} \ln y^+ + C \tag{4.18}$$

where, $\kappa = 0.41$ is the Karman constant. C ranges between 5.5 and 8.5; it is derived from data fitting and it is function of the local roughness, with $C \approx 5.5$ for a hydraulically smooth surface. Eq. 4.18 is also known as log law.

In CFD, two approaches are generally adopted to model the inner region of the boundary layer. The first method, for example the one used in the standard $k-\omega$ model, fully resolves the boundary layer with a fine computational grid, extended through the viscous sublayer.

This technique implies that a certain number of cells, of the order of 10, need to be placed in the region $y^+ < 30$.

However, for high Reynolds number flows, the boundary layer can be extremely thin compared to the geometry to be modelled, implying that a large number of high aspect ratio cells may be required to resolve the viscous sublayer. Moreover, the cell size needs to grow away from the wall at a finite rate, typically 'geometrically', in order to avoid large discontinuities. Since this can lead to very large mesh requirements and convergence issues arising from high cell aspect ratios, a second approach based on wall functions is commonly used in CFD. With this second method, implemented in the $k-\varepsilon$ model, the flow velocity profile in the inner boundary layer is computed based on the correlations seen in Eq. 4.16 - Eq. 4.18.

The wall function approach described above is known as standard wall function. In some flow cases, mesh constraints can make it challenging to meet its wall y^+ requirements in the whole domain. For this reason, some models, such as scalable wall functions and the enhanced wall treatment, incorporate adjustments to meet the required conditions. Scalable wall functions address cases in which the centroid of the near-wall cell falls within the viscous sublayer, i.e. its y^+ value is too low.

Although wall functions are typically used in $k-\varepsilon$ models, near-wall corrections are available also in $k-\omega$ models.

4.3 Preliminary Modelling and Verification Study

ANSYS Workbench 16.1 was used as the parent platform for carrying out CFD and structural analysis of the model. Fig. 4.1 shows the geometry of the model created on ANSYS Design Modeler. As it can be observed, the model contains both the structural and fluid bodies. The solid bodies were suppressed for carrying out CFD simulations on the fluid domain. The dimensions of the fluid volumes are given in Table 4.1.

Table 4.1 Dimensions of the fluid volumes used for CFD analysis

Part	Inner Diameter (mm)	Outer Diameter (mm)	Length (mm)
Seal Air-film	40	40.028(min.) - 40.1 (max.)	20
Supporting Assembly	40	54	80
Outlet Volume	40	100	120

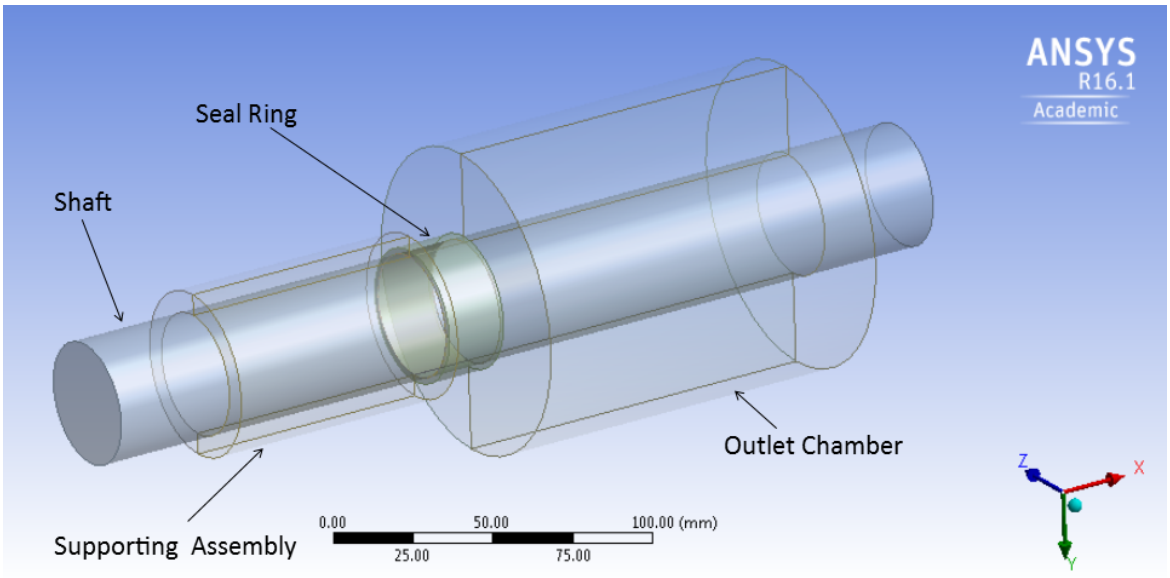


Fig. 4.1 Simplified fluid and structural model set-up in ANSYS Design Modeler

.

The geometry of the fluid domain was then imported in ANSYS Meshing. It is worth mentioning that the 3 fluid bodies (i.e. seal air-film, supporting assembly or secondary seal film, and the outlet volume) were combined to form a single part in Design Modeler. This leads to a generation of conformal mesh when the meshing is done for the fluid domain. Non-conformal meshes have been known to induce some inaccuracy in the results, and as the fluid-fluid interface in this geometry lies at critical locations (inlet and outlet of the seal air-film), a conformal mesh was preferred to a non-conformal one.

A structured hexahedral mesh was created by using the 'Sweep' method. The Sweep method can be applied on a model that revolves around an axis, where the source and target faces share a topology. Sweep 'number of divisions' indicates the number of cells that are created along the direction of sweep and the 'sweep bias' option allows the user to have an increasing/decreasing number of nodes towards the source and/or the target face. Fig. 4.2 shows a cut-section (by X-Y plane) view of the swept mesh on the full fluid domain.

As it may be observed from Fig. 4.3, 9 cells have been swept in the seal gap of 14 μm, and the maximum growth rate of the elements is restricted to 20%.

The mesh is then imported to the ANSYS CFX-Pre software where the model is set-up for CFD simulations. SST $k-\omega$ turbulence model has been used for all the simulations as shortcomings of the $k-\varepsilon$ in the solution of the near-wall layers and those of the standard $k-\omega$ in the solution of freestream regions are overcome [82]. The details of the steady state and transient simulation set-up will be explained in detail in the next chapter.

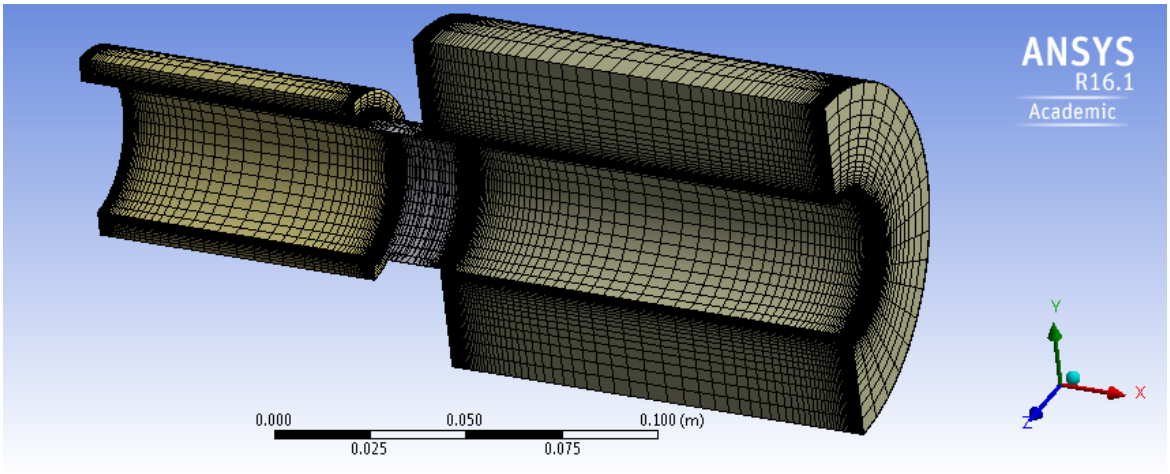


Fig. 4.2 Structured hexahedral meshing of the fluid domain

.

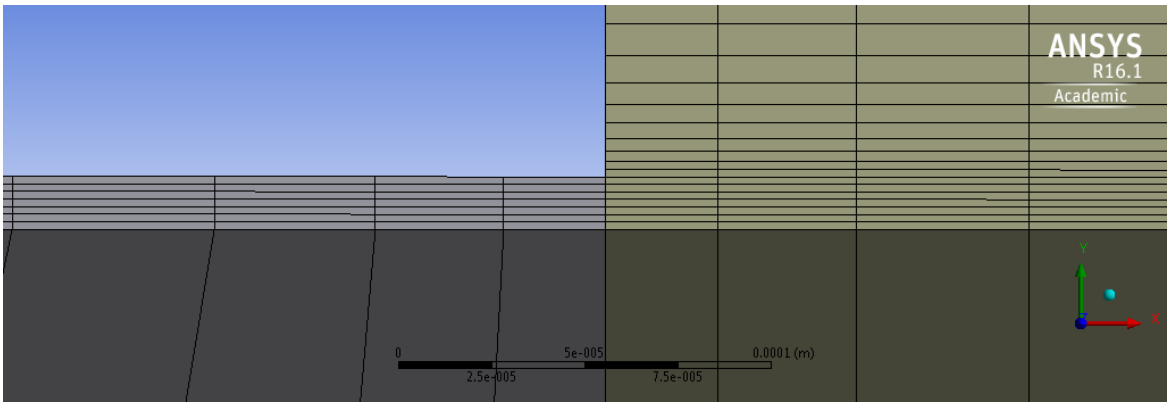


Fig. 4.3 Zoomed-in view showing the mesh at the interface between seal air-film outlet and the outlet volume

.

4.3.1 Grid Independence Study

Table 4.2 shows the input parameters for the CFD simulation carried out for the grid verification study.

Table 4.2 Grid independence study - Input parameters for the CFD simulation

Parameter	Value
Inlet Pressure	4 bar
Outlet Pressure	1 bar
Shaft rotation speed	10000 rpm
Temperature at inlet	25 °C
Temperature at outlet	25 °C
Turbulence model	$k-\omega$ SST

Convergence criteria for the simulation was set as follows:

- Residuals, including the mass continuity, momentum and turbulence are monitored until the root means square (RMS) values have reduced to 10^{-4} or below.
- Three monitor values are set up: lift force (F_y), mass flow rate at inlet ($\dot{m}_{in}$) and mass flow rate at ($\dot{m}_{out}$). Solution is deemed to have converged when the variations in the values of these parameters are less than 1 % for the last 100 iterations, and $\dot{m}_{in} = \dot{m}_{out}$, as shown in 4.4.

A review of prior CFD simulation efforts for modelling hydrodynamic seals didn't reveal any substantial evidence to indicate a preference towards a specific turbulence model. After Menter [81] developed the $k-\omega$ SST model for aerodynamic flows, various authors have used this model for CFD simulations of thin films (bearings, electrical machines etc.) [83–85] and high speed jets [86]. So $k-\omega$ SST model was used for the grid independence analysis.

Grid independence is determined by using the structured meshes detailed in the Table 4.3. The initial mesh, Mesh 1, was created by opting for 4 sweep number of divisions in the seal air-film, and changing the various edge sizing and bias values, to create a mesh which respects the 'best practices' in CFD. This process was repeated for Mesh 2, and Mesh 3, where the sweep number of division were chosen as 3, 5 and 7 respectively. Leakage rate $\dot{m}_{out}$ was chosen as the critical monitoring criterion for grid convergence.

It can be observed from Table 4.3 that for 401,750 nodes, the change in leakage rate from the previous mesh is less than 1%. So it could be concluded that for mesh sizes of 401,750 nodes and above, the solution can be considered to be independent of grid size.

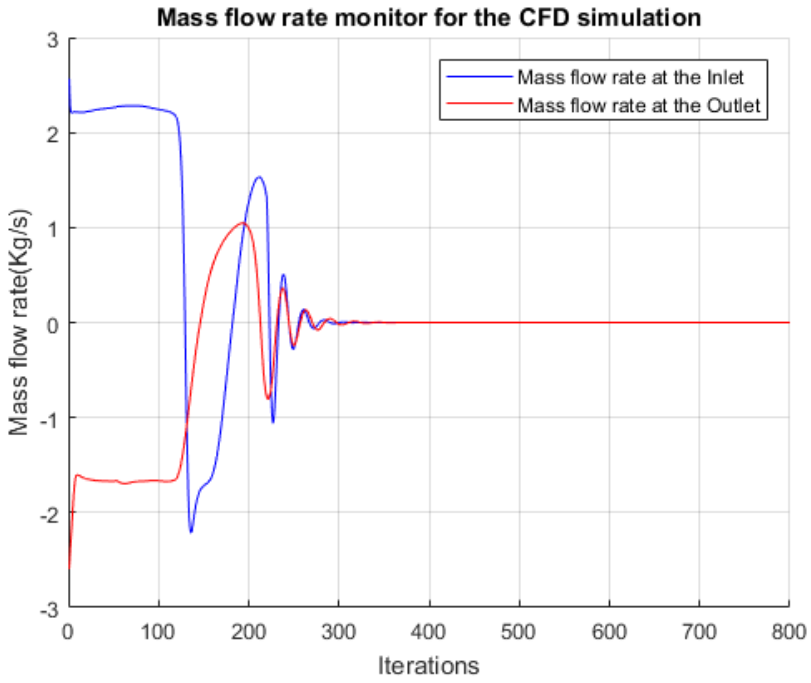


Fig. 4.4 Variation of mass flow rate at the inlet and outlet through the steady state CFD simulation

.

Table 4.3 Grid independence study - Details of the meshes used

Mesh	Number of nodes	Sweep division in air-film	% change in leakage rate $\dot{m}_{out}$
Mesh 1	200,160	3	N/A
Mesh 2	362,485	5	6.2
Mesh 3	401,750	7	0.76

As discussed in Section 4.2.6, for $k-\omega$ and $k-\omega$ SST, it is desirable to have y^+ values as low as possible. Common practice in CFD is to have $y^+ < 5$ for $k-\omega$ SST model, but higher values of y^+ are acceptable as long as the solution satisfies the grid independence criteria. Fig. 4.5 shows the variation of y^+ values on the seal air-film surface.

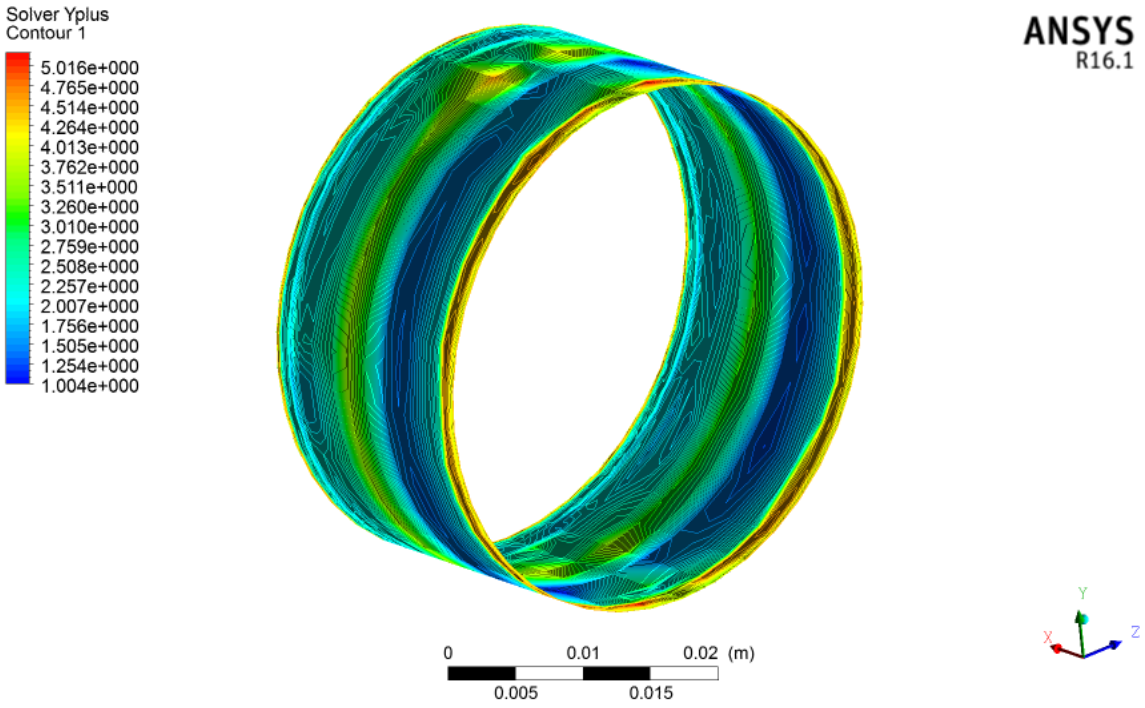


Fig. 4.5 y^+ values on the seal air-film surface

.

Shaft roughness has not been accounted for in these studies. Shaft roughness may lead to some turbulence formation. This can be explored in future research work on the seal. For the studies described in 5.5, it was found that flow convergence to steady state got slower with both decreasing the seal gap and increasing the pressure ratio. Converged steady state solution could not be obtained for seal gap of < 5µm. Variation of inlet temperature and shaft rotation speed didn't seem to have any significant effect on solution convergence. There was minor increase in direct film stiffness with increase in inlet temperature and shaft rotation speed. Fig. 4.6 shows the variation of film stiffness with increase in inlet temperature.

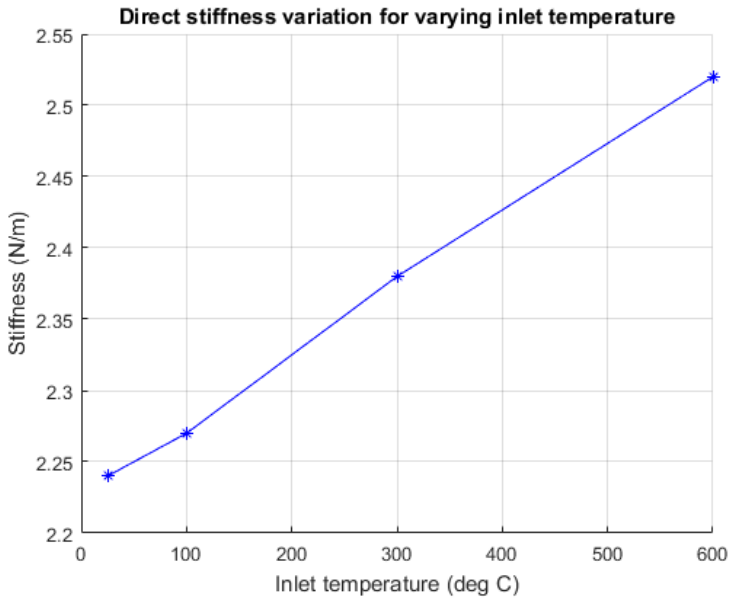


Fig. 4.6 Variation of direct film stiffness with inlet temperature

.

4.4 Summary and Discussion

In this chapter, the underlying concepts & principles behind CFD simulations were discussed, and a preliminary modelling set-up and verification study was carried out.

The equations describing the flow of fluid, which form the basis of all CFD codes, were explained briefly. This was followed by a detailed investigation on some of the most popular turbulence models used in CFD. In Section 4.2.6, near wall modelling approaches were discussed and the importance of y^+ and u^+ in understanding the turbulent characteristics of the flow was highlighted. The turbulence model used for all CFD studies in the thesis is the SST $k-\omega$ model.

A preliminary model was set-up in ANSYS CFX and a grid independence study was carried out. The study suggested that for a grid size of 401,750 nodes and above, the solution will independent of grid size. A contour map was created for the y^+ values on the air-film surface and the y^+ value was found to be less than 5.

The next chapter explains the settings and results of steady-state and transient CFD analyses carried out on the fluid film.

Chapter 5

CFD Modelling - Steady State and Transient Analyses

Chapter 4 provided a general background on CFD simulations and the grid independence study verified the validity of mesh created on the geometry for carrying out CFD simulations.

In this chapter the model set-up in CFX-Pre, for steady-state and transient simulations, will be explained in details. The results of from the CFD analysis will be discussed and they will be compared to the results obtained through 1-D and 2-D analysis.

In terms of time dependence, flow characteristics can either be specified as steady-state or transient. Steady-state simulations are those whose characteristics do not change with time and the various fluid parameters (like velocity, pressure etc.) are assumed to have been reached a steady state after a relatively long time interval. In other words, no time information is required to describe the fluid parameters in a steady state analysis.

Transient simulations require real time information to determine the time intervals at which the CFX-Solver calculates the flow field [87]. Transient behaviour can be caused by the changing boundary conditions of the flow or it can be inherently related to the flow characteristics. In analyses carried out in this thesis, transient simulations are performed to understand the flow characteristics for small perturbations on the seal system. To run transient simulations on ANSYS CFX, both physical time steps and the maximum number of coefficient iterations per time step need to specified.

5.1 Steady-State Analysis

5.1.1 Fluid Domain Settings

Regions of fluid flow and/or heat transfer in CFX are called domains. For the CFD models presented in this thesis, a single fluid domain was constructed, including the 3 fluid bodies (supporting assembly or secondary seal, seal air-film and outlet volume). Table 5.1 shows the setting/values selected for the fluid parameters in the full fluid domain.

Table 5.1 Steady-state CFD: Fluid Domain settings

Property/Parameter	Value/Setting
Fluid material	Air Ideal Gas
Reference Pressure	0 bar
Heat Transfer	Total Energy
Turbulence Model	$k-\omega$ SST

Air Ideal Gas is used as the fluid material as this activates compressible flow model in CFX. For modelling high-speed compressible flows (transonic or supersonic), CFX recommends the use the total energy heat transfer model [87].

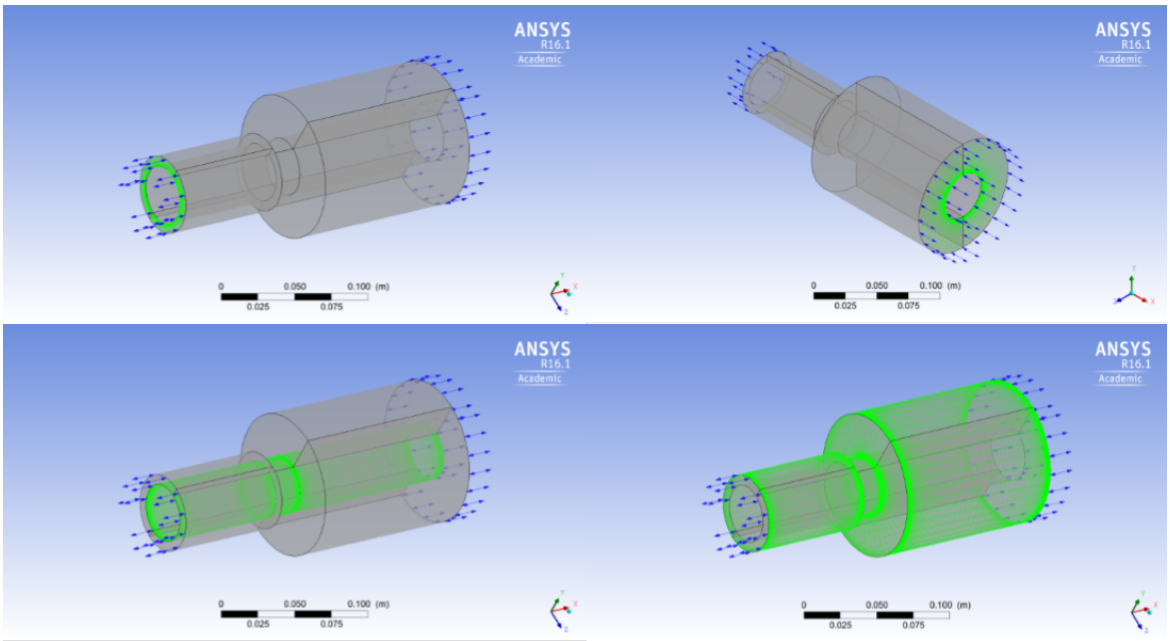


Fig. 5.1 Boundary conditions for the CFD simulations (clockwise from top left): Inlet, Outlet, Outer Wall, Inner Wall

.

Fig. 5.1 shows the locations of the boundary condition applied for the CFD analysis. The parameter values set on these boundaries are as follows:

- Inlet: This was defined as an 'opening'. CFX recommends a boundary to be defined an opening when the full prescription of information at that location is not well known; for example, if the value of pressure is known, but the direction of flow is unknown. For an 'inlet' type condition, any flow reversal at the boundary is known to cause convergence issues and simulation failures. Pressure was set as 4 bar, temperature as 25 °C and flow direction was set as normal to boundary condition.
- Outlet: It was also defined as an opening for similar reasons as stated above. Pressure was set as 1 bar, temperature as 25 °C, turbulence intensity as medium and flow direction was set as normal to boundary condition.
- Outer Wall: This was set as a no-slip, smooth wall with adiabatic heat transfer.
- Inner Wall: This was set also set as a no-slip, smooth wall with adiabatic heat transfer but it was additionally assigned a rotational velocity of 10000 rpm about the X-axis.

5.1.2 Solver Settings

Table 5.2 enlists the parameter settings used in solver control. The default and preferred timescale selection for the simulation is the Auto Timescale option. Auto Timescale is a fluid timescale control option that uses an internally calculated physical time scale based on the boundary conditions, flow conditions, physics, and domain geometry [87]. The Timescale Factor(TF) option, set automatically to a default value of 1, can be used to multiply the Auto Timescale. TF was set through a CEL expression to change the TF with the number of iterations (shown as '$iterations$' in next paragraph). CFX Expression Language (CEL) is an interpreted, declarative language that enables CFX users to enhance their simulations [87].

For $1 \leq iterations < 50$, $TF = 0.01$, for $50 \leq iterations < 120$, $TF = 0.05$, for $120 \leq iterations < 220$, $TF = 0.1$ and for $iterations \geq 220$, $TF = 0.5$. This leads to timesteps of 7.2×10^{-7}s, 4.2×10^{-6}s, 8.39×10^{-6}s and 4×10^{-5}s. This was set by monitoring the residuals and ensuring that the convergence criteria is met.

As already mentioned in Section 4.3.1, 3 monitor points were set-up for the simulations: lift force (F_y), mass flow rate at the inlet ($\dot{m}_{in}$) and mass flow rate at the outlet($\dot{m}_{out}$).

Table 5.2 Steady-state CFD: Solver settings

Parameter	Value/Setting
Advection Scheme	High Resolution
Maximum Iterations	800
Timescale Factor	Varying from 0.01 to 0.5 (CEL expression)
Convergence Criteria - Residual Target	1×10^{-6} (RMS)

5.2 Steady-State Simulation Results

To visualise the results from the steady state analysis, the fluid domain is sliced through by an X-Y plane and the contour plots of various parameters are plotted on this plane. Fig. 5.2 illustrates the velocity contour plotted on the plane. Fig. 5.3 shows a zoomed-in view (of the seal exit) of the velocity contour at the seal outlet.

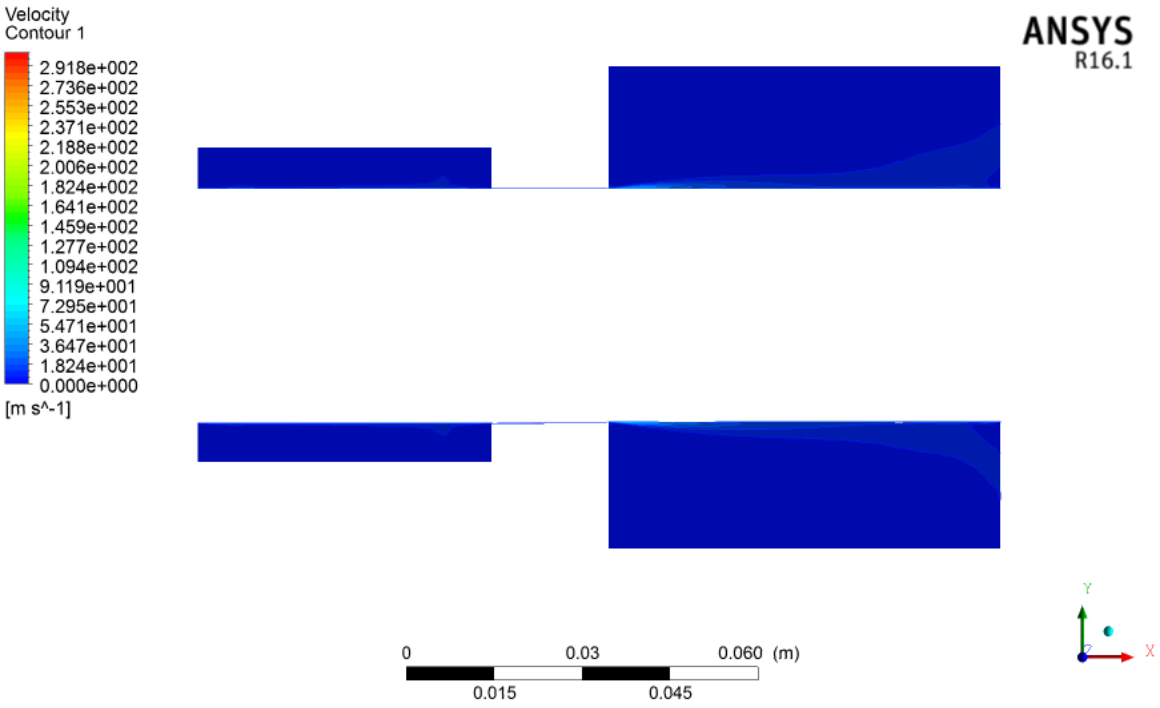


Fig. 5.2 Velocity variation across an axial section of the full seal assembly

.

The high exit velocity at the seal outlet can be visualised through Fig. 5.3. Fig. 5.2 shows evidence of zones of flow recirculation in the inlet volume (secondary seal) and outlet volume. Fig. 5.4 shows the variation of pressure near the seal outlet.

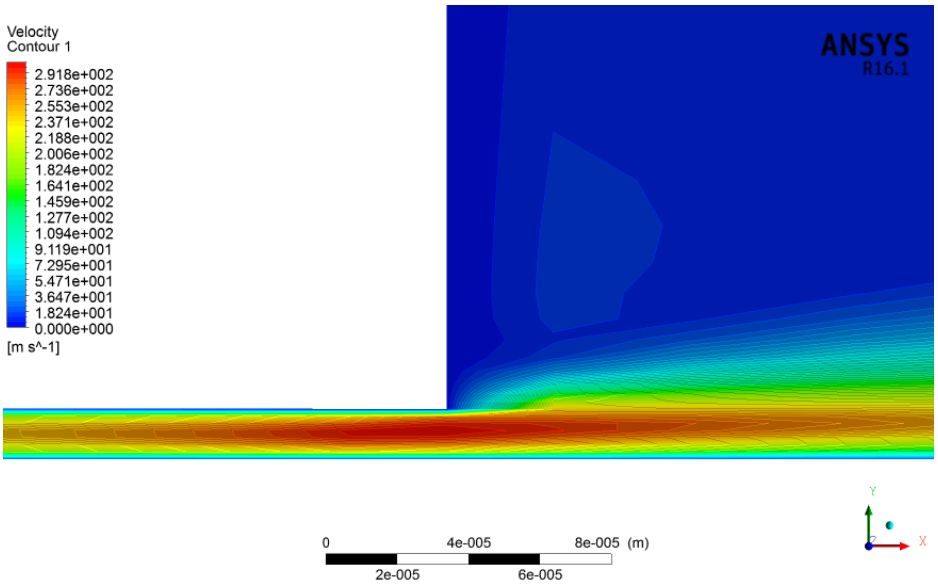


Fig. 5.3 Zoomed-in view of the velocity contour at the seal outlet

.

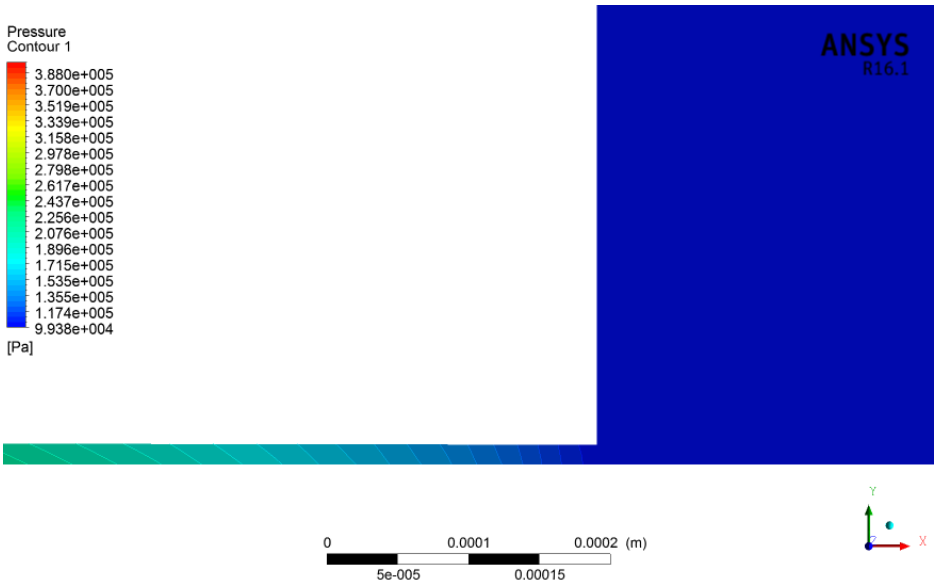


Fig. 5.4 Pressure variation near the seal outlet

.

The leakage rate was found to be 0.0017 kg/s. In order to correlate the results from steady state simulations with the 1-D and 2-D analysis, pressure values along a line passing through the middle of the air-film is plotted. Fig. 5.5 shows the comparison between the pressure variation plots evaluated from 1-D, 2-D and CFD analysis. It is observed that there is a noticeable difference in the pressure values calculated from the 1-D analysis and those calculated from CFD analysis, but a very good correlation in pressure values can be observed between the 2-D and CFD results. This is further proved by calculating the RMS (Root Mean Square) of the difference between each pair of results, as shown in Table 5.3.

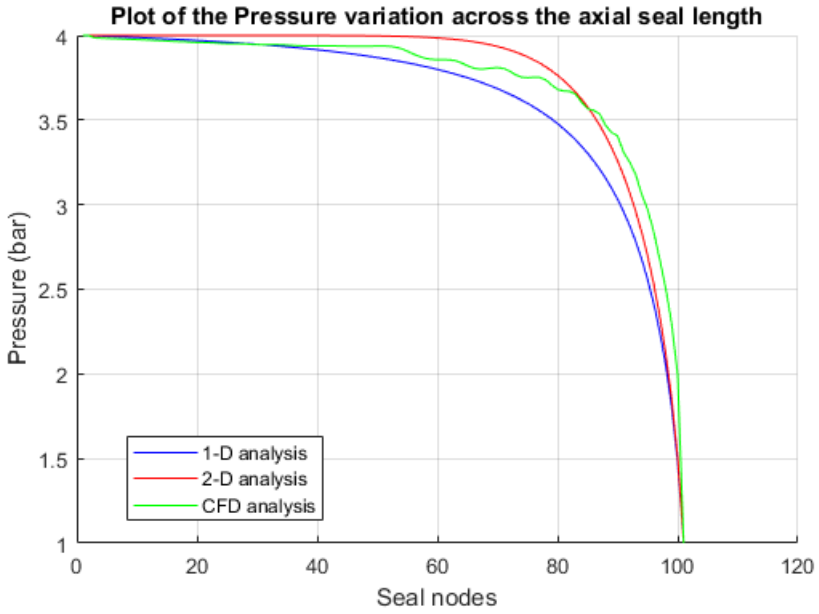


Fig. 5.5 Comparison of the the pressure variation plots evaluated from 1-D, 2-D and CFD analysis

.

Table 5.3 Analysis of the diffrence between the pressure values calculated from 1-D, 2-D and CFD analysis

Pair of results analysed	Root Mean Square (RMS) of the difference
1-D and 2-D	$\varepsilon_{RMS,1D-2D} = 0.1599$
1-D and CFD	$\varepsilon_{RMS,1D-CFD} = 0.1755$
2-D and CFD	$\varepsilon_{RMS,2D-CFD} = 0.1250$

5.3 Stiffness Matrix

The linearised expression of the force on the air-riding seal film can be written as:

$$\begin{Bmatrix} F_y \\ F_z \end{Bmatrix} = \begin{bmatrix} K_{yy} & K_{yz} \\ K_{zy} & K_{zz} \end{bmatrix} \begin{Bmatrix} y \\ z \end{Bmatrix} + \begin{bmatrix} C_{yy} & C_{yz} \\ C_{zy} & C_{zz} \end{bmatrix} \begin{Bmatrix} \dot{y} \\ \dot{z} \end{Bmatrix} \tag{5.1}$$

A discussion on the damping matrix C can be found in Section 5.4.5 in this chapter. As discussed in Section 3.3.3, stiffness matrix can be evaluated from steady state analyses. Considering that the system reaches a steady state after a small radial displacement in (Y,Z), the equation of motion is reduced to:

$$\begin{Bmatrix} F_y \\ F_z \end{Bmatrix} = \begin{bmatrix} K_{yy} & K_{yz} \\ K_{zy} & K_{zz} \end{bmatrix} \begin{Bmatrix} y \\ z \end{Bmatrix} \tag{5.2}$$

So, from Eq. 5.2 it can be inferred that the value of the stiffness coefficients can be evaluated if the force and displacement matrices are known.

Steady state CFD analyses are carried out, with different values of shaft offset in Y and Z and resultant changes in force on the fluid film in Y and Z direction are recorded, as shown in Table 5.4.

Table 5.4 Steady state analyses for different shaft offset values

Y offset (µm)	Z offset (µm)	F_y (N)	F_z (N)
0	0	0.002	-0.001
1	0	2.242	-0.122
0	1	-0.085	2.261

So, the stiffness matrix of the fluid-film is calculated as:

$$K = 1 \times 10^6 \begin{bmatrix} 2.24 & -0.121 \\ 0.087 & 2.262 \end{bmatrix} \text{ N/m} \tag{5.3}$$

There should be no net force acting on the seal for a centred shaft but some non-zero force values are observed, but as these values are quite small ($\sim$ 2mN), they can be ignored as numerical error. It can be observed that the calculated direct stiffness value (K_{yy}) of 2.24 MN/m is slightly higher than those calculated from 1-D and 2-D analysis, i.e. 1.75 MN/m and 1.85 MN/m respectively.

5.4 Fluid-Structure Interaction Analysis

Fluid-Structure interaction (FSI) is a multi-physics coupling between the laws that describe the dynamics of the fluid and structural mechanics. This phenomenon is characterized by interactions between a deformable or moving structure and an external or internal fluid flow.

FSI can be used to study a phenomenon where a fluid flow deforms a physical structure, which in turn changes the fluid flow, or vice-versa. This two-way interaction loop continues through multiple cycles, possibly resulting in deformation of the structure and/or undesired change in fluid flow characteristics.

In ANSYS Workbench, 2-way FSI analysis is possible by coupling ANSYS CFX with ANSYS Mechanical. Communicating data between CFX and the Mechanical application is effectuated by the using the ANSYS Multi-field solver (MFS). Data is communicated between the CFX and the Mechanical application field solvers through standard internet sockets using a custom client-server communication protocol [87]. The MFS solver uses iterative coupling where each physics is solved sequentially and each matrix equation is solved separately. The solver iterates between each physics field until the loads that are transferred across physics interfaces converge.

To carry out FSI analysis in CFX, fluid and solid domain/physical models need to be defined in the CFX-Pre and the Mechanical application user interfaces, respectively. The specification of coupling data transfers and controls are also required to be set-up in the CFX-Pre user interface. Execution and run-time monitoring of the coupled simulation is performed in the CFX-Solver Manager.

Two different FSI analyses were carried out on the model, which will be discussed in the next couple of sections.

5.4.1 Study-1: Response to Shaft Motions

In this study, an external sinusoidally varying force of the form of Eq. 5.4 was applied to shaft in Y direction. The seal ring was assumed to be fixed(stationary) and the movement of the shaft in the fluid film (in the $Y-Z$ plane) was recorded, in response to the excitation frequency vibrations. The shaft is described as a mass, as shown in Table 5.5.

$$F_{ext} = -F_0 \sin(\omega t) \tag{5.4}$$

where, F_0 is the amplitude of the oscillating force, and ω is the angular velocity. Simulations are carried out for different frequency values to understand the behaviour of the fluid film at different excitation frequencies.

The key input parameters, which differ from steady-state analysis, are listed below:

- Transient analysis is selected in analysis settings.
- The Inner Wall boundary (as shown in Fig. 5.1) is selected as a 'Rigid Body'.
- Mesh motion is defined in terms of 'Displacement Relative to Previous Mesh'.
- In boundary conditions, mesh motion for Inlet and Outlet (Fig. 5.1) is set as 'Unspecified', while it is set as stationary for Outer Wall and 'Rigid Body Solution' for Inner Wall.

In CFX, a 'Rigid Body' is defined as a solid object that moves through a fluid. Its motion is dictated by the fluid forces and torques acting upon it, along with any external forces (such as gravity) and external torques.

Table 5.5 shows the parameter settings for the Rigid Body domain to define the shaft properties and movement.

Table 5.5 FSI Study1 - Rigid Body Settings

Parameter	Value/Settings
Location	Inner Wall
Mass	1 kg
Force in Y	F_{ext}
Translational degree of freedom	X and Y

Solver Settings

Table 5.6 illustrates the solver settings for the transient FSI simulation of shaft vibration.

Table 5.6 FSI Study1 - Solver Settings

Parameter	Value/Settings
Timesteps	2×10^{-6}s
Number of timesteps	1250
Maximum number of coefficient loops	20

Maximum number of coefficient loops indicate the maximum inner iteration within each outer loop iteration to reach the desired convergence value for residuals (RMS - 10^{-5}).

Additional monitor points (apart from the ones previously stated in Section 4.3.1) are introduced for the transient simulations - F_y (force in Y direction), F_z (force in Z direction), Y_{shaft} (shaft displacement Y direction) and Z_{shaft} (shaft displacement Z direction).

Domain initialisation is necessary to start a transient simulation. The steady state solution (from Section 5.2) is imported as the initial solution file before starting the simulation run. There are a couple of important factors that need to be considered while monitoring a transient FSI run in order to avoid solution inaccuracies:

1. Convergence criterion should be met for each time step (i.e. the inner loop solution should converge before the maximum number of coefficient loop iteration is reached)
2. Courant number should be not exceed 100.

The Courant number is an important factor that should be considered for modelling transient flows in CFD. It can be written as:

$$Courant = \frac{u\Delta t}{\Delta x} \tag{5.5}$$

where, u is the fluid speed, Δt is the timestep and Δx is the mesh size. The Courant number calculated in ANSYS CFX is a multidimensional generalization of this expression where the velocity and length scale are based on the mass flow into the control volume and the dimension of the control volume [87].

For explicit CFD methods, the timestep must be chosen such that the Courant number is sufficiently small, usually of the order of unity. As ANSYS CFX is an implicit code, it does not require the Courant number to be small for stability, but it is still recommended to have a Courant number of less than 100.

5.4.2 Study-1: Results

For the first test, frequency is set to 600Hz, and F_0 is set as 5 N.

Fig. 5.6 shows the resultant shaft displacement along Y and Z from the FSI analysis, when the oscillating force F_{ext} is applied to the shaft along Y direction.

Fig. 5.7, shows the displaced mesh near the seal outlet during one of the transient timesteps.

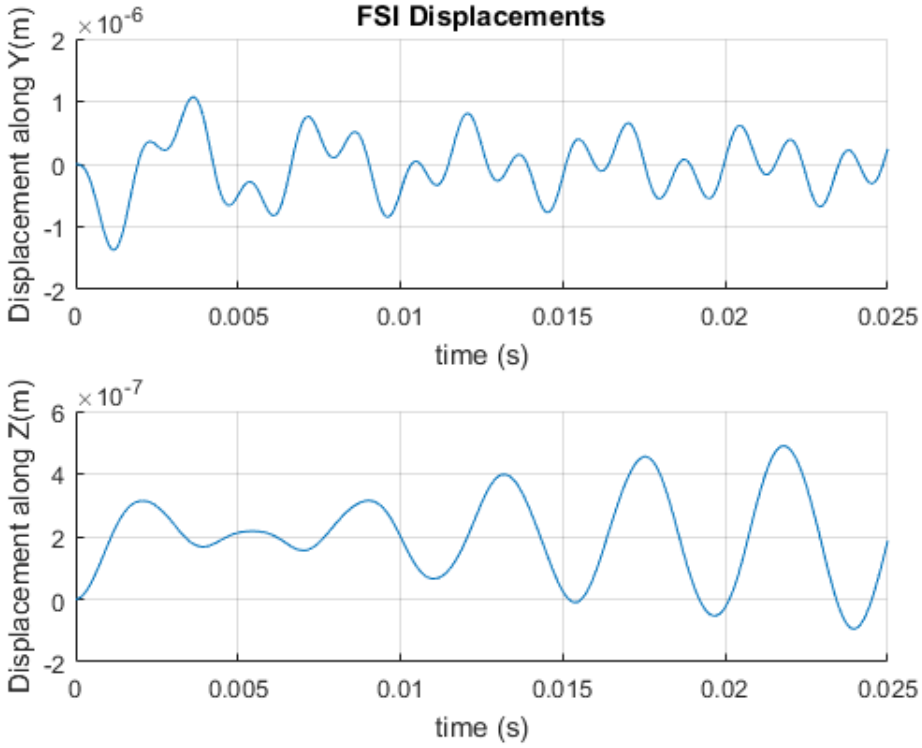


Fig. 5.6 Resultant displacement from F_{ext} applied along Y

.

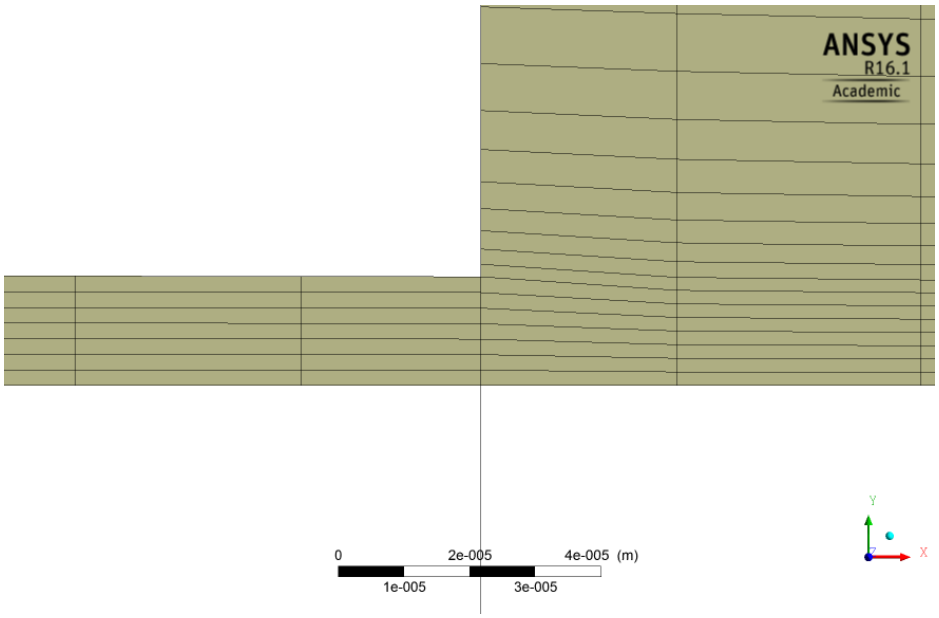


Fig. 5.7 Displaced mesh during a transient timestep

.

It can be observed from the shaft displacement plots that the oscillations along Y are composed of a steady part and a transient part. So, the displacement can be expressed as a function of two separate oscillations, which can be expressed as shown in Eq. 5.6:

$$y = a\cos\omega t + b\sin\omega t + e^{\frac{-t}{\tau}}(c\cos\Omega t + d\sin\Omega t) \tag{5.6}$$

where, ω is the frequency of the steady part (or, the input shaft frequency), Ω is the frequency of oscillations of the transient part, τ is the time period of decay of the transient oscillations, a, b, c and d are the coefficients, and t is the time.

In order to calculate the unknown parameters from Eq. 5.6, it is fitted to the displacement values along Y obtained from the FSI analysis.

Fig. 5.8 shows the fitted curve on the displacement values along Y, when the frequency of force oscillation was 600Hz. Results from the curve-fitting has been shown in Table 5.7.

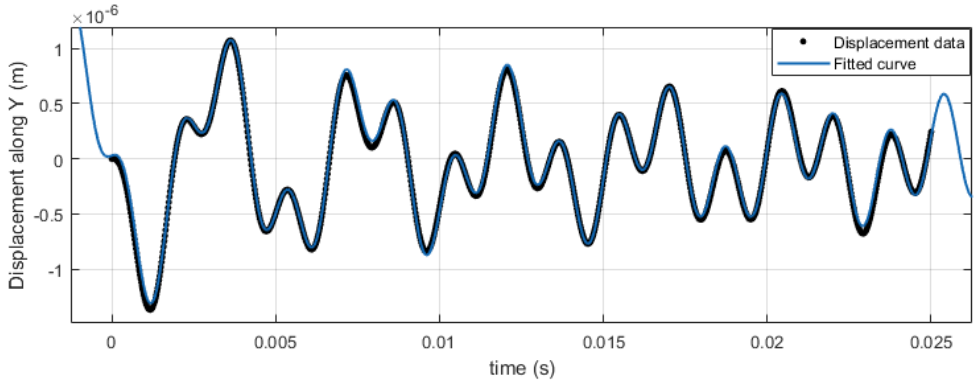


Fig. 5.8 Fitted curve on the plot of the calculated displacement values

.

Table 5.7 Results from the curve-fitting at an excitation frequency of 600Hz

Parameter	Value/Settings
ω (known)	3769 rad/s
Ω	1424 rad/s
τ	0.0152 s
a	3.45×10^{-8}
b	4.03×10^{-7}
c	-6.18×10^{-9}
d	-9.905×10^{-7}

The FSI analysis for the oscillating shaft motion is then carried out for a range of frequencies. Fig. 5.9 - Fig. 5.12 shows some of the curves fitted to the displacement data recorded from the FSI analysis at these frequencies.

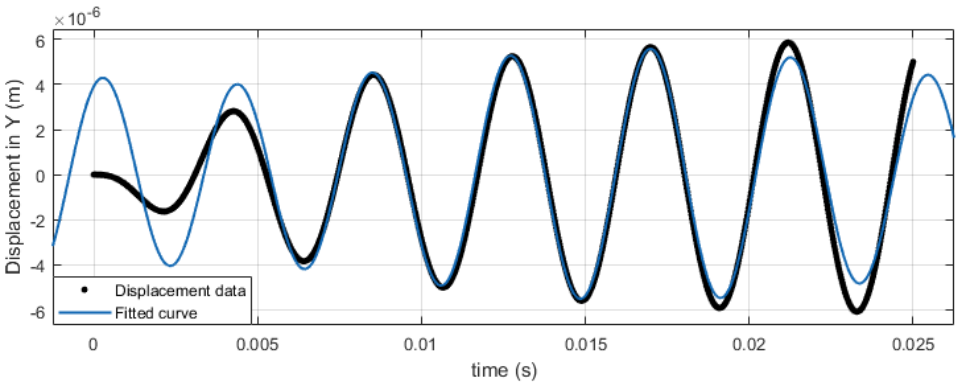


Fig. 5.9 Fitted curve for 200Hz

.

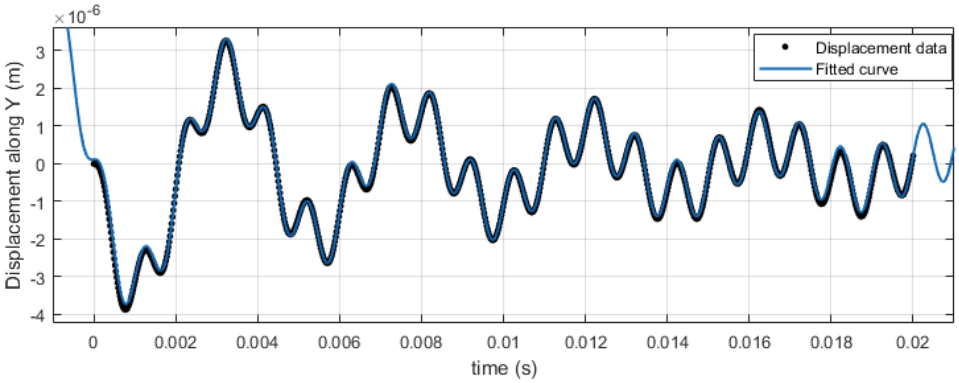


Fig. 5.10 Fitted curve for 1kHz

.

Table 5.7 lists the ω, Ω and τ for all the frequencies for which FSI analysis was carried out.

Average values of angular frequency of transient vibrations and the time constant associated with the transient oscillations are evaluated as:

$$\Omega_{mean} = 1428 \tag{5.7}$$

$$\tau_{mean} = 0.010 \tag{5.8}$$

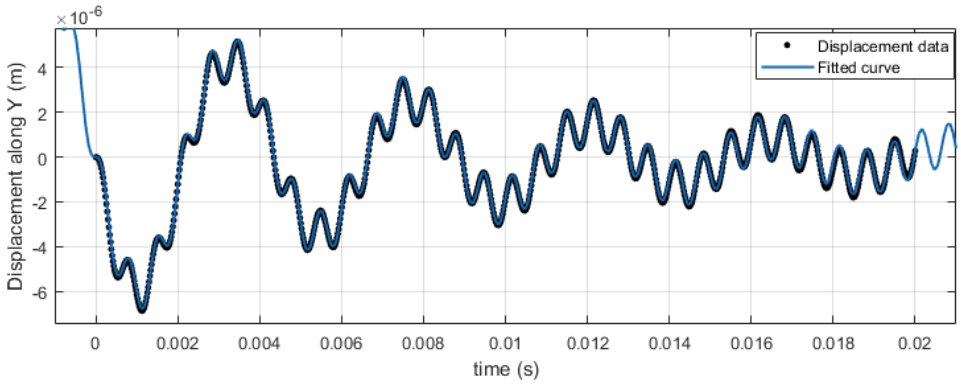


Fig. 5.11 Fitted curve for 1.5kHz

.

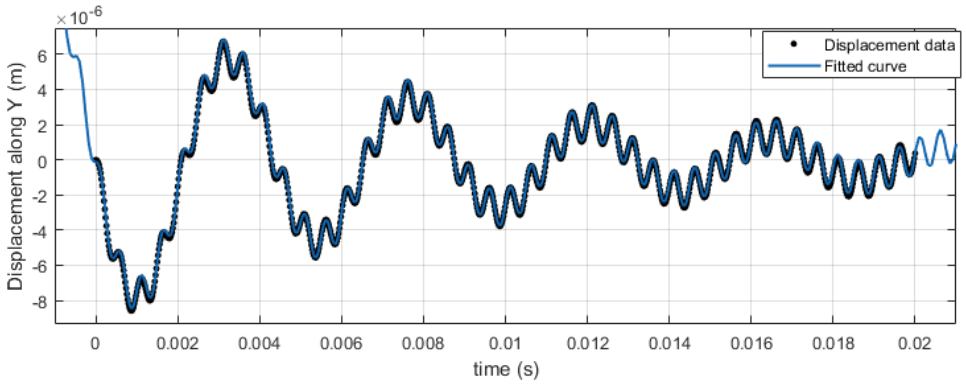


Fig. 5.12 Fitted curve for 2kHz

.

Table 5.8 Results from the curve-fitting of Eq. 5.6 to displacements calculated at a range of excitation frequencies

Frequency (Hz	ω (rad/s)	Ω (rad/s)	τ (s)
200	1256.63	1450	0.0151
400	2513.27	1420	0.0093
600	3769.91	1424	0.0120
1000	6283.18	1430	0.0095
1200	7539.82	1426	0.0086
1500	9424.78	1423	0.0079
2000	12566.37	1425	0.0088

The frequency (ν_{shaft}) corresponding to Ω_{mean} can be written as:

$$\nu_{shaft} = \Omega_{mean}/(2\pi) = 227.27\text{Hz} \tag{5.9}$$

So, it can be concluded that the damped natural frequency of the 1 kg shaft is 227.27 Hz.

5.4.3 Direct Stiffness and Damping Coefficients

The natural frequency of the shaft can be calculated from the equation:

$$\omega_n = \frac{\omega_d}{\sqrt{1-\zeta^2}}, \;\; 1/\tau = \zeta\omega_n \tag{5.10}$$

where, $\omega_d = \Omega_{mean}$

The direct stiffness in Y can then be calculated using the following equation:

$$K_{yy} = m_{shaft}\omega_n^2 \tag{5.11}$$

Moreover, the direct damping in Y can be expressed as:

$$C_{yy} = 2\zeta m_{shaft}\omega_n = 2m_{shaft}/\tau \tag{5.12}$$

Substituting $\nu_{shaft} = 227.27,\ \tau = 0.010,\ m_{shaft} = 1$ in Eq. 5.10 - Eq.5.12, the damping ratio & natural frequency are calculated as shown in Eq. 5.13 and the stiffness & damping coefficients are evaluated as shown in Eq. 5.14

$$\zeta = 0.0699, \;\; \omega_n = 2\pi \times 227.82 \text{ rad/s} \tag{5.13}$$

$$K_{yy} = 2.04 \times 10^6 \text{ N/m}, \;\; C_{yy} = 200 \text{ Ns/m} \tag{5.14}$$

It can be observed that the direct stiffness value of 2.04 MN/m calculated from Study 1 correlates well with the values 1.75 MN/m, 1.85 MN/m and 2.24 MN/m calculated from 1-D, 2-D and steady state CFD analyses respectively.

5.4.4 Study-2: Petal Curve Study

For this study, the shaft was moved in a petal-like shape in the $Y-Z$ plane in the fluid film. In Study-1, the shaft was modelled as a Rigid Body and the movement of the shaft in the fluid film, for different force excitations, was analysed. In Study-2, the shaft is moved in the fluid film and the resultant forces on the fluid film caused by the shaft movement is analysed. A petal motion was selected as it would have a good spatial distribution of points in the fluid film.

Eq. 5.15 is used to define a petal-like path for shaft movement in the fluid film.

$$\begin{aligned} y &= A\cos 2\theta \cos\theta \\ z &= A\cos 2\theta \sin\theta \end{aligned} \tag{5.15}$$

where, A is the amplitude and θ is the radial angle as measured from the initial position. The amplitude A is taken as 5µm and the angle θ is varied from 0 to 2π.

The resultant shaft movement in Y and Z can be visualised from Fig. 5.13 and Fig. 5.14.

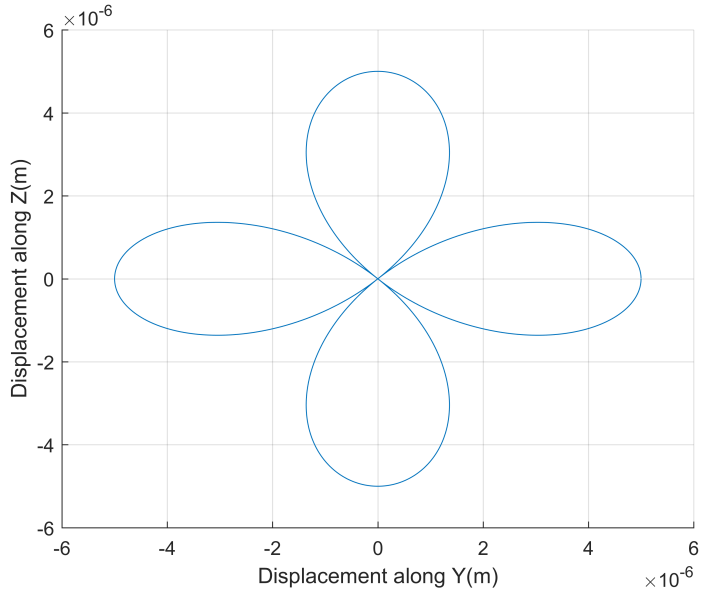


Fig. 5.13 Petal curve traced by the shaft

.

The key input parameters for the FSI analysis are as follows:

- Transient analysis is selected in analysis settings.

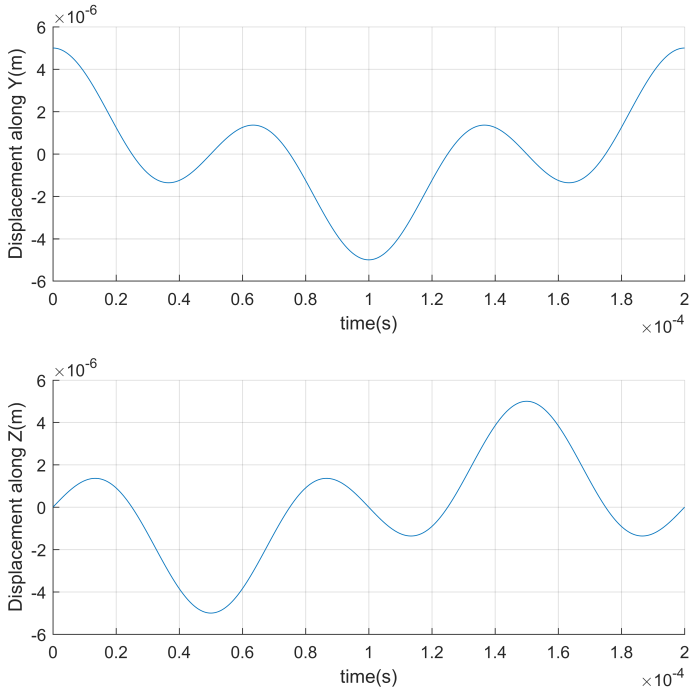


Fig. 5.14 Petal curve - shaft displacement plots along Y and Z

.

- The Inner Wall boundary (as shown in Fig. 5.1) is given a assigned a 'Specified 'Displacement'.
- Mesh motion is defined in terms of 'Displacement Relative to Previous Mesh'.
- In boundary conditions, mesh motion for Inlet and Outlet (Fig. 5.1) is set as 'Unspecified', while it is set as stationary for Outer Wall.

Domain and Solver Settings

The major parameters in domain and solver settings for the FSI simulation are listed in Table.

The monitor points, convergence criteria and rest of the solver settings are same as the ones used in Study-1. Y_{shaft2} and Z_{shaft2} are defined from Eq. 5.15.

Table 5.9 FSI Study2 - Domain and Solver Settings

Parameter	Value/Settings
Specified Displacement - X coordinate	0
Specified Displacement - Y coordinate	Y_{shaft2}
Specified Displacement - Z coordinate	Z_{shaft2}
Timesteps	5×10^{-8}s
Number of timesteps	4000
Maximum number of coefficient loops	20

5.4.5 Study-2: Results

For the first test, the incremental variation in angle θ is chosen such that 2 full petal cycles are completed within the simulation time.

Fig. 5.15 shows the resultant force along Y ($F_{Y\,petal}$) and Z ($F_{Z petal}$) for the shaft displacement governed by the petal equation. Fig. 5.16 shows a plot of $F_{Z petal}$ with respect to $F_{Y\,petal}$.

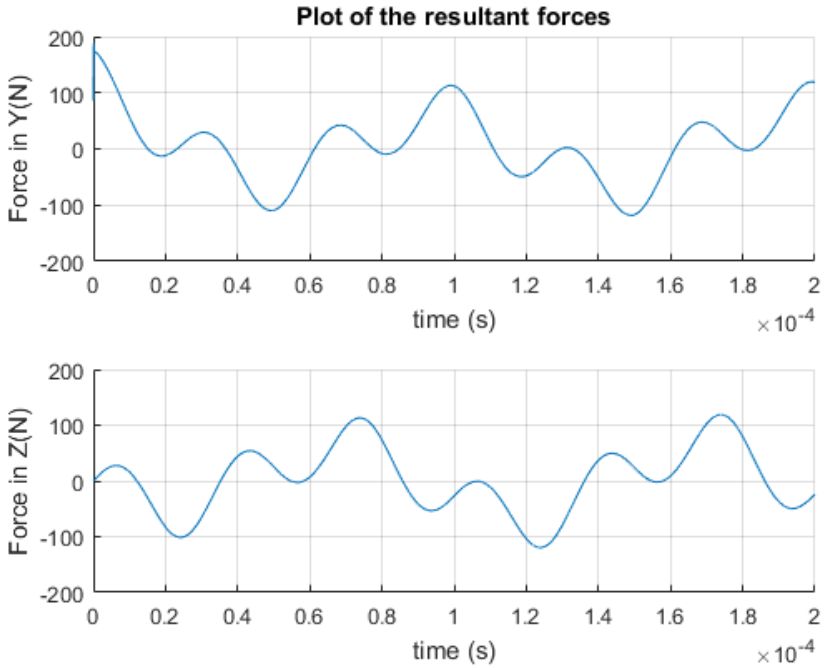


Fig. 5.15 Resultant force along Y and Z for shaft displacements governed by the petal equation (for 2 cycles)

.



Fig. 5.16 Comparison of $F_{Y\,petal}$ and $F_{Z\,petal}$ (for 2 cycles)

.

It is observed that the resultant force curve follows a petal-like pattern as well. The initial deviation of the values of the first petal as compared to the second petal can be attributed to the fact that the initial shaft position is taken as centred, but the petal equation (as shown in Eq. 5.15) is traced from the initial point $(A, 0)$, where A is the maximum value of displacement (which in this case is taken as 5 µm).

The FSI study is repeated for 3 and 4 cycles. In order to avoid the initial deviation observed in the force values, half of the recorded data is sliced off (for e.g., for the 2 cycles study, force data from only 1 petal is considered).

The objective behind this study was to gather a range of data points from the shaft displacement in the fluid film from which the displacement, velocity and force values could be extracted and analysed to evaluate the rotordynamic coefficients of the fluid film.

The stiffness matrix was already evaluated from the steady state analyses discussed in Section 5.3. So, from the equation of motion stated in eq. 5.1 (as demonstrated below), the only unknown variables for any data point in the petal analysis are the the damping coefficients - C_{yy}, C_{zz}, C_{yz} and C_{zy}.

$$\begin{Bmatrix} F_y \\ F_z \end{Bmatrix} = \begin{bmatrix} K_{yy} & K_{yz} \\ K_{zy} & K_{zz} \end{bmatrix} \begin{Bmatrix} y \\ z \end{Bmatrix} + \begin{bmatrix} C_{yy} & C_{yz} \\ C_{zy} & C_{zz} \end{bmatrix} \begin{Bmatrix} \dot{y} \\ \dot{z} \end{Bmatrix}$$

Eq. 5.1 can be expressed in terms of a system of two linear equations as demonstrated below:

$$\begin{bmatrix} -1 & 0 & K_{yy} & K_{yz} & C_{yy} & C_{yz} \\ 0 & -1 & K_{zy} & K_{zz} & C_{zy} & C_{zz} \end{bmatrix} . \begin{bmatrix} F_y & F_z & y & z & \dot{y} & \dot{z} \end{bmatrix}^T = 0 \tag{5.16}$$

It is evident that the system is overdetermined as there are a lot more equations (from the transient data points for the petal curve) than unknowns. So, the Singular Value Decomposition Method is used to find a lower rank matrix which is a good approximation of the data matrix.

The column vector in Eq. 5.16 can be considered as a matrix A. The singular value decomposition of a matrix A is the factorization of A into the product of three matrices $A = USV$, where the columns of U and V are orthonormal and the matrix S is diagonal with positive real entries. The diagonal entries σ_i of S are known as the singular values of A. A common convention is to list the singular values in descending order, which is also incorporated in Matlab.

As there are two degrees of freedom in the petal analysis, a singular value decomposition of A should have two zero singular values. So the values are extracted from the last two columns of U and the linear equations are solved to get the coefficients of the damping matrix.

So the damping matrix evaluated by from the 4-cycle data by SVD method is:

$$C = \begin{bmatrix} 186.98 & -0.96 \\ 1.02 & 188.23 \end{bmatrix} \text{ Ns/m} \tag{5.17}$$

It can be observed that the direct damping value of $\sim$187.6 Ns/m calculated from Study-2 correlates quite well with the value of 200 Ns/m calculated from Study-1, as evaluated in Eq. 5.14

The solution is verified by putting the values of stiffness and damping coefficients in Eq. 5.16 and re-evaluating the force for the 3 cycles. The re-evaluated forces ($F_{RY\,petal}$ and $F_{RZpetal}$) is then compared against the actual forces $F_{Y\,petal}$ and F_{Zpetal}., as shown in Fig. 5.17 - Fig. 5.19.

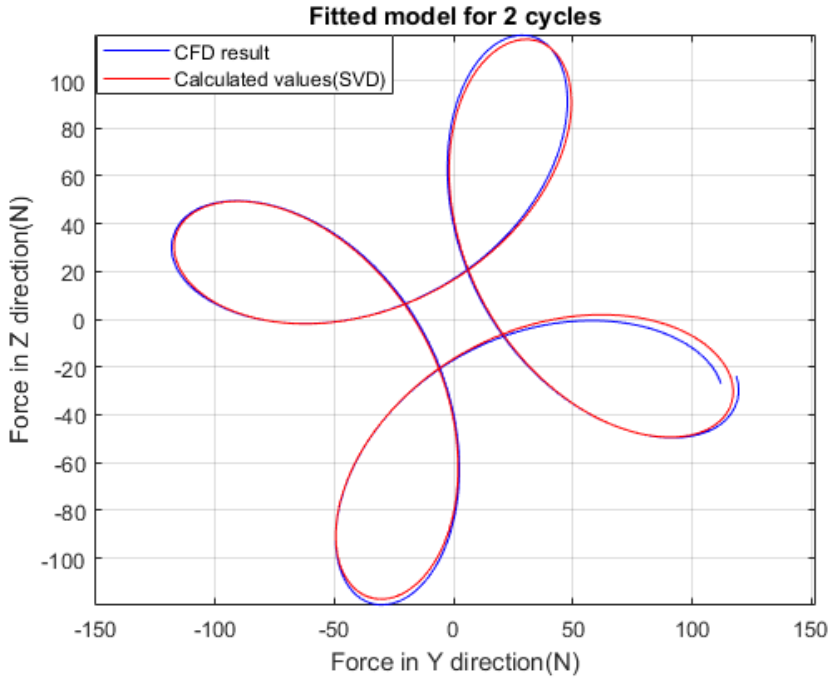


Fig. 5.17 Comparison between the actual force values and the fitted model (for 2 cycles)

.

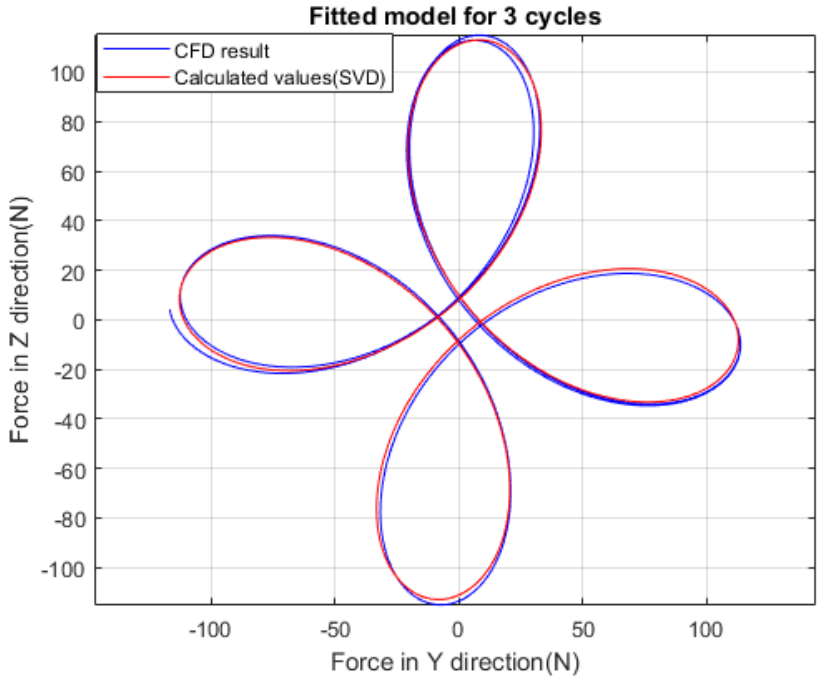


Fig. 5.18 Comparison between the actual force values and the fitted model (for 3 cycles)

.

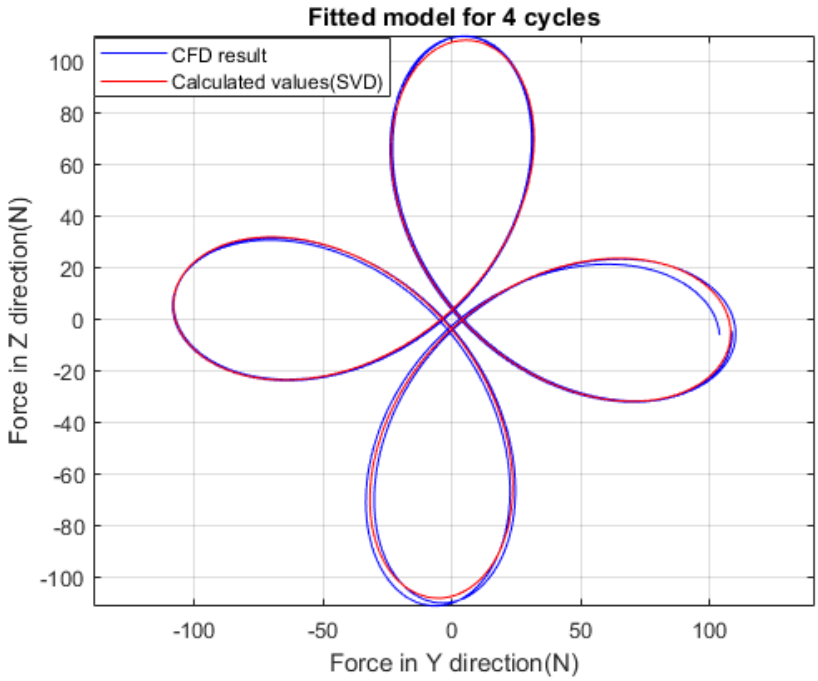


Fig. 5.19 Comparison between the actual force values and the fitted model (for 4 cycles)

.

To validate the values obtained from the SVD analysis in Study 2, a circular path is selected for the motion of the shaft, and the damping and stiffness coefficients are substituted in Eq. 5.16 and compared with the force data obtained from the FSI analysis in CFD.

Eq. 5.18 is used to define a circular path for shaft movement in the fluid film.

$$\begin{aligned} y &= A\sin\theta \\ z &= A\cos\theta \end{aligned} \tag{5.18}$$

where, A is the amplitude and θ is the radial angle as measured from the initial position. The amplitude A is taken as 5μm and the angle θ is varied from 0 to 2π.

The re-evaluated forces are then compared against the actual forces , as shown in Fig. 5.20

From Fig. 5.20 it is observed that there is the good correlation between the fitted model (from the coefficient values calculated in Petal curve study) and the actual force data extracted from the CFD analysis of the circular path motion.

The direct damping coefficient of 186.98 obtained in Eq. 5.17

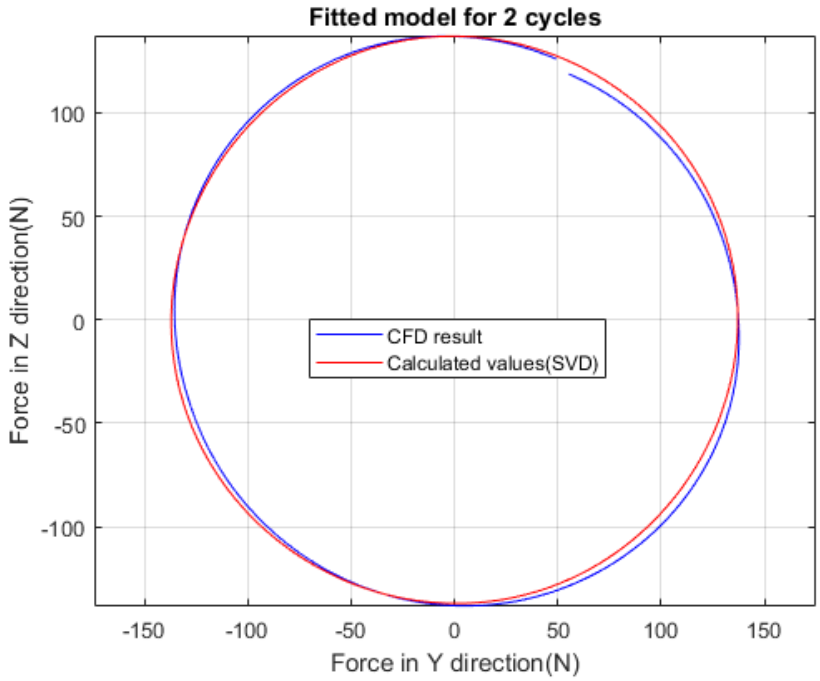


Fig. 5.20 Comparison between the actual force values and the fitted model (for 2 cycles)

.

5.4.6 Dynamic Coefficients of the fluid film - 2

As the stiffness and damping matrices have now been evaluated, the dynamic stiffness coefficient, as discussed in 3.3.4 in Chapter 3, can now be calculated. Using the damping and stiffness coefficient values, from Eq. 5.3 and Eq. 5.17 respectively, in Eq. 3.35 we have:

$$\kappa_{eq} = 2.25 \times 10^6 \text{ N/m} \tag{5.19}$$

5.5 Comparison between 1-D, 2-D and CFD analyses

1-D, 2-D and CFD analyses were carried out for for a range of pressure ratios, seal outlet height, and shaft rotation speeds. Direct stiffness values were calculated for each of these cases.

Fig. 5.21, shows the variation of direct film stiffness for increasing seal outlet height when the inlet pressure is 4 bar. It can be observed that although the direct stiffness values follow a similar trend for all the 3 analyses, calculated stiffness values from CFD are generally higher than those evaluated from 1-D and 2-D analyses. This may be attributed to the fact

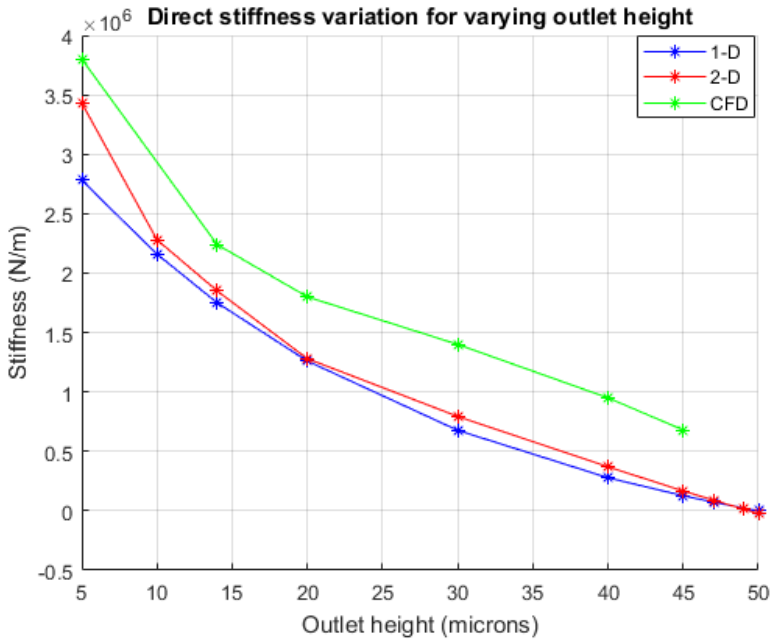


Fig. 5.21 Comparison between stiffness values from 1-D, 2-D and CFD analyses for varying seal outlet height, for a pressure ratio of 4, shaft rotation speed of 10000 rpm and a fixed seal inlet height of 50 µm

.

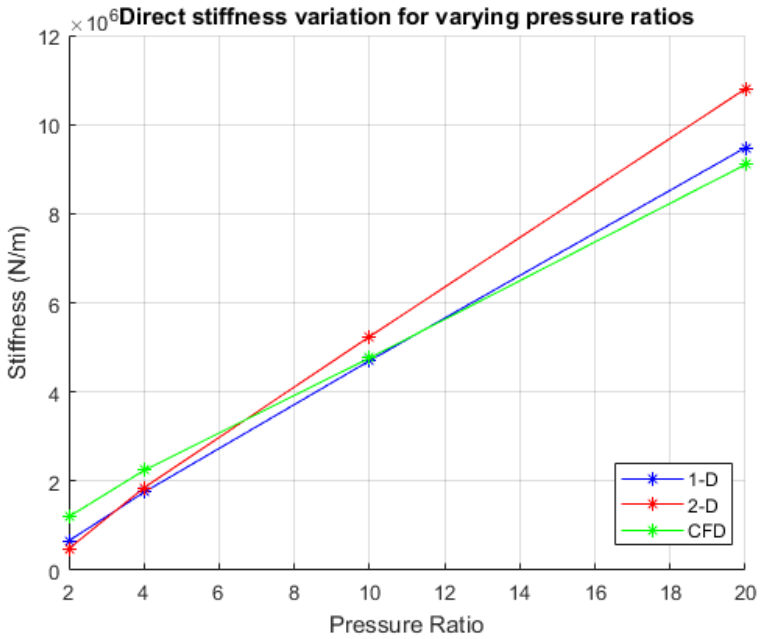


Fig. 5.22 Comparison between stiffness values from 1-D, 2-D and CFD analyses for varying pressure ratio, for a fixed shaft rotation speed of 10000 rpm and a seal inlet and outlet height of 50 µm and 14 µm respectively

.

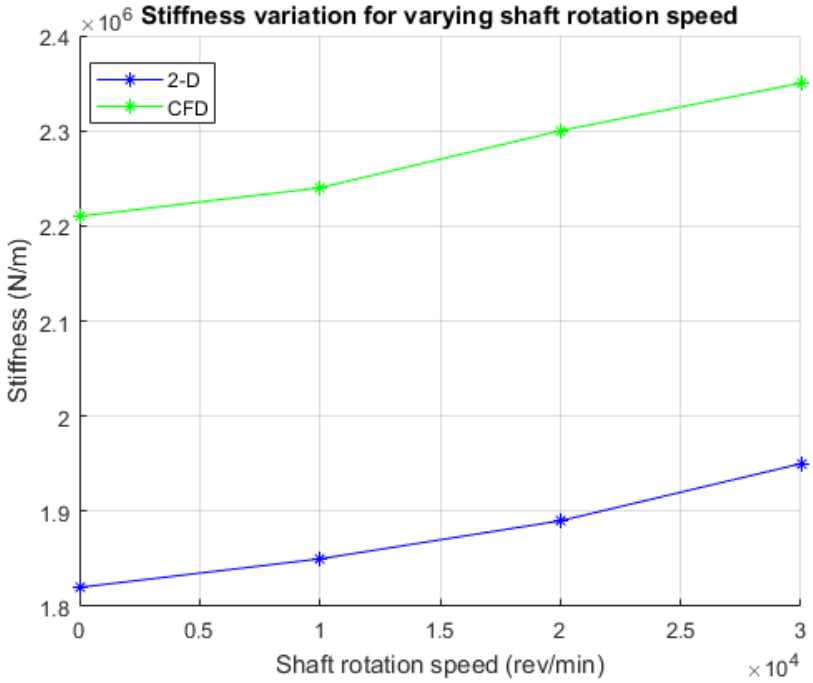


Fig. 5.23 Comparison between stiffness values from 1-D, 2-D and CFD analyses for varying shaft rotation speeds at 4 bar, for a seal inlet and outlet height of 50 µm and 14 µm respectively

.

that the full Navier-Stokes equations are solved in the CFD code and it also accounts for turbulence effects. It is also observed that the difference between CFD and 1-D or 2-D analyses increases with increasing seal outlet height. One of the possible explanations for this observation could be that as the characteristic length increases with increasing seal outlet height, the Reynold's number increases and the turbulence effects become more significant.

Fig. 5.22 shows the comparison of film stiffness for varying pressure ratios, calculated from 1-D, 2-D and CFD analyses. It can be observed that stiffness increases linearly with pressure ratio and the values are comparable for all the 3 analyses.

Fig. 5.23 shows the variation of film stiffness with increasing shaft rotation speed for 2-D and CFD analyses. It is observed that there is minor increase in stiffness with increasing shaft rotation speed and although stiffness values obtained from CFD are slightly higher (which may again be attributed to turbulence effects and flow irregularities), they follow very similar trend for any variation in shaft rotation speed.

5.6 Summary and Discussion

In this chapter, steady state and transient CFD simulations were carried out to analyse the properties of the fluid film. The applied boundary conditions, the fluid domain settings and solver settings in selected for steady state and transient simulations were discussed in detail.

The results from the steady state simulation was compared to the 1-D and 2-D results and a good correlation was found between the 2-D and CFD results. Stiffness matrix was evaluated by comparing lift forces generated in different shaft positions (in steady state). It was observed that the direct stiffness value calculated, 2.24 MN/m, was a bit higher than those calculated from 1-D and 2-D analysis, 1.75 MN/m and 1.85 MN/m respectively.

Fluid Structure Interaction analyses were carried out to analyse the transient behaviour of the air film for shaft perturbations. For the first study, an oscillating force was applied to shaft and the shaft displacement in (Y,Z) was recorded (considering that the seal ring was fixed). The study was repeated for a range of shaft oscillation frequencies. It was observed that the shaft displacement was composed of a steady parts and a transient part. On fitting the displacement to an equation simulating this steady and transient behaviour for all shaft frequencies, resonance frequency of the 1 kg shaft was found to be 227.27 Hz.

For the second FSI study, the shaft was moved through the seal air-film in a petal-like path in $Y-Z$ plane and the resultant forces on the fluid film were recorded. The study was repeated for different petal cycles. As the force, displacement, velocity and stiffness coefficients were known for all data points, the damping coefficients were evaluated using 5.16, after the model was reduced using the Singular Value Decomposition technique. As all the rotordynamic coefficients were known, the force values were re-evaluated using Eq. 5.1 and the plots from the original force values and the re-evaluated force values were compared for the petal curve and the circular curve. It was observed that the data evaluated from the rotordynamic coefficient had a good agreement with the actual force values.

The direct stiffness values were evaluated for a range of pressure ratios, seal outlet height and shaft rotation speeds from 1-D, 2-D and CFD analyses and the 3 analyses methods were compared with each other. The stiffness values obtained from the 3 analyses methods seem to have good correlation with each other for all operating conditions studied.

Chapter 3 to Chapter 5 have been dedicated towards detailing the modelling and simulations carried out for characterising the properties of the fluid film - its rotordynamic coefficients, leakage rate, transient behaviour etc. An important consideration in designing a full-ring radial-gap air-riding seal would be to analyse the stability of the seal and understand

the critical design considerations for designing this novel kind of seal. Chapter 6 is dedicated towards understanding the stability and behaviour of the seal for expected operating conditions. Chapter 6 also highlights the design considerations and discusses the results from some rudimentary testing carried out on the seal.

Chapter 6

Seal Design and Experimental Results

Chapter 3 to Chapter 5 have been dedicated towards developing the modelling capability to predict the performance of the full-ring radial-gap air-riding seal and evaluating the rotordynamic coefficients of the seal, thus successfully fulfilling the first and a part of the second objective, as described in Chapter 1).

This chapter analyses the stability of the seal during its operating conditions and discusses some results from the rudimentary testing of this new sealing system. Some of the key design considerations are outlined and a detailed set-up of the designed seal system and the test rig is provided.

6.1 Routh-Hurwitz Stability Analysis

With the knowledge of the rotordynamic coefficients of the seal, it was possible to carry out an analysis to investigate the stability of the system. Routh-Hurwitz stability criterion provides a way to determine if the equations of motion of a linear system have only stable solutions, without having to solve the characteristic equation directly.

In 1875, Edward Routh developed an algorithm to predict the number of roots of a characteristic polynomial that lie on the right hand side of the complex plane. In 1895, Adolf Hurwitz proposed a methodology where he arranged the coefficients of the polynomial into a square matrix and showed that the polynomial is stable if and only if the sequence of determinants of its principal submatrices are all positive. So a stability criterion developed from combining their findings stated the necessary and sufficient condition for all roots of

a characteristic polynomial to lie on the left half of the complex plane, which is known as Routh-Hurwitz stability criterion.

To demonstrate the Routh-Hurwitz criterion, let a characteristic polynomial be expressed as:

$$a_0 s^n + a_1 s^{n-1} + a_2 s^{n-2} + \ldots a_{n-1} s + a_n = 0 \tag{6.1}$$

The coefficients of the polynomial are then arranged as shown below:

$$\begin{array}{cccccc} s^n & a_0 & a_2 & a_4 & a_6 \ldots \\ s^{n-1} & a_1 & a_3 & a_5 & a_7 \ldots \\ s^{n-2} & b_1 & b_2 & b_3 & b_4 \ldots \\ s^{n-3} & c_1 & c_2 & c_3 & c_4 \ldots \\ \vdots & \vdots & \vdots & & \\ s^1 & f_1 & & & \\ s^0 & g_0 & & & \end{array} \tag{6.2}$$

where,

$$b_1 = \frac{a_1 a_2 - a_0 a_3}{a_1}$$
$$b_2 = \frac{a_1 a_4 - a_0 a_5}{a_1}$$
$$\vdots$$
$$c_1 = \frac{b_1 a_3 - b_1 a_2}{b_1}$$
$$c_2 = \frac{b_1 a_5 - b_1 a_3}{a_1}$$
$$\vdots$$

until the n_{th} row of the array has been completed. The column beginning with a_0 is considered to be the first column of the array. From Routh-Hurwitz stability criterion, it can be stated that for the system to be stable all roots should have negative real parts, i.e. the number of sign changes in the first column of the table should be 0.

This exercise will assume a single degree of freedom model (SDOF) where the shaft is oscillating and the seal ring is kept fixed. The seal system can be represented by a mass-spring-damper system, where its motion can be described by the equation:

$$\begin{bmatrix} m & 0 \\ 0 & m \end{bmatrix} \begin{Bmatrix} \ddot{y} \\ \ddot{z} \end{Bmatrix} + \begin{bmatrix} C_{yy} & C_{yz} \\ C_{zy} & C_{zz} \end{bmatrix} \begin{Bmatrix} \dot{y} \\ \dot{z} \end{Bmatrix} + \begin{bmatrix} K_{yy} & K_{yz} \\ K_{zy} & K_{zz} \end{bmatrix} \begin{Bmatrix} y \\ z \end{Bmatrix} = 0 \tag{6.3}$$

Eigen values of this equation are roots of the expression:

$$\begin{vmatrix} ms^2 + C_{yy}s + K_{yy} & C_{yz}s + K_{yz} \\ C_{zy}s + K_{zy} & ms^2 + C_{zz}s + K_{zz} \end{vmatrix} = 0 \tag{6.4}$$

From the stiffness and damping matrices computed in Eq.5.3 and 5.17, it is possible to conclude (within logical limits of approximation) that $K_{yy} = K_{zz}$, $K_{yz} = -K_{zy}$ and $C_{yy} = C_{zz}$, $C_{yz} = -C_{zy}$.

So, Eq. 6.4 can be expressed as:

$$m^2s^4 + C_{yy}^2s^2 + K_{yy}^2 + 2mC_{yy}s^3 + 2C_{yy}K_{yy}s + 2mK_{yy}s^2 + C_{yz}^2s^2 + K_{yz}^2 + 2C_{yz}K_{yz}s = 0 \tag{6.5}$$

Using the values of the rotordynamic coefficients (from Eq. 5.3 and Eq. 5.17) and considering the mass of the shaft as 1 kg, Eq. 6.5 can be written as:

$$\begin{aligned} 1s^4 + 3.49 \times 10^4 s^2 + 5.01 \times 10^{12} + 373.96s^3 + 8.37 \times 10^8 s + \\ 4.48 \times 10^6 s^2 + 0.92s^2 + 1.46 \times 10^{10} + 2.32 \times 10^5 s = 0 \end{aligned} \tag{6.6}$$

The Routh array is evaluated as:

Table 6.1 Routh Hurwitz analysis of the seal system

s^4	1	4.5199×10^6	5.0246×10^{12}
s^3	373.96	8.3723×10^8	0
s^2	2.2761×10^6	5.0246×10^{12}	0
s^1	1.1688×10^7	0	0
s^0	5.0246×10^{12}	0	0

As number of sign changes in the first column is 0, it can be concluded that the system is stable.

6.2 Whirl Frequency Ratio

Following the calculation of equivalent dynamic stiffness in Eq.5.19, Lund's equations [38] can be used to calculate the critical mass and the whirl frequency ratio. Using Eq. 3.34 (as discussed in Section 3.3.4), for a shaft rotation speed of 10000 rpm, critical mass of the system is evaluated as:

$$M_c = 81 \text{ kg} \tag{6.7}$$

Using the stiffness and damping coefficients (as evaluated in Eq. 5.3 and Eq. 5.17), the whirl frequency ratio (WFR) can be then calculated using the following equation (as shown by Lund [38]):

$$WFR^2 = (\frac{\bar{\omega}}{\Omega})^2 = \frac{(\kappa_{eq} - K_{yy})(\kappa_{eq} - K_{zz}) - K_{yz}K_{zy}}{C_{yy}C_{zz} - C_{yz}C_{zy}} \tag{6.8}$$

$$WFR = 543.77 \tag{6.9}$$

Hence, it can be concluded that for a shaft rotation speed of 10000 rpm, the system becomes unstable if the system mass exceeds the critical mass value of 81 kg. As the mass of the seal ring system is $<<$ 81 kg, it can be concluded that the seal ring system is stable for a shaft rotation speed of 10000 rpm. If the actual system mass is greater than M_c, the system will begin self-excited motions at a frequency equalling 543.77 times the shaft rotational frequency.

6.3 Practical Operability Criteria for Dynamic Operation

One of the most important considerations in the design of the full-ring radial-gap air-riding seal is to ensure that there is no contact between the rotor(shaft) and stator(seal ring) during the dynamic running conditions of an engine. The study presented in this section aims to investigate the response of the seal for shaft-runouts and unbalance vibrations.

The seal-shaft system can be represented as shown in Fig. 6.1.

where, $k_{air-film}$ is the stiffness of the air-film. Let $u(t)$ be the shaft displacement for a once-per-revolution vibration. The seal displacement resulting from the shaft excitation is denoted here by $q(t)$.

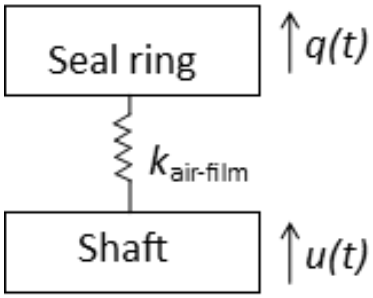


Fig. 6.1 Schematic of the seal-shaft system

.

Let u_{max} be the maximum shaft displacement and let the minimum seal height be denoted by h_{min} (h_{min} = 14µm). As long as $u_{max} < h_{min}$, there would not be any possibility of a rotor-stator contact. If $u_{max} > h_{min}$, the seal response needs to be investigated to determine the limiting conditions to ensure that there is no contact between the seal ring and the shaft.

Two important criteria were identified for ensuring operability of the seal for dynamic running conditions:

1. Frequency criterion
2. Relative movement criterion

Frequency criterion states that the natural frequency of the seal on the air film should be much greater than the maximum excitation frequency of the shaft, i.e. $\omega_{seal} >> \Omega_{max_shaft}$.

From the vibration study carried out in Section 5.4.1, the shaft resonance frequency was determined as 354.9 Hz (for 1 kg shaft). In Study-1 described in Section 5.4.1, the seal ring was kept constant and the movement of the shaft in the fluid film in response to the excitation frequency vibrations was recorded. Now, if the shaft is assumed to be fixed and the movement of seal ring in response to the excitation is measured, the force exerted by the air film on the seal (in this case) will be the same as that exerted on the shaft in Study-1 (as the properties of the air film remain unchanged). The weight of the seal ring is 0.159 kg. So the natural frequency of the seal can be calculated as:

$$\omega_{seal} = \sqrt{\frac{\Omega_{shaft}^2 . m_{shaft}}{m_{seal}}} \tag{6.10}$$

where, ω_{seal} is the natural frequency of the seal, Ω_{shaft} is the resonance frequency of the shaft for the vibration study and m_{shaft} and m_{seal} are the mass of shaft and the seal ring, respectively.

So the natural frequency of the seal was calculated as:

$$\omega_{seal} = 569.96 \text{ Hz} \tag{6.11}$$

For a shaft with a maximum rotation speed of 20,000 rpm, maximum shaft frequency (unbalance vibrations) can be calculated as:

$$\Omega_{max_shaft} = 20000/60 = 333.33 \text{ Hz} \tag{6.12}$$

As $\omega_{seal} > \Omega_{max_shaft}$, it can be concluded that the seal satisfies the frequency criterion of operability during dynamic operation.

The relative movement criterion states that for a shaft excitation $u(t)$, the relative displacement of the shaft and the seal ring should be less than the minimum seal height. It can be expressed as:

$$q(t) - u(t) < h_{min} \tag{6.13}$$

Let the shaft excitation be caused due to the unbalance vibrations arising from the maximum shaft speed of 20,000 rpm. So the excitation frequency is Ω_{max_shaft}. The compression in spring (air-film) computed with respect to the shaft and seal displacement should be equal. This can be expressed as:

$$\begin{aligned} u.k_{air-film} &= (k_{air-film} - \Omega^2_{max_shaft}.m_{seal})q \\ i.e. \quad q &= \frac{u.k_{air-film}}{(k_{air-film} - \Omega^2_{max_shaft}.m_{seal})} \end{aligned} \tag{6.14}$$

where, u and q are the shaft and seal displacements, respectively.

So, the relative displacements can be calculated as:

$$q - u = u.\Big[\frac{k_{air-film}}{(k_{air-film} - \Omega^2_{max_shaft}.m_{seal})} - 1\Big] \tag{6.15}$$

Amplitudes of the unbalance vibrations in gas turbine engines can reach up to 1mm. So, on substituting the values of $k_{air-film}$, m_{seal} and Ω_{max_shaft} in Eq. 6.15 and considering $u = 1 \times 10^{-3}$m:

So, the relative displacements can be calculated as:

$$q - u = 7.9 \times 10^{-6}\text{m} \tag{6.16}$$

It is observed that the relative displacement is almost half of the minimum seal height. So it can be concluded that the seal can be successfully employed for conditions where the shaft rotation speed is 20,000 rpm and there is a shaft run-out of 1 mm. In its current configuration, the seal won't be suitable to employ in locations where the expected shaft run-out is more than 2.4 mm or for shaft rotation speeds of more than 20000.

Thermal Considerations

Another important criterion for avoiding rotor-stator contact is to ensure that the thermal expansion of the rotor is always less than that of the stator.

Structural steel is used as a material for manufacturing the shaft. The coefficient of thermal expansion of structural steel as described in [88] can be expressed as, α_{steel} = 12 $\times 10^{-6}$ K^{-1}.

To ensure that the thermal expansion of the stator is always more than the rotor, the seal ring should be made out of a material with a higher coefficient of thermal expansion than steel, but it is also important to ensure that the relative thermal expansion of the stator to rotor is not very high to keep the leakage rate within the desired limits and maintain the minimum film stiffness required. Brass was selected as the material for the seal ring because it matched well with this criterion. The coefficient of thermal expansion of brass, $\alpha_{brass} = 19 \times 10^{-6}\text{K}^{-1}$. It was also one of the recommended target materials listed for the selected proximity sensors.

6.4 Seal System Design

Modelling and performance analysis of the full-ring radial-gap air-riding seal has been discussed in Chapter 3 to Chapter 6, and the stability analysis of the seal system was discussed in this chapter (Section 6.1). Based on these studies, it was concluded that the modelled seal system was able to satisfy the desired design requirements of the seal.

The final step of this research on full-ring radial-gap air-riding seal was to design the full seal system and carry out some rudimentary testing of the seal system. This section

provides a detailed description of the seal system and the test rig design. After designing the full system, it was manufactured from one of the suppliers of The University of Nottingham.

The modelled seal ring is shown in Fig. 6.2 and Fig. 6.3. Seal ring material and thickness was chosen so that they satisfy the thermal considerations discussed above and they satisfy the advised material thickness for the sensors. The seal material selection and thickness have not been optimised. This can be explored further in future research work. Due to the small sealing gap and tight clearances needed on the seal surface, high finishing will be needed on the seal ID which will increase the manufacturing cost. This is again subjected to further research work and exploration.

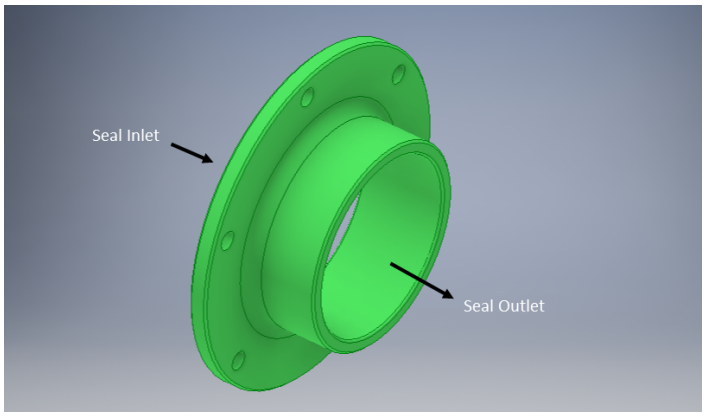


Fig. 6.2 Seal ring design

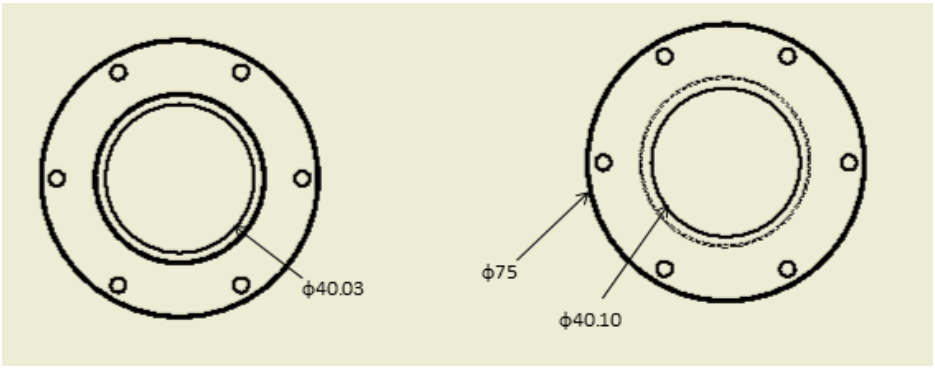


Fig. 6.3 Seal ring design - front and back view

.

For the supporting assembly or the secondary seal, the two important design criteria were:

1. It should be quite flexible for all radial movements, or in other words, its radial stiffness should be less than the stiffness of the air-film so that the air-film is able to drive or move the seal system for any shaft perturbations.

2. As it would also act as a secondary seal, it should be able to withstand the high pressure air flowing through it.

A formed metal bellow was chosen as the core element of the secondary seal, as it satisfied both these conditions. This item was taken off-the-shelf from Hyspan Bellows (model no. -7523L). The details of the chosen bellow is shown below [89] in Fig. 6.4:

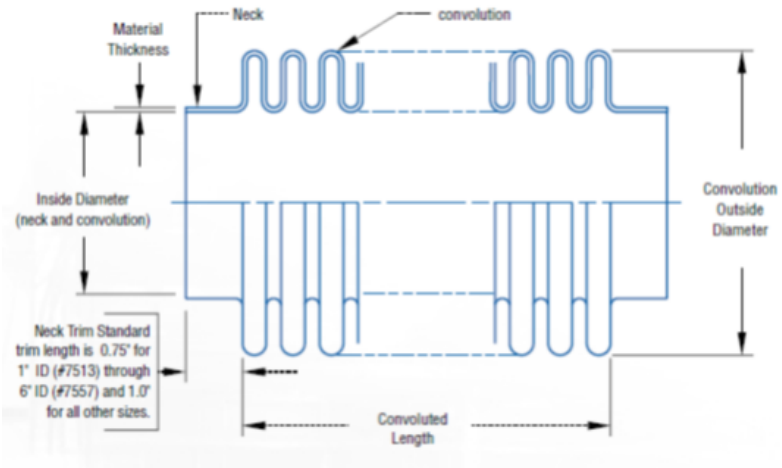


Fig. 6.4 Schematic of the bellows [89]

.

Table 6.2 Details of the bellows model chosen (Hyspan Formed Bellows 7523L)

Material	I.D(mm)	O.D (mm)	Max. pressure (bar)	k_{rad} (N/m)	k_{ax}(N/m)
Beryllium copper	41.3	54.1	16.75	1.5×10^3	2.9×10^5

where, $I.D$ & $O.D$ are the inside and outside diameter, respectively, and k_{rad} & k_{ax} are the radial and axial stiffness of the bellow, respectively.

One of the demerits of using the flexible bellow was that it susceptible to an angular mode of deformation (rotation of the longitudinal centre-line about the perpendicular axis) [89]. That was an undesirable characteristic as it would tilt the seal ring outlet face towards or away the shaft, thereby changing the seal height along the axial direction. So the bellows were reinforced with flexures and a face plates, as shown in Fig. 6.5

The H.P inlet end is screwed to the end plate (discussed in Section 5.4), so an O-ring seal is provided to avoid any air leakage from the sides.

The full seal system design is shown in Fig. 6.6. Air at high pressure (from the compressor) enters the $H.P\ chamber$ through the $H.P\ Inlet$. There is a vertical end-plate between the $H.P\ chamber$ and the secondary seal but it has not be shown here. The $H.P\ chamber$ is

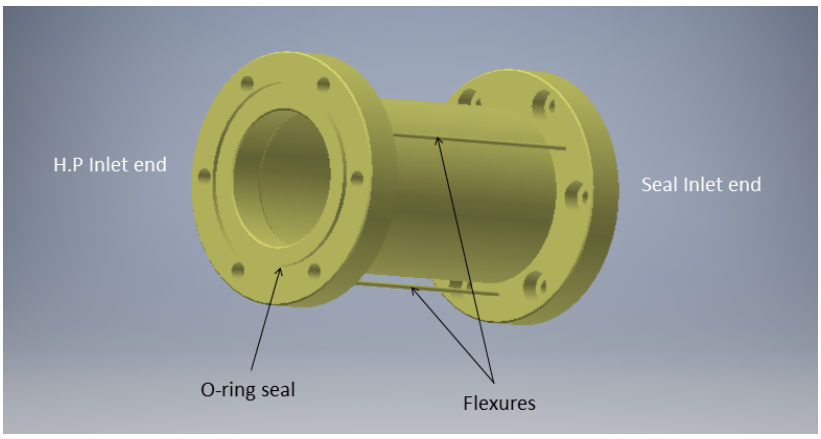


Fig. 6.5 Secondary seal- bellows and flexure arrangement

.

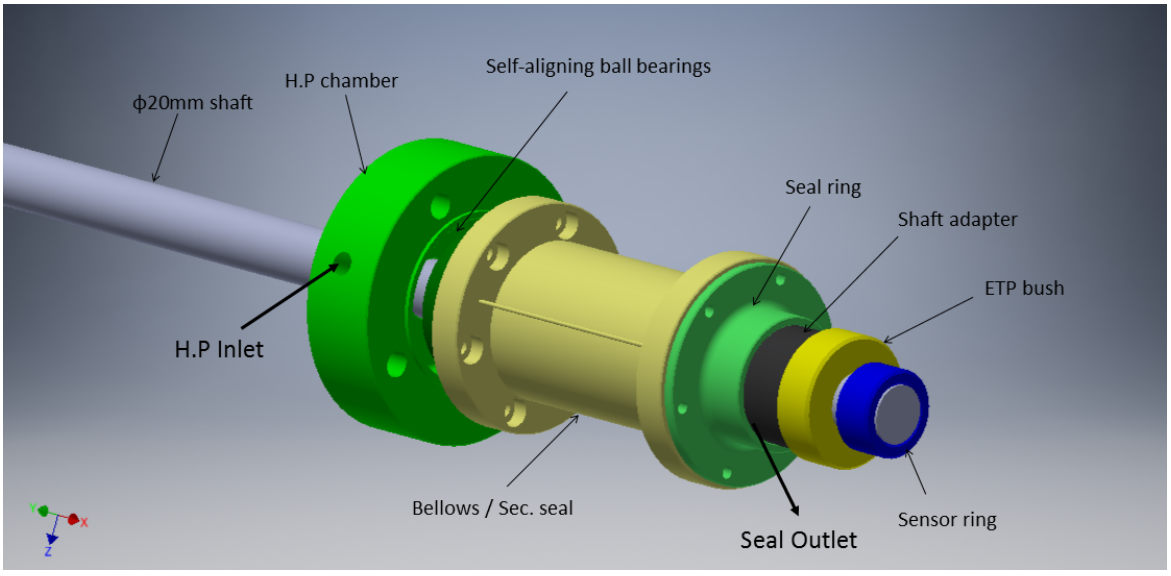


Fig. 6.6 Seal system assembly (model)

screwed to the end plate. The $O-ring\ seal$ at the mating surface of the $H.P\ chamber$ (with the end plate) avoids any side air leakage.

A self-aligning *ball bearing* is fitted at the cavity through the end plate. From the $H.P\ chamber$, high pressure air flows axially through the bearing and enters the *secondary seal*. The inlet end of the *secondary seal* is screwed to the end plate, as described earlier. From the bellows, high pressure air flows axially to the *seal ring* fitted to the *secondary seal* and exits from the $seal\ outlet$.

As the shaft (present in the intended rig) is of 20 mm diameter, a $\phi 20mm - \phi 40mm$ shaft adapter is mounted on which the *seal ring* would be floating. The adapter is kept fixed on a shaft position by using an *ETP Bush*. A *sensor ring* made of aluminium is provided at the end of shaft to act as a target for the sensors.

An *Outlet chamber* made of plexiglass was designed to simulate the real scenario of the seal operation, as shown in Fig. 6.7. It had provisions for inserting the sensors and the solenoid actuator (discussed later in this chapter).

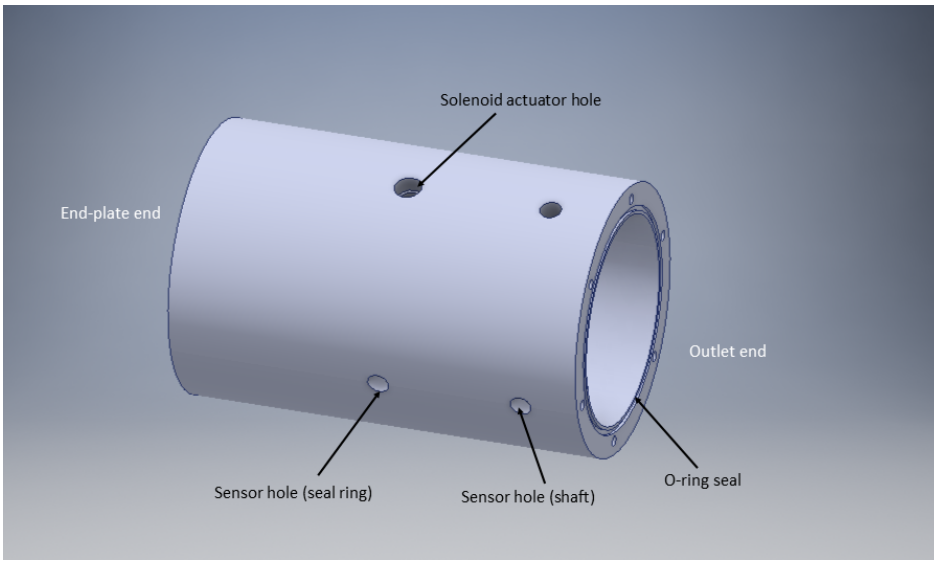


Fig. 6.7 Outlet chamber

This completed the modelling of the full seal system. The actual seal assembly has been shown in Fig. 6.8.

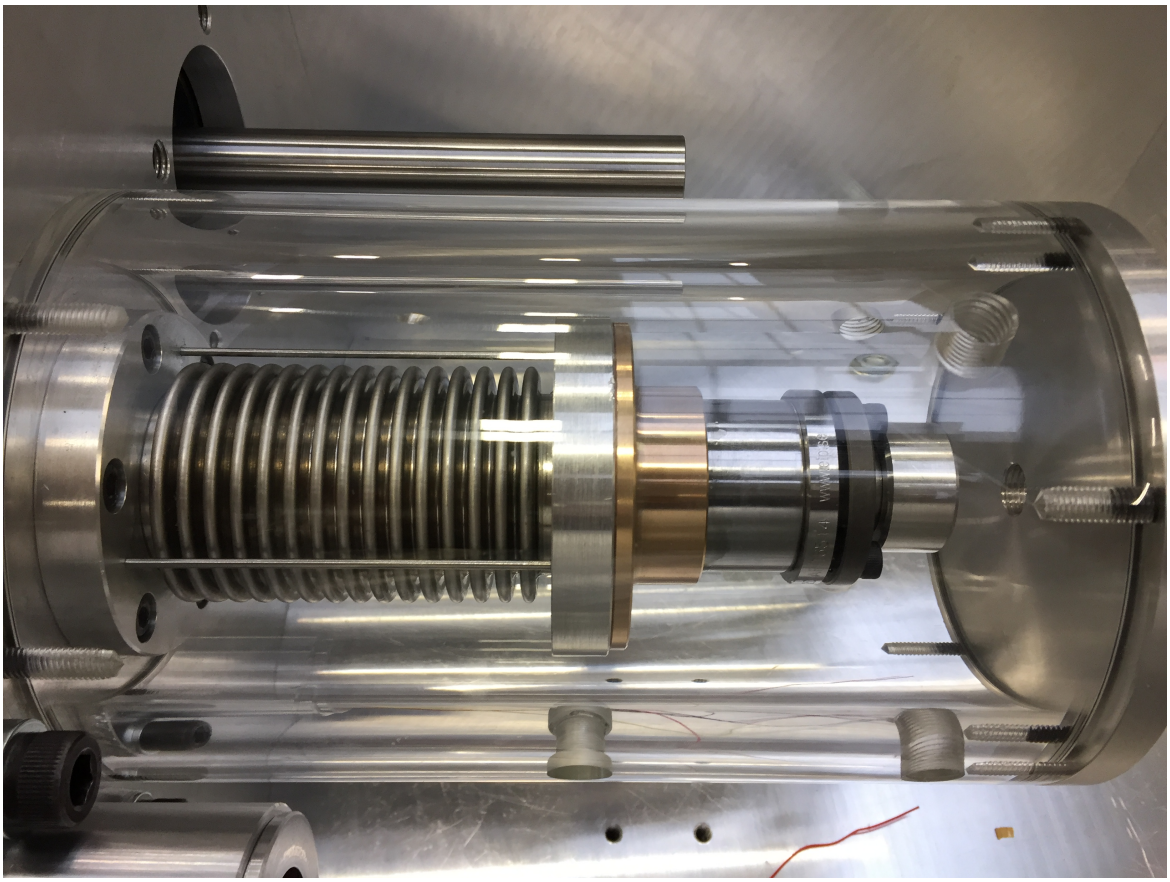


Fig. 6.8 Seal Assembly

6.5 Integrated Test-Rig

The seal system described in Section 6.4 was designed to be integrated into an integrated test-rig which would combine three different technologies developed by three researchers: an air-riding seal system developed by the author of this thesis, a bearingless machine developed by Nicolas Schneider [90] and a technology developed by Constanza Ahumada [90] which investigated a methodology of moderating the electrical loading caused by a generator to reduce shaft vibrations. A further discussion on the latter two topics is outside the scope of this thesis as they are individual research work carried out by the above mentioned researchers.

The model and actual assembly of the test rig have been shown in Fig. 6.9 and Fig. 6.10. The bearingless machine, with a maximum rotation speed of 3,000 rpm, acts as the prime mover. The shaft on which the seal is mounted(seal shaft) is connected to the power shaft

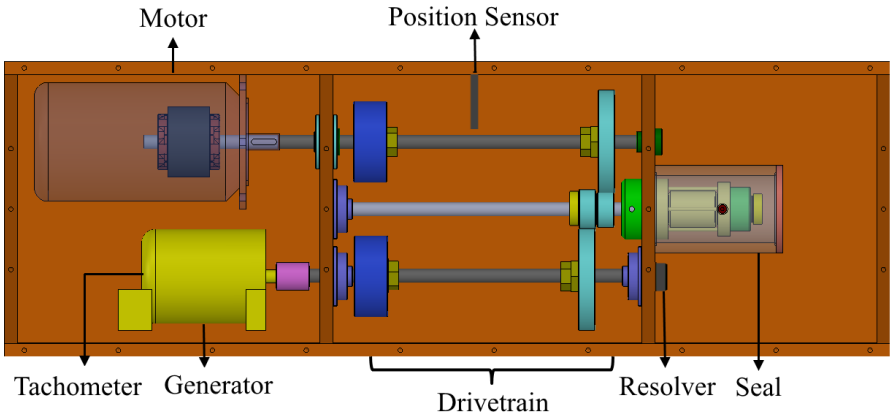


Fig. 6.9 Test-rig model

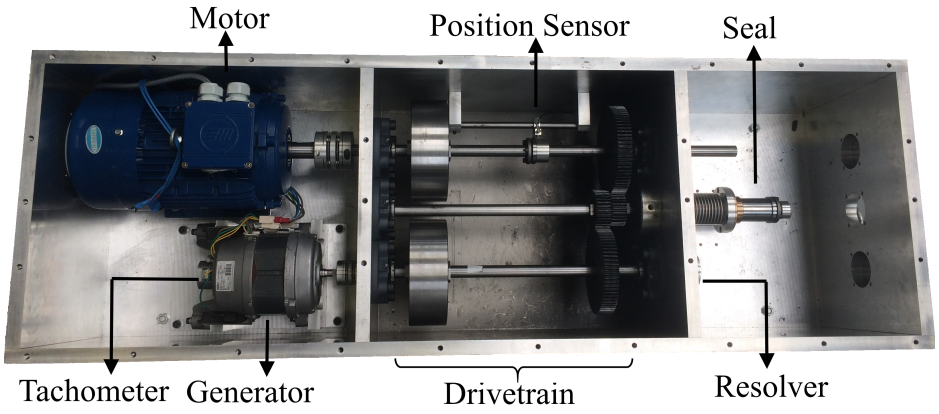


Fig. 6.10 Test-rig assembly

through a set of gears such that the speed ratio of the seal shaft and the power shaft is 3:1. The seal shaft is connected to the generator shaft through a set of gears. The idea behind the integration of the full-ring radial-gap air-riding seal with these technologies is that the seal can benefit from the reduction in vibrations resulting from these technologies.

6.6 Experiment-1: Weight Test

This test was carried out to analyse the stiffness of the air-film for a static shaft. In Experiment-1, known weights were placed on the seal for varying pressure values and the measurement from the sensor was recorded. Fig. 6.11 shows the way in which the weights were placed on the seal ring. The weights were calibrated by weighing them on a scale.

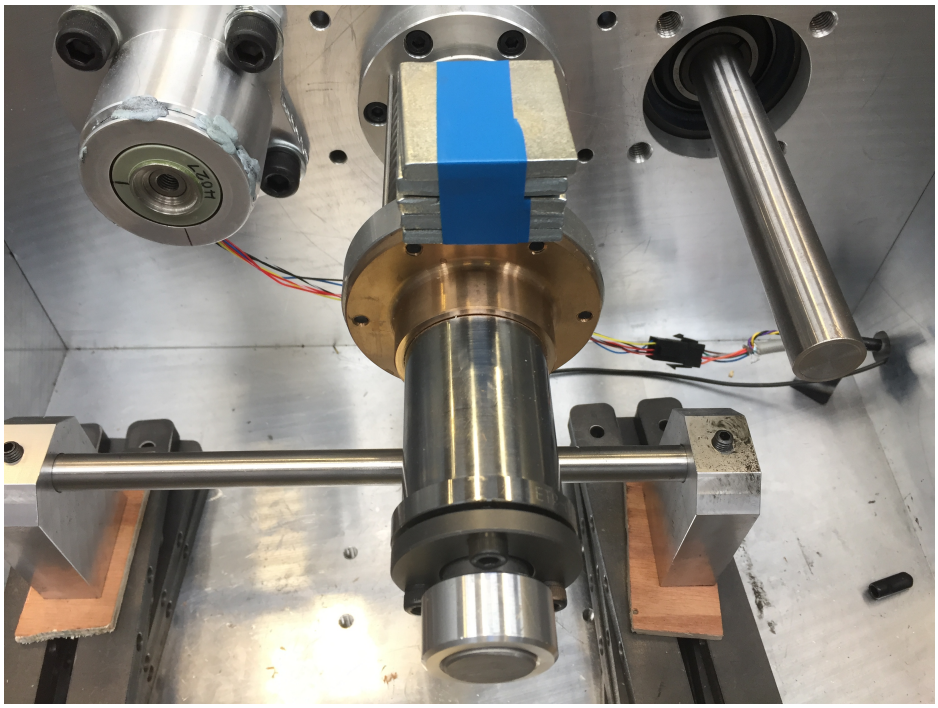


Fig. 6.11 Weight test

A sensor was installed below the shaft so that the point of application of the weights, the shaft centre and the sensor were all aligned in one straight line. So in effect, the effective stiffness of the seal system along Y direction (k_{eff-Y}) was measured. In order to avoid further complexity, k_{eff-Y} will be referred-to as k_{eff} for this study. Fig. 6.12 shows the position where the sensor and sensor mount were placed to take the measurements.

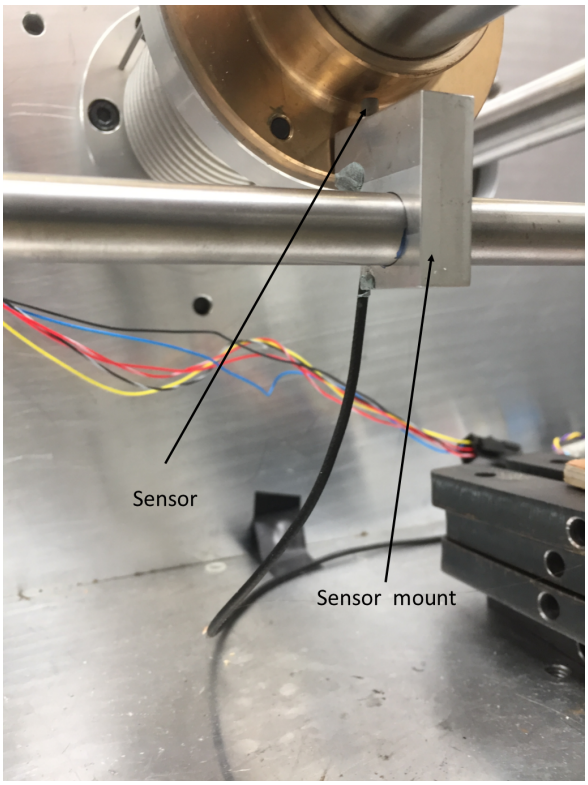


Fig. 6.12 Weight test - sensor and sensor mount

The sensor was connected to a dSPACE controller and the data was monitored through the dSPACE user-interface in real-time. As per the sensor specifications, error was less than 0.1 μm for most operating conditions, with a maximum error of 0.4 μm (specification sheet provided in Appendix 1). A simulink model was created to take the mean value of the readings from the data.

From the initial readings it was realised that there seemed to be some irregularities in the readings (for the same input parameters) depending on the angular position of the shaft with respect to the seal. This indicated that there could be some variation in seal clearance along the circumferential direction; i.e. either the shaft was not central in the seal ring or the profile of the ring and/or the shaft were irregular. So, the weight study was carried out for a range of angular shaft positions with respect to the seal ring.

6.6.1 Methodology

1. The initial angular position of the shaft with respect to the seal was marked as 0 deg. Five more angular positions, at 60 deg increments, were marked.

2. Four different weights, ranging from 0.307 kg to 2.53 kg were placed on the seal and the resulting readings from the sensor were noted.

3. 3 readings were taken for each weight, for each of the 6 angular shaft positions, and the mean value of the reading was considered as the best representation of the data.

4. The first 3 steps were then repeated for 2 different pressures.

6.6.2 Observation

Table 6.3 Experiment-1: Weight Test Data (2 bar)

Pressure(bar)	Angular position(deg)	Mass(g)	Force(N)	Deflection (μm)	Stiffness (N/m)
2	0	307	3.01	5	5.63×10^5
		967	9.49	15	
		1566	15.36	26	
		2533	24.85	46	
2	60	307	3.01	7.5	4.73×10^5
		967	9.49	21.1	
		1566	15.36	33.6	
		2533	24.85	53.6	
2	120	307	3.01	6.4	4.52×10^5
		967	9.49	18.9	
		1566	15.36	31.8	
		2533	24.85	54.4	
2	180	307	3.01	4.2	6.31×10^5
		967	9.49	15.5	
		1566	15.36	24.3	
		2533	24.85	39	
2	240	307	3.01	4.6	6.33×10^5
		967	9.49	13.6	
		1566	15.36	23.3	
		2533	24.85	38.8	
2	300	307	3.01	4	6.09×10^5
		967	9.49	12.8	
		1566	15.36	23	
		2533	24.85	39.4	

Table 6.3 and Table 6.4 show the readings recorded for each shaft position, for different weights, at 2 bar and 4 bar pressure.

Table 6.4 Experiment-1: Weight Test Data (4 bar)

Pressure(bar)	Angular position(deg)	Mass(g)	Force(N)	Deflection (μm)	Stiffness (N/m)
4	0	307	3.01	6.1	4.39×10^5
		967	9.49	20.5	
		1566	15.36	31.5	
		2533	24.85	56	
4	60	307	3.01	7.7	4.30×10^5
		967	9.49	25.3	
		1566	15.36	37.9	
		2533	24.85	58.9	
4	120	307	3.01	6.1	4.95×10^5
		967	9.49	20.7	
		1566	15.36	31.8	
		2533	24.85	50.5	
4	180	307	3.01	5	5.73×10^5
		967	9.49	16.5	
		1566	15.36	26.1	
		2533	24.85	42.9	
4	240	307	3.01	4.4	6.35×10^5
		967	9.49	12.9	
		1566	15.36	21.7	
		2533	24.85	38.5	
4	300	307	3.01	4	6.47×10^5
		967	9.49	12.6	
		1566	15.36	21.3	
		2533	24.85	37.5	

The value of effctive stiffness (k_{eff}) at each shaft position, for each pressure, is calculated by plotting the deflection for each weight against the applied force and taking the slope of the best fit line through the data points. Fig. 6.13 shows an example of the best-fit line method, carried out for a pressure of 2 bar and shaft angular position of 180 deg. The slope of the line was found to be 6.31 $\times 10^5$N/m). It is observed that the stiffness values are not significantly affected by pressure. This may arise due to the flow getting choked and thus minimal increase in mass flow rate with rise of pressure ratio.

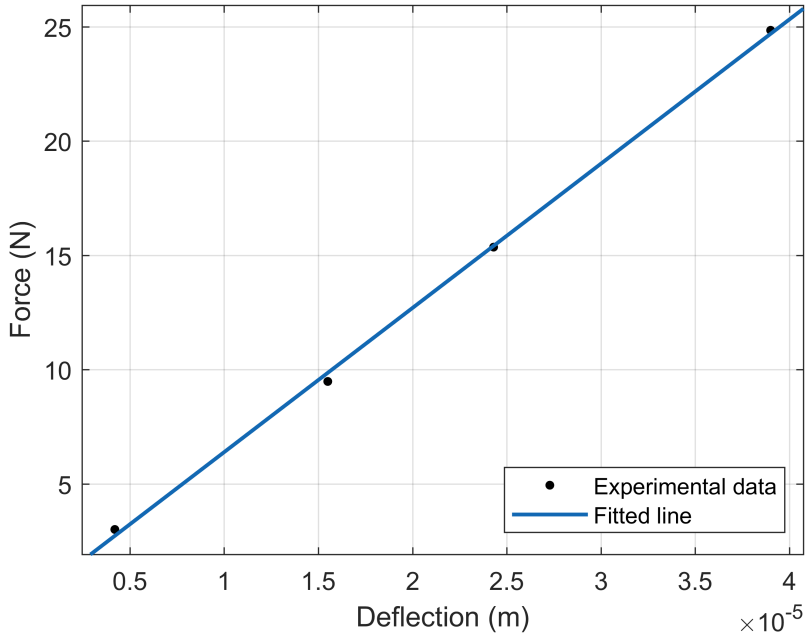


Fig. 6.13 An example of the curve fit exercise, for a pressure of 2 bar

The effective stiffness values (k_{eff}) were then plotted with respect to the angular shaft position, for each pressure. Fig. 6.14 shows the variation of the measured stiffness with angular position of the shaft, for 2 different pressures.

From Fig. 6.14, it is evident that the stiffness, and hence the seal gap height, varies circumferentially. To have a better understanding of these results, it is important to study the relationship between the 3 major stiffness contributors in the seal system.

The seal system and the Weight Test experiment can be effectively represented as:

where, k_{sec_seal}, $k_{air-film}$ and k_{shaft} are the stiffness values of the secondary seal, air-film and shaft respectively. F is the applied Force and δ is measured deflection.

Let k_{eff} be the effective stiffness that was calculated from the experimental results.So, k_{eff} can be expressed as:

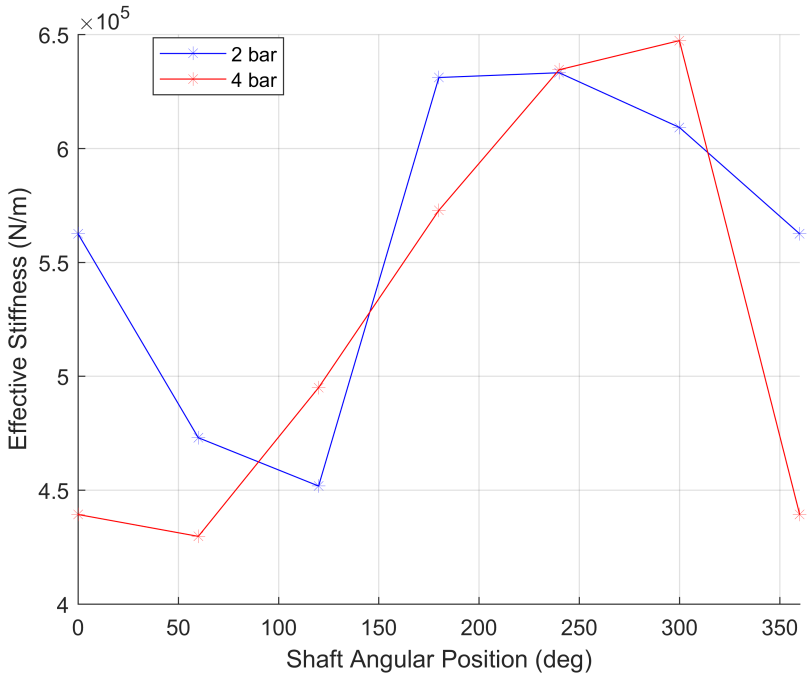


Fig. 6.14 Variation of measured stiffness with angular position of the shaft

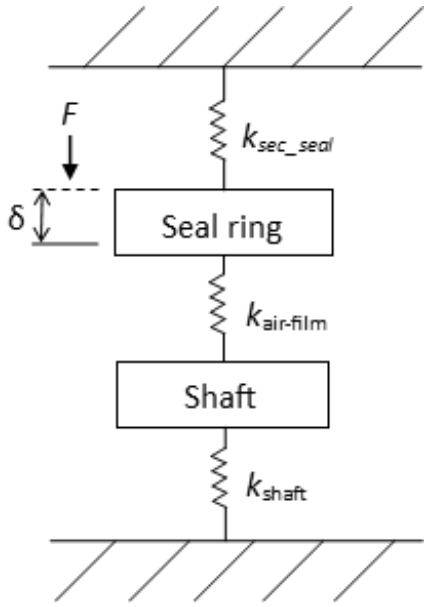


Fig. 6.15 Variation of measured stiffness with angular position of the shaft

$$k_{eff} = k_{sec_seal} + \frac{1}{\frac{1}{k_{air-film}} + \frac{1}{k_{shaft}}} \tag{6.17}$$

Or,

$$(k_{air-film} + k_{shaft})(k_{eff} - k_{sec_seal}) = k_{air-film}.k_{shaft} \tag{6.18}$$

On rearranging the terms in Eq. 6.18, it can be written as:

$$k_{air-film} = \frac{-k_{shaft}(k_{eff} - k_{sec_seal})}{k_{eff} - (k_{sec_seal} - k_{shaft})} \tag{6.19}$$

So in order to evaluate Eq. 6.19, k_{sec_seal} and k_{shaft} had to be determined.

Similar weight tests were carried out on the secondary seal and the shaft. To carry out these tests, the shaft was pulled out towards the seal outlet till the *shaft adapter* came out of the seal ring, to ensure that there was no contact between the shaft and the seal ring during these tests (as shown in Fig. 6.16).

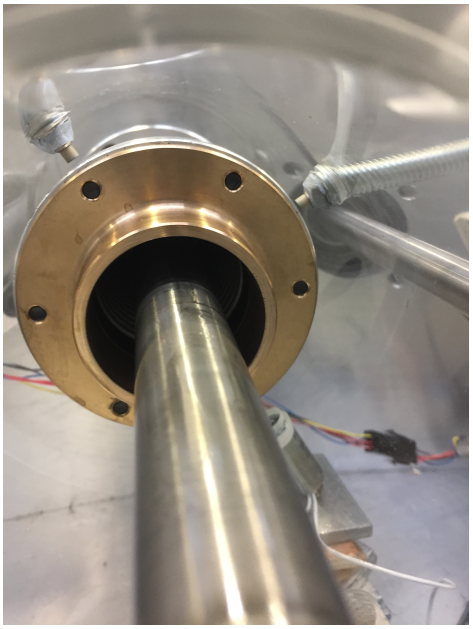


Fig. 6.16 Weight test - Seal adapter pulled out

Table 6.5 and Table 6.6 show the results from the weight test on the secondary seal and the shaft, respectively.

Table 6.5 Weight test - secondary seal

Mass(g)	Force(N)	Deflection (µm)	Stiffness (N/m)
307	3.01	5.9	5.06×10^5
967	9.49	19	
1566	15.36	31	
2533	24.85	49	

Table 6.6 Weight test - shaft

Mass(g)	Force(N)	Deflection (µm)	Stiffness (N/m)
307	3.01	18	1.75×10^5
967	9.49	58	
1566	15.36	90	
2533	24.85	143	

The shaft deflections were also verified by simulating the shaft and bearings on the Matlab rotordynamic model developed by Friswell *et al.* [91]. A good correlation was found between the experimental results and the simulation values.

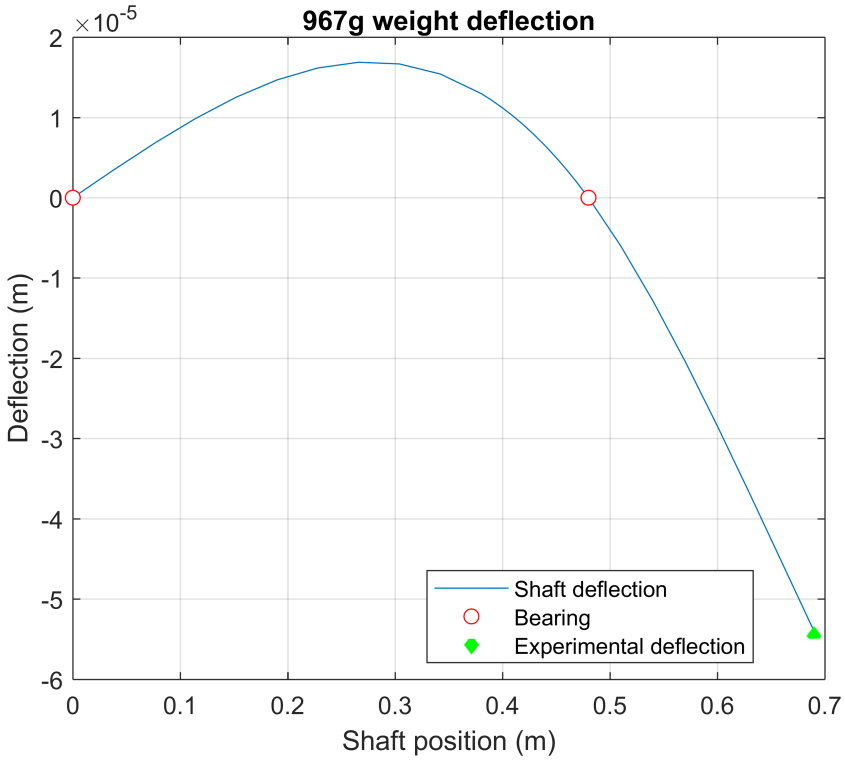


Fig. 6.17 Comparison between the simulation and experimental results, for determining shaft stiffness

After determining the values of shaft stiffness (k_{shaft}) and secondary seal stiffness (k_{sec_seal}), their values are substituted in Eq. 6.19. Fig. 6.18 shows a plot of air-film stiffness with respect to angular shaft position. On comparing with Table 6.5 it is observed that the secondary film stiffness is comparable to air film stiffness. It is also worth mentioning that the air film stiffness calculated here is significantly lower than the values derived from 1-D, 2-D and CFD simulations at a pressure of 4 bar (1.75 MN/m, 1.85 MN/m and 2.24 MN/m respectively).

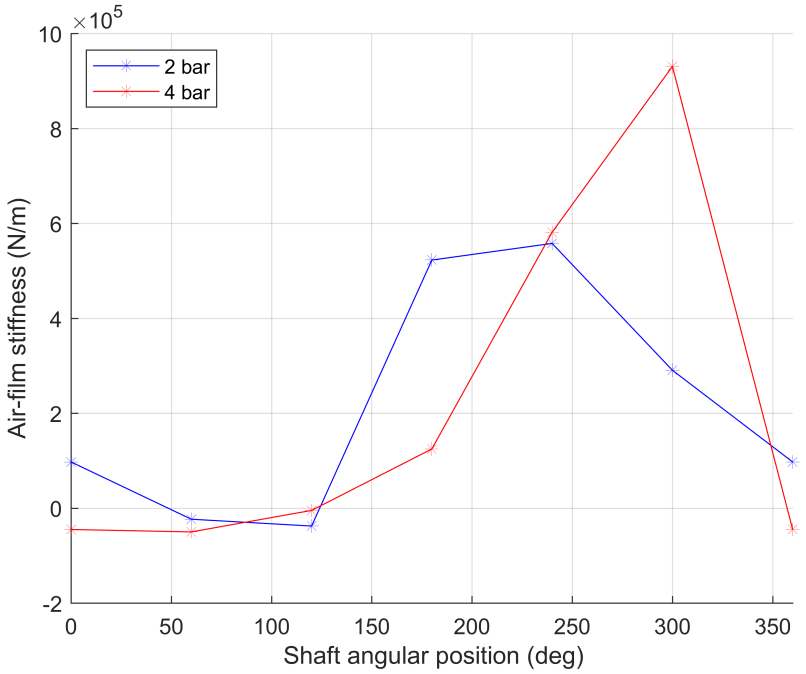


Fig. 6.18 Variation of air-film stiffness with shaft angular position

6.6.3 Conclusion

The conclusions drawn from the static weight test are as follows:

- It can be observed from Fig. 6.18 that the film stiffness along Y direction varies with the angular position of the shaft with respect to the seal. This confirmed that the average seal gap varied circumferentially.
- It can also be observed from Fig. 6.18 that for some angular positions, the air-film stiffness is negative. It has been shown in 3.17 that for the given pressure ratio, the fluid-film will have a negative stiffness if the seal gap is either diverging (i.e $h_{out} > h_{in}$)

or close to parallel. This indicated that there is an axially diverging seal gap along those angular positions. So it can be concluded that there was machining errors/imperfections in the seal ring. The nominal values of h_{out} and h_{in} were supposed to be $50 \pm 2\mu m$ and $14 \pm 2\mu m$ respectively.

- The film stiffness value of $\sim 0.5 MN/m$ calculated in the weight test is significantly lower than those evaluated from 1-D,2-D and CFD (1.75 MN/m, 1.85 MN/m and 2.24 MN/m respectively). If this was due to a larger seal gap, based on Fig. 5.21, it would imply that the seal outlet height is perhaps > 40μm.

From the studies carried out, it was quite evident that the seal ring was not manufactured to required specifications. An effort at improving the seal ring design was made at the manufacturing facility in the University of Nottingham but due to lack of such precise machining or measuring equipments, it was not possible to achieve the desired results. The lead time involved to manufacturing a new seal ring and possibly a new shaft adapter, with the time required for assembly, testing and analysis, was too long for considering it as possibility for including it in this thesis. As stated above, it was still possible to demonstrate that film stiffness predicted from the simulations and analysis could be achieved practically, with precise machining of seal components.

The 1-D, 2-D and CFD analyses were initially carried out at a pressure of 10 bar as it was known that maximum pressure that can be achieved from the compressor in the laboratory was 10 bar. Unfortunately, pressures higher than 4 bar could not be achieved due to some limitations in the test rig, so all the simulations had to be rerun at 4 bar. Rotational testing of the rig for 9000 rpm was also not possible as the bearingless machine was not functioning properly. As the researcher who had designed the bearingless machine was not available, and the shaft was permanently fitted to the motor, the lead time involved in mounting and testing a new motor made it practically impossible to carry out a dynamic testing of the seal for reporting in this thesis.

6.7 Experiment-2: Strike Test

This test was carried out to determine the response of the fluid film for shaft excitations.

6.7.1 Methodology

The seal ring was struck through a solenoid actuator and the response of the fluid film was recorded through sensor which was placed in such a way so that the actuator, shaft centre and the sensor was in a straight line.

Fig. 6.19 and Fig. 6.20 show the set-up of the solenoid striker and sensors. It should be noted that these pictures are being provided merely to act as an indication of the placement of the solenoid striker and the sensors, and they are not meant to provide a real set-up of the experiment. As it can be observed, in both these pictures the shaft has been pulled out so that the seal adapter is not inside the seal ring. During the experiments, the shaft was pushed back in, with the shaft adapter inside the seal ring.

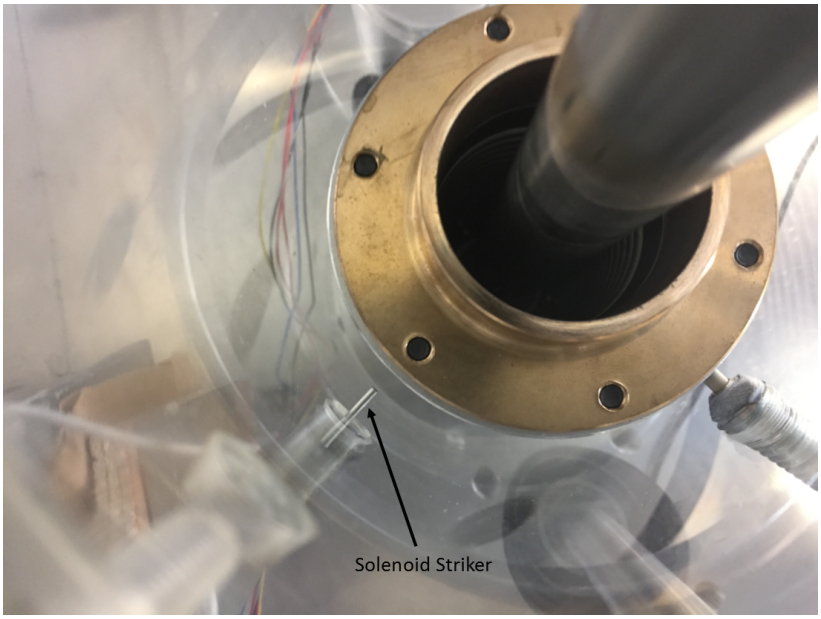


Fig. 6.19 Solenoid striker used to strike the seal ring

The solenoid striker was used to strike the seal ring three times and the readings from the sensor were recorded.

6.7.2 Observation

Fig. 6.21 shows the readings recorded from the sensor. On zooming-in on the middle peak in the plot, the transient vibrations in the seal system could be visualised, as shown in Fig. 6.22.

The data was then truncated from the peak, as shown in the Fig. 6.23. To determine the frequencies in the vibration data, Fast Fourier Transform on the truncated data was carried

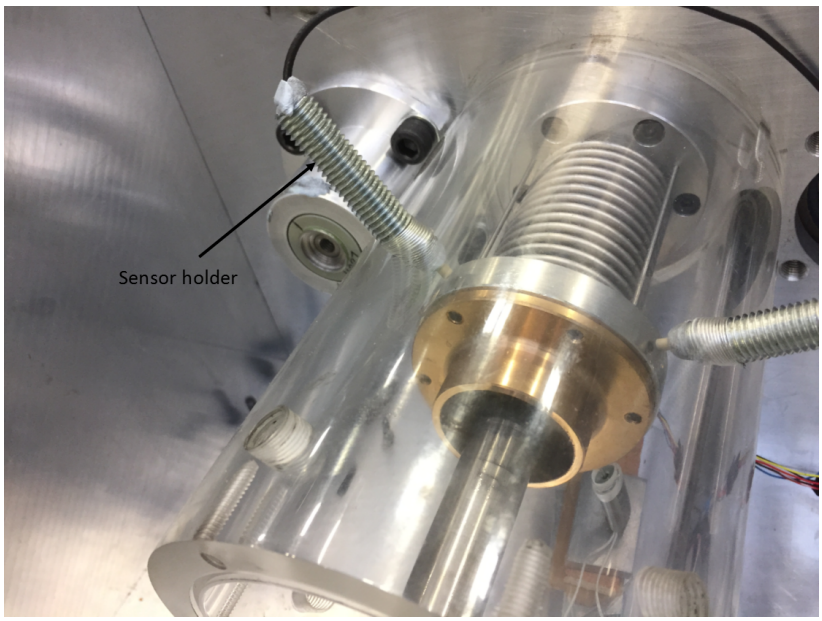


Fig. 6.20 Sensor Holders and solenoid striker used for the strike test

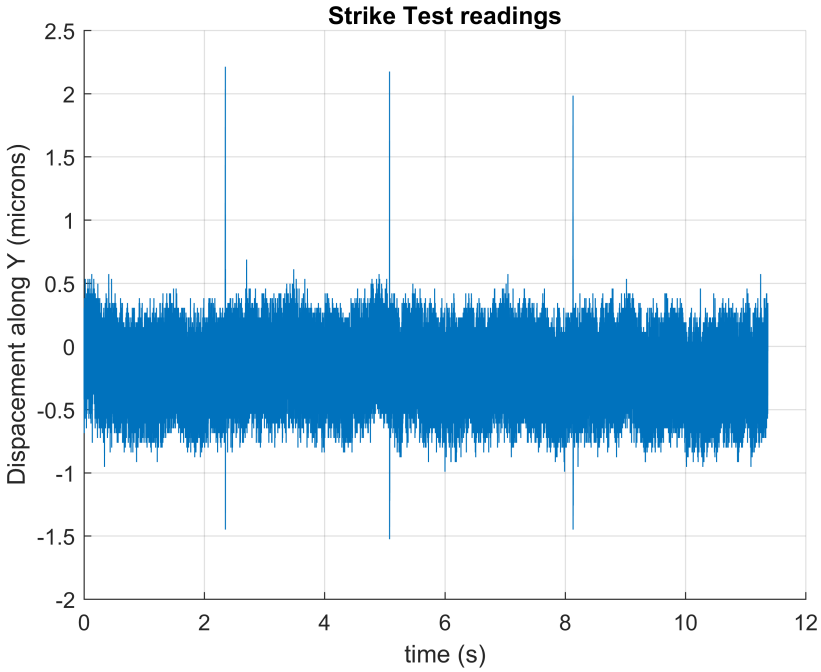


Fig. 6.21 Strike Test - readings from the sensor

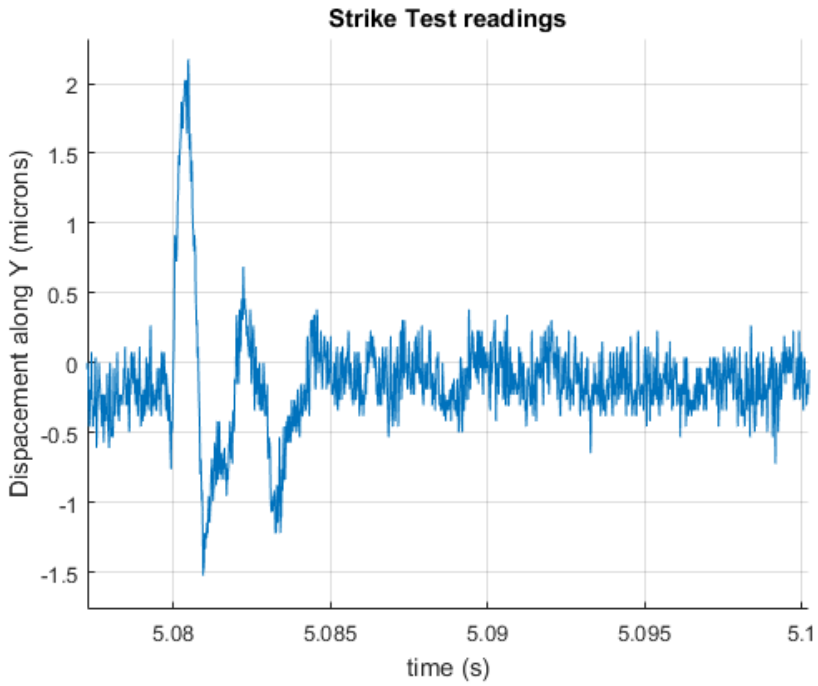


Fig. 6.22 Strike Test - Sensor readings (zoomed-in on one of the strikes)

out on Matlab. Fig. 6.24 shows the single sided amplitude spectrum obtained from the Fast Fourier Analysis of the signal.

Neglecting the excitation frequency, from Fig. 6.24 the resonance frequency was found to be at 513.6 Hz. This was coherent with the Fast Fourier Transform of the two other strikes as well, with resonance frequencies of 495.7 Hz and 505.9 Hz. So the average resonance frequency was calculated as:

$$\omega_{avg} = 505\text{Hz} \tag{6.20}$$

6.7.3 Conclusion

As the resonance frequency of the seal ω_{avg} is still higher than the shaft excitation frequency Ω_{max_shaft} of 333.33 Hz (due to unbalance), it confirms the conclusion drawn from the simulations that the seal system has a higher resonance frequency than maximum shaft excitation frequency.

Although slightly lower, ω_{avg} value of 505 Hz has a good correlation with the ω_{seal} value of 569.96 Hz calculated in Eq. 6.11.

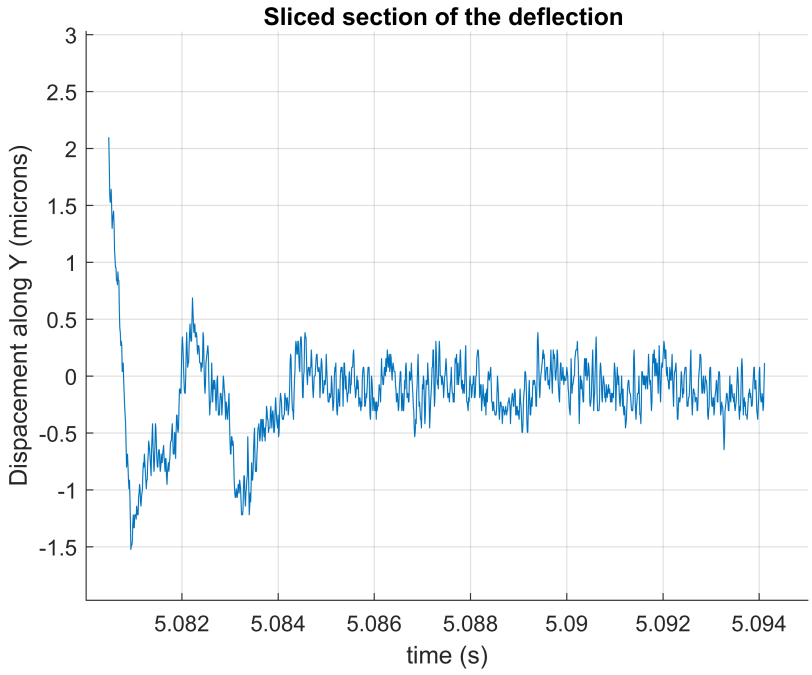


Fig. 6.23 Strike Test - Truncated data

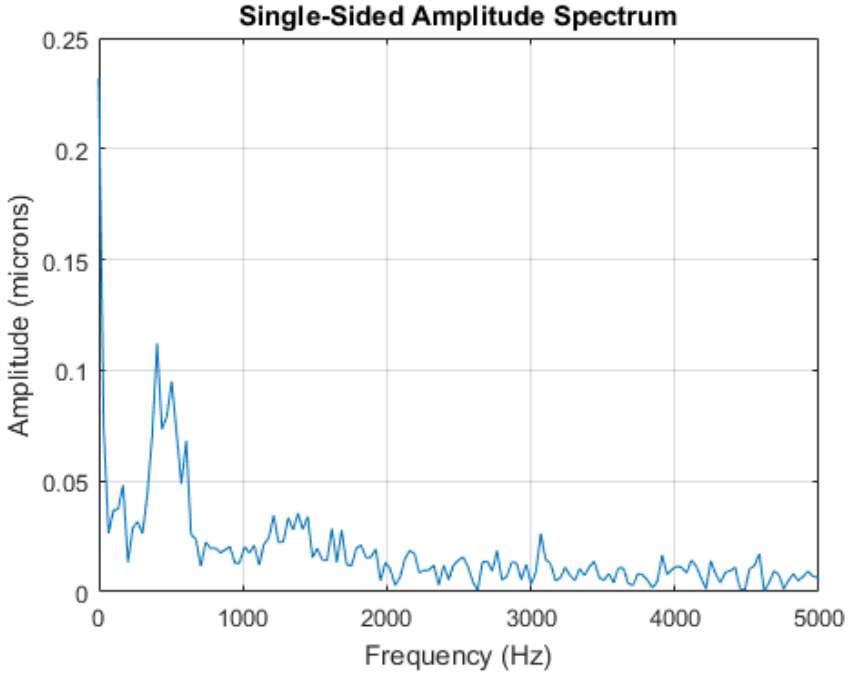


Fig. 6.24 Strike Test - Fourier Transform

Based on the above observation, it can be concluded that there was a good correlation between the resonance frequencies of the seal calculated from the CFD and experimental analysis.

6.8 Summary and Discussion

In this chapter, stability analysis of the seal, a detailed design of the seal system and the experimental results from the rudimentary tests carried out on the seal have been presented.

With the knowledge of rotordynamic coefficients of the seal air-film, Routh Hurwitz stability analysis was carried out on the characteristic polynomial of the equation of motion of the seal. On evaluating the Routh array it was concluded that the system was stable. Two critical criteria were identified for the rotational operation of the seal - frequency criterion and relative movement criterion. On analysing the seal stability for these two criteria it was found that the seal satisfied both these criteria.

A detailed design of the seal system was presented in this chapter. This was followed by the description and conclusions drawn from two experiments carried out on the seal system. From the weight test, it was observed that there was a variation in effective stiffness for varying shaft angular positions with respect to the shaft. On further analysis, it was clear that the air-film stiffness was negative for certain shaft angular positions, which indicated that there must be a diverging seal gap for the respective angular position. Based on these findings it was concluded that the seal ring was not manufactured to specifications and a more accurately manufactured seal ring was required for any further analysis.

For the next experiment, a solenoid striker was used to strike the seal, for an inlet pressure of 4 bar. From the recorded sensor readings it was possible to calculate the natural frequency of the seal, which was found to have a good correlation with the value predicted from the CFD simulations.

Chapter 7

Conclusions and Suggested Future Research

In this thesis, a novel design of a radial-gap air-riding seal has been presented. As discussed in Chapter 1 and Chapter 2, prior art in the field of radial-gap air-riding seals consist of segmented type seals. The design presented in thesis incorporates a full-ring seal which is supported by a secondary sealing structure. A detailed design of this new category of seal has been presented. Results have been discussed from the 1-D, 2-D and CFD simulations of the fluid-film in the seal and some characteristic features of the full-ring radial-gap air-riding seal has been identified.

The main conclusions drawn from the modelling and analysis presented in this thesis has been summarised in Section 7.1. In Section 7.2, a number of areas of future work are proposed based on the key findings of the work presented in this thesis.

7.1 Conclusions

A review of the prior art in the field of seals employed in the contemporary Gas Turbine Engines highlighted the need for developing better sealing systems to cope with the challenges posed by the future engines (larger engines, higher OPRs, higher engine efficiency etc.). Several authors identified air-riding seals as a promising option for replacing the traditional seals employed in Gas Turbine Engines.

Majority of prior-art in the field of air-riding seals was found to be composed of face seals or axial gap seals. The importance of generating sufficient air-film stiffness in these

seals was identified from the reviewed literature. Various hydrostatic and hydrodynamic face seal designs developed by authors during last 3-4 decades were reviewed. Several authors were found to use spiral grooves to enhance hydrodynamic lift generation properties of the seal.

It was identified that one of key challenges faced by axial-gap seals is differential thermal growth of engine parts which resulted in net motions of the order of 1 cm. This resulted in an added complexity in designing the seal components. It was realised that radial gap seals would benefit from lower net motions of engine parts, but one of the key challenges faced by these seals would be to contend with the once-per-revolution vibrations.

Circumferential seals or segmented seals were the only kind of radial-gap seal documented in the literature. In Gas Turbine Engines, they were mostly found to be employed near bearing chambers to seal the flow of air to the oil wetted areas. As the seal ring used here was segmented, several issues associated with this segmented design were identified, like leakage of flow between the segments, rubbing between parts etc.

This was the inspiration behind the research work presented in this thesis. A full-ring radial-gap air-riding seal would benefit from lower net travel of the rotor that it would need to accommodate and it would not have the added complexity of a segmented ring design. In spite of these benefits, the key challenge in designing such a seal would be to generate a sufficiently stiff yet flexible seal for accounting for once per revolution vibrations.

The seal gap geometry and a possible seal assembly schematic for this novel seal design was presented in Chapter 3. The suitability of employing Navier-Stokes equations to model the flow in the thin film was confirmed by computing the Knudsen number. The governing equation derived from the Navier Stokes equation for 1-D flow was used to generate the pressure profile through the seal. The air-film stiffness in the seal was determined by calculating the net lift force generated by the fluid film for small perturbations. This was followed by a 2-D analysis of the fluid flow through the seal by using Reynolds equations for modelling thin fluid films. A numerical modelling scheme for solving the Reynolds Equations was developed by using a central finite difference model. It was realised that most of the lift generated in the fluid film was by hydrostatic means. Stiffness matrix of the fluid film was calculated by calculating the lift force generated by the film for small perturbations. On plotting the film stiffness against pressure ratios it was realised that the stiffness increases linearly with increasing pressure ratios. On studying the variation of stiffness for varying seal outlet height, it was realised that a converging seal gap is necessary for generating positive lift force from the film.

The preliminary CFD modelling of fluid film geometry was carried out in Chapter 4. A literature review on CFD modelling methodologies and turbulence models used for modelling thin films suggested the use of $k-\omega$ SST turbulence model. A grid independence study was carried out for the CFD model set up on ANSYS CFX and the solution was found to be grid-independent for grid size of approximately 400k nodes. The preliminary verification work carried out in this chapter formed the basis of steady state and transient CFD simulations carried out in Chapter 4.

CFD simulations carried out in Chapter 5 was essential in understanding the properties of the fluid film. Results from the steady state CFD simulations were found to have a good correlation with the 2-D results. Stiffness matrix of the fluid film was calculated by computing the lift force generate for small perturbations. This was followed by Fluid-Structure Interaction analyses to analyse the transient response of the fluid film to shaft perturbations. Two different FSI studies were carried out. For the first study, shaft displacements in the fluid film were recorded when an oscillating force was acting on the shaft. This study was carried out for a range of frequencies. From these analyses, the resonance frequency of the fluid film at a pressure of 4 bar was found to be 227.27 Hz. For the second study, the shaft was moved in the air-film in a petal-like path and the resultant force on the shaft were recorded. Singular value decomposition method was used to find a best representation of the force values for the thousands of data points and the damping coefficient of the fluid film was evaluated.

After completing the performance analysis of the fluid film, it was important to analyse its stability during its operating conditions. Chapter 6 was dedicated towards analysing the stability of the fluid film, designing the full seal system and carrying out some rudimentary testing of the seal. As rotordynamic coefficients were now known, following the CFD analyses carried out in Chapter 5, Routh-Hurwitz stability analysis was carried out by computing the Routh array for the characteristic equation of the equation of motion for the fluid film. From Routh-Hurwitz analysis, it was concluded that the system is stable. Dynamic operability of the film was then analysed in terms of two critical criteria that were identified - frequency criteria and relative movement criteria. The seal system was found to satisfy the frequency criterion as the resonance frequency of the air-film was much higher than the maximum excitation frequency from once-per-revolution vibrations of a shaft rotating at 20,000 rpm. The system was also found to satisfy the relative movement criterion as the relative movement of the shaft with respect to the seal ring was always found to be less than the minimum seal height. Following the stability analysis, full designing of the seal system was carried out. Chapter 6 explains each element of the seal system in detail. Two rudimentary tests were carried out on the seal test rig. A weight test was carried out to analyse the static stiffness of the fluid film. It was realised that the stiffness of the film in a

radial direction (say Y) varied with different angular shaft position relative to the seal ring. The analyses carried out on various shaft position led to the conclusion that the seal ring might not have been manufactured as per specifications and for certain angular positions, film stiffness was found to be negative, which, along other factors, might be caused by a diverging rather than a converging seal gap. It was still possible to demonstrate from this test that if the seal ring is manufactured as per specification (with a tolerance of 1 μm), it was possible to achieve the stiffness values reported from 1-D, 2-D and CFD simulations. For the next experiment, a solenoid actuator was used to strike the seal ring when an inlet pressure of 4 bar was applied. The natural frequency of the seal was calculated by carrying out Fast Fourier Transform of the data recorded from the sensor. A good correlation was found between the experimental results and the predicted seal natural frequency from CFD analysis.

7.2 Suggested Future Research

Future research into a full-ring radial-gap air-riding seal could be initiated by including a number of physical processes and geometric configurations not considered in this thesis. The predictive capability of the modelling work could be further extended by considering different thermal operating conditions of the seal. This would allow a better understanding of the performance of these seals for actual operating conditions and throw some light on the locations in the gas turbine engine where they could be successfully employed.

Although a coupled Fluid-Structure Interaction model was developed for simulating the rotor interaction with the fluid film, the studies carried out were mostly focused on study of frequency response of the fluid film and characterising the damping achieved from the fluid film. This model could be further extended to account for the thermodynamics of the FSI.

As this was the first effort in designing this new category of seals, there is a lot of scope for further improvements in seal design by analysing many more possible geometries and design features. In the current configuration, the seal does not benefit from hydrodynamic lift generation. This could be investigated by cutting spiral grooves in the rotor or stator for adding more stiffness in the fluid film.

It was also observed that the secondary seal stiffness increased considerably by adding the face plate and flexures. It would certainly be possible to reduce this added stiffness by having lighter face plates or by considering a different design of the secondary seal. Another

key area of investigation would be analyse the performance benefits achieved from using different materials for manufacturing the seal ring

Due to machining errors and other unfortunate circumstances, it was not possible to carry out any dynamic testing of the seal system in the integrated test-rig. So the current experimental results could be extended further and the results from the simulation models can be further validated by carrying out the dynamic testing of the seal system for accurately manufactured seal components.

References

[1] Boeing. Current market outlook 2016-2035, July 2016. [online] http://www.boeing.com/resources/boeingdotcom/commercial/about-our-market/assets/downloads/cmo_print_2016_final_updated.pdf.

[2] Glenn Garrison and Alan McNickle. Air riding seal, May 20 2005. US Patent App. 11/134,249.

[3] G. F. Holle H. L. Stocker, D. M. Cox. Aerodynamic performance of conventional and advanced design labyrinth seals with solid-smooth abradable, and honeycomb lands. *US Patent EDR-9339*, (NASA-CR-135307), November 1977.

[4] LJ Dobek. Development of mainshaft seals for advanced air breathing propulsion systems, 1973. NASA CR-121177.

[5] Philip Varney and Itzhak Green. Impact phenomena in a noncontacting mechanical face seal. *Journal of Tribology*, 139(2):022201–022201–8, 2016. 10.1115/1.4033366.

[6] Kenneth A Lahrman. Fluid bearing face seal for gas turbine engines, December 29 1992. US Patent 5,174,584.

[7] Mingfong Hwang, Adam N Pope, and Bernie Shucktis. Advanced seals for engine secondary flowpath. *Journal of propulsion and power*, 12(4):794–799, 1996.

[8] John Munson and Glenn Pecht. Development of film riding face seals for a gas turbine engine. *Tribology transactions*, 35(1):65–70, 1992.

[9] James Gardner. Development of a high speed, high temperature, compressor discharge seal. In *35th Joint Propulsion Conference and Exhibit*, page 2684, 1999.

[10] Philip C Stein. Circumferential seals, April 2019. [online] https://www.steinseal.com/brochures/details.asp?tid=122&nid=315.

[11] Philip C Stein. Seal for sealing between a rotating member and a housing, April 4 1978. US Patent 4,082,296.

[12] Mark R Borkiewicz. Segmented hydrodynamic seals for sealing a rotatable shaft, April 23 1996. US Patent 5,509,664.

[13] Mingfong Hwang. Hydrodynamic lift seal for use with compressible fluids, November 14 2000. US Patent 6,145,843.

[14] Ronald Horace Warring. *Seals and sealing handbook*. Gulf Publishing Company, Houston, 1981.

[15] A.P. Charles and Q.C. Alfred. Packing for rotating bodies. *US Patent 1,482,031*, January 29 1924.

[16] John F Justak and Peter F Crudgington. Evaluation of a film riding hybrid seal. *AIAA Paper*, (2006-4932), 2006.

[17] David L Rhode. Labyrinth seal. *US Patent 5,244,216*, September 14 1993.

[18] C. Delebarre, V. Wagner, J.Y. Paris, G. Dessein, J. Denape, and J. Gurt-Santanach. An experimental study of the high speed interaction between a labyrinth seal and an abradable coating in a turbo-engine application. *Wear*, 316(1):109 – 118, 2014.

[19] Tong Seop Kim and Kyu Sang Cha. Comparative analysis of the influence of labyrinth seal configuration on leakage behavior. *Journal of Mechanical Science and Technology*, 23(10):2830–2838, 2009.

[20] Dara W Childs and John M Vance. Annular gas seals and rotordynamics of compressors and turbines. In *Proceedings of the 26th Turbomachinery Symposium*, pages 201–220, 1997.

[21] Ruben O Peterson. Brush seal and the like, March 17 1959. US Patent 2,878,048.

[22] Saim Dinc, Mehmet Demiroglu, Norman Turnquist, Jason Mortzheim, Gayle Goetze, John Maupin, James Hopkins, Christopher Wolfe, and Mark Florin. Fundamental design issues of brush seals for industrial applications. In *ASME Turbo Expo 2001: Power for Land, Sea, and Air*, pages V003T01A080–V003T01A080. American Society of Mechanical Engineers, 2001.

[23] Matthias Neef, Erik Sulda, Norbert Sürken, and Jan Walkenhorst. Design features and performance details of brush seals for turbine applications. *ASME Paper No. GT2006-90404*, 2006.

[24] JG Ferguson. Brushes as high performance gas turbine seals. In *ASME 1988 International Gas Turbine and Aeroengine Congress and Exposition*, pages V002T02A006–V002T02A006. American Society of Mechanical Engineers, 1988.

[25] David Robert Skinner, Bharat S Bagepalli, Robert Harold Cromer, Osman Saim Dine, Norman Arnold Turnquist, and Christopher Edward Wolfe. Combined brush seal and labyrinth seal segment for rotary machines, May 12 1998. US Patent 5,749,584.

[26] Waukesha Bearings. Brush seals, April 2019. [online] https://www.waukbearing.com/en/technical-resources/company-literature/.

[27] Margaret P Proctor and Irebert R Delgado. Leakage and power loss test results for competing turbine engine seals. *NASA, Report No. TM-2004-213049*, 2004.

[28] Yahya Dogu and Mahmut F Aksit. Brush seal temperature distribution analysis. *Journal of engineering for gas turbines and power*, 128(3):599–609, 2006.

[29] Wang-Long Li. Analytical modelling of ultra-thin gas squeeze film. *Nanotechnology*, 10(4):440, 1999.

[30] Adam N Pope. Gas bearing sealing means, February 8 1994. US Patent 5,284,347.

[31] JTS Ma. An investigation of self-acting foil bearings. *Journal of Basic Engineering*, 87(4):837–846, 1965.

[32] MA Barnett and A Silver. Application of air bearings to high-speed turbomachinery. Technical report, SAE Technical Paper, 1970.

[33] WA Gross and EC Zachmanaglou. Perturbation solutions for gas-lubricating films. *Journal of Basic Engineering*, 83(2):139–144, 1961.

[34] DN Ha, TA Stolarski, and S Yoshimoto. An aerodynamic bearing with adjustable geometry and self-lifting capacity. part 1: self-lift capacity by squeeze film. *Proceedings of the Institution of Mechanical Engineers, Part J: Journal of Engineering Tribology*, 219(1):33–39, 2005.

[35] JS Ausman. Linearized ph stability theory for translatory half-speed whirl of long, self-acting gas-lubricated journal bearings. *Journal of Basic Engineering*, 85(4):611–618, 1963.

[36] V Castelli and HG Elrod. Solution of the stability problem for 360 deg self-acting, gas-lubricated bearings. *Journal of Basic Engineering*, 87(1):199–210, 1965.

[37] EOJ Salbu. Compressible squeeze films and squeeze bearings. *Journal of Basic Engineering*, 86(2):355–364, 1964.

[38] E Reinhardt and JW Lund. The influence of fluid inertia on the dynamic properties of journal bearings. *Journal of Lubrication Technology*, 97(2):159–165, 1975.

[39] Zenglin Guo, Toshio Hirano, and R Gordon Kirk. Application of cfd analysis for rotating machinery: Part 1—hydrodynamic, hydrostatic bearings and squeeze film damper. In *ASME Turbo Expo 2003, collocated with the 2003 International Joint Power Generation Conference*, pages 651–659. American Society of Mechanical Engineers, 2003.

[40] T Raparellj and V Viktorov. Theoretical investigation of fluid inertia effects and stability of self-acting gas journal bearings. *Journal of tribology*, 121:837, 1999.

[41] Joab J Blech. On isothermal squeeze films. *Journal of lubrication technology*, 105(4):615–620, 1983.

[42] Hans Pennink et al. The gas lubricated spiral grooved face seal in the process industry. In *Proceedings of the 14th Turbomachinery Symposium*. Texas A&M University. Turbomachinery Laboratories, 1985.

[43] Josef Sedy. A new self-aligning mechanism for the spiral-groove gas seal stability. In *American Society of Lubrication Engineers and American Society of Mechanical Engineers, Lubrication Conference, Dayton, Ohio*, page 1979, 1979.

[44] Abraham Lipschitz. Hydrodynamic non-contacting seal for rotary machines, December 20 1983. US Patent 4,421,321.

[45] Robert S Wentworth. Face seal with automatic face convergence means, February 2 1988. US Patent 4,722,534.

[46] James F Gardner. Spiral groove gas lubricated seal, August 13 1991. US Patent 5,039,113.

[47] Yuming Wang. Face seal with spiral grooves, November 28 2000. US Patent 6,152,452.

[48] Glenn Garrison and Alan McNickle. Air riding seal, January 11 2007. US Patent App. 11/134,249.

[49] Glenn M Garrison and Alan D McNickle. Air riding seal, September 25 2012. US Patent 8,272,643.

[50] Ingo Henry Johannes Jahn. Air-riding seal, December 30 2014. US Patent 8,919,779.

[51] Ming-Fong Hwang and Adam N Pope. Expanding circumferential seal with upper-cooled runner, April 12 1994. US Patent 5,301,957.

[52] Thurai Manik Vasagar, Glenn M Garrison, and Alan D McNickle. Low and reverse pressure application hydrodynamic pressurizing seals, January 22 2013. US Patent 8,356,819.

[53] John Munson. Circumferential sealing arrangement, March 15 2011. US Patent 7,905,495.

[54] Osborne Reynolds. An experimental investigation of the circumstances which determine whether the motion of water shall be direct or sinuous, and of the law of resistance in parallel channels. *Proceedings of the royal society of London*, 35(224-226):84–99, 1883.

[55] B Popper and M Reiner. The application of the centripetal effect in air to the design of a pump. *British Journal of Applied Physics*, 7(12):452, 1956.

[56] HAROLD G Elrod. A derivation of the basic equations for hydrodynamic lubrication with a fluid having constant properties. *Quarterly of Applied Mathematics*, 17(4):349–359, 1960.

[57] WE Langlois. Isothermal squeeze films. *Quarterly of Applied Mathematics*, 20(2):131–150, 1962.

[58] Adi Minikes, Izhak Bucher, and Shimon Haber. Levitation force induced by pressure radiation in gas squeeze films. *The Journal of the Acoustical Society of America*, 116(1):217–226, 2004.

[59] Mohamed Fourka, Yong Tian, and Marc Bonis. Prediction of the stability of air thrust bearings by numerical, analytical and experimental methods. *Wear*, 198(1):1–6, 1996.

[60] TA Stolarski and Wei Chai. Load-carrying capacity generation in squeeze film action. *International journal of mechanical sciences*, 48(7):736–741, 2006.

[61] RJ Fritz. The effects of an annular fluid on the vibrations of a long rotor, part 1—theory. *ASME J. Basic Eng*, 92:923–929, 1970.

[62] C-I Yang and TJ Moran. Finite-element solution of added mass and damping of oscillation rods in viscous fluids. *Journal of applied mechanics*, 46(3):519–523, 1979.

[63] VN Constantinescu and S Galetuse. Operating characteristics of journal bearings in turbulent inertial flow. *Journal of Lubrication Technology*, 104(2):173–179, 1982.

[64] Noël Brunetière and Bernard Tournerie. The effect of inertia on radial flows—application to hydrostatic seals. *Journal of tribology*, 128(3):566–574, 2006.

[65] AM Beskok, George Em Karniadakis, and William Trimmer. Rarefaction and compressibility effects in gas iviicroflows. *Journal of Fluids Engineering*, 118(3):448–456, 1996.

[66] Marco Tulio C Faria and Luis San Andres. On the numerical modeling of high-speed hydrodynamic gas bearings. *Journal of Tribology*, 122(1):124–130, 2000.

[67] PYP Chen and EJ Hahn. Use of computational fluid dynamics in hydrodynamic lubrication. *Proceedings of the Institution of Mechanical Engineers, Part J: Journal of Engineering Tribology*, 212(6):427–436, 1998.

[68] KP Gertzos, PG Nikolakopoulos, and CA Papadopoulos. Cfd analysis of journal bearing hydrodynamic lubrication by bingham lubricant. *Tribology International*, 41(12):1190–1204, 2008.

[69] Satish B Shenoy, RS Pai, DS Rao, and Raghuvir B Pai. Elasto-hydrodynamic lubrication analysis of full 360'journal bearing using cfd and fsi techniques. *World Journal of Modelling and Simulation*, 5(4):315–320, 2009.

[70] AI Sayma, C Breard, M Vahdati, and M Imregun. Aeroelasticity analysis of air-riding seals for aero-engine applications. *TRANSACTIONS-AMERICAN SOCIETY OF MECHANICAL ENGINEERS JOURNAL OF TRIBOLOGY*, 124(3):607–616, 2002.

[71] Andras Z Szeri. *Tribology: friction, lubrication, and wear*. McGraw-Hill, 1980.

[72] V Castelli and J Pirvics. Review of numerical methods in gas bearing film analysis. *Journal of Lubrication Technology*, 90(4):777–790, 1968.

[73] Henk Kaarle Versteeg and Weeratunge Malalasekera. *An introduction to computational fluid dynamics: the finite volume method*. Pearson Education, 2007.

[74] David C Wilcox et al. *Turbulence modeling for CFD*, volume 2. DCW industries La Canada, CA, 1998.

[75] Philipe R Spalart, Steven R Allmaras, et al. A one equation turbulence model for aerodynamic flows. *RECHERCHE AEROSPATIALE-FRENCH EDITION-*, pages 5–5, 1994.

[76] CD Argyropoulos and NC Markatos. Recent advances on the numerical modelling of turbulent flows. *Applied Mathematical Modelling*, 39(2):693–732, 2015.

[77] PR Spalart, WH Jou, M Strelets, SR Allmaras, et al. Comments on the feasibility of les for wings, and on a hybrid rans/les approach. *Advances in DNS/LES*, 1:4–8, 1997.

[78] Brian Edward Launder and Dudley Brian Spalding. The numerical computation of turbulent flows. *Computer methods in applied mechanics and engineering*, 3(2):269–289, 1974.

[79] Dieter Forster, David R Nelson, and Michael J Stephen. Large-distance and long-time properties of a randomly stirred fluid. *Physical Review A*, 16(2):732, 1977.

[80] Victor Yakhot and Steven A Orszag. Renormalization group analysis of turbulence. i. basic theory. *Journal of scientific computing*, 1(1):3–51, 1986.

[81] FR Menter. Zonal two equation k-omega turbulence models for aerodynamic flows, 1993. AIAA-93-2906.

[82] FR Menter, M Kuntz, and R Langtry. Ten years of industrial experience with the sst turbulence model. *Turbulence, heat and mass transfer*, 4(1):625–632, 2003.

[83] Andrea Bristot, Hervé P. Morvan, and Kathy A. Simmons. Evaluation of a volume of fluid cfd methodology for the oil film thickness estimation in an aero-engine bearing chamber. Number 49712 in 10.1115/GT2016-56237, page V02CT39A007. Proceedings of ASME Turbo Expo 2016: Turbomachinery Technical Conference and Exposition, Seoul, South Korea, 2016.

[84] Alexander O Pugachev, Ulrich Kleinhans, and Manuel Gaszner. Prediction of rotor-dynamic coefficients for short labyrinth gas seals using computational fluid dynamics. *Journal of Engineering for Gas Turbines and Power*, 134(6):062501, 2012.

[85] Gilles Roy, Iulian Gherasim, François Nadeau, Gérard Poitras, and Cong Tam Nguyen. Heat transfer performance and hydrodynamic behavior of turbulent nanofluid radial flows. *International Journal of Thermal Sciences*, 58:120–129, 2012.

[86] M Angioletti, E Nino, and G Ruocco. Cfd turbulent modelling of jet impingement and its validation by particle image velocimetry and mass transfer measurements. *International Journal of Thermal Sciences*, 44(4):349–356, 2005.

[87] ANSYS Inc. Ansys r16.1, cfx user manual, 2016.

[88] ANSYS Inc. Ansys r16.1, engineering data, 2016.

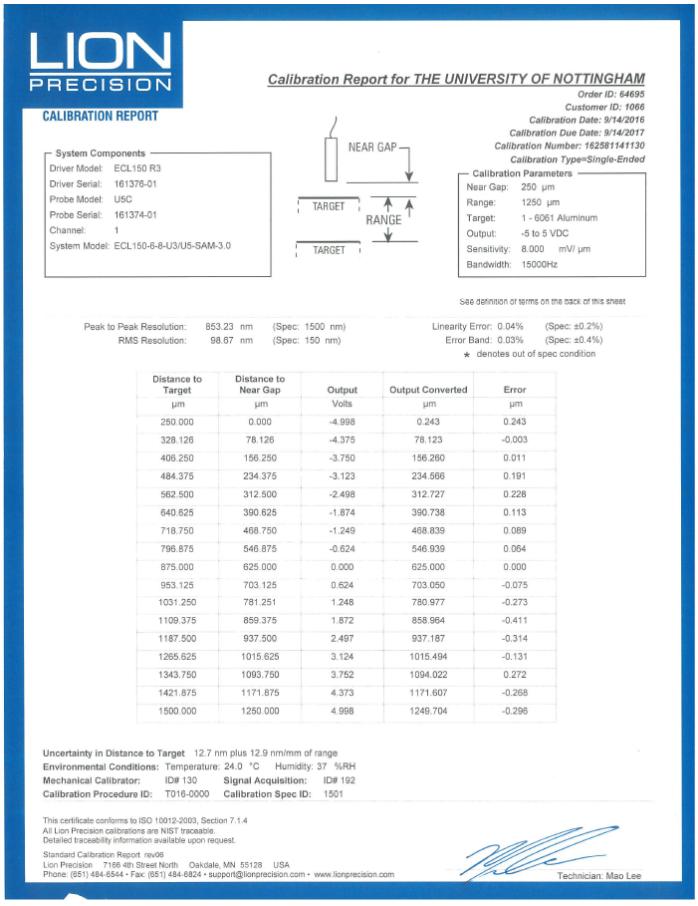
[89] Hyspan Bellows. Series 7500 formed metal bellows catalog 974c, September 2017. [online] http://www.hyspanbellows.com/pdfs/BellowsCatalog.pdf.

[90] Constanza Ahumada Sanhueza, Andrea Bristot, Shubham Kumar, Nicolas Schneider, Seamus Garvey, and Herve Morvan. An integrated system's approach towards aero engine subsystems design. Technical report, SAE Technical Paper, 2016.

[91] Michael I Friswell. *Dynamics of rotating machines*. Cambridge University Press, 2010.

Appendix A

Appendix



LION PRECISION

CALIBRATION REPORT

Calibration Report for THE UNIVERSITY OF NOTTINGHAM

Order ID: 64695
Customer ID: 1066
Calibration Date: 9/14/2016
Calibration Due Date: 9/14/2017
Calibration Number: 162581141130
Calibration Type=Single-Ended

System Components

Driver Model: ECL150 R3
Driver Serial: 161376-01
Probe Model: U5C
Probe Serial: 161374-01
Channel: 1
System Model: ECL150-6-8-U3/U5-SAM-3.0

Calibration Parameters

Near Gap: 250 µm
Range: 1250 µm
Target: 1 - 6061 Aluminum
Output: -5 to 5 VDC
Sensitivity: 8.000 mV/ µm
Bandwidth: 15000Hz

See definition of terms on the back of this sheet

Peak to Peak Resolution: 853.23 nm (Spec: 1500 nm)
RMS Resolution: 98.67 nm (Spec: 150 nm)

Linearity Error: 0.04% (Spec: ±0.2%)
Error Band: 0.03% (Spec: ±0.4%)
* denotes out of spec condition

Distance to Target µm	Distance to Near Gap µm	Output Volts	Output Converted µm	Error µm
250.000	0.000	-4.998	0.243	0.243
328.126	78.126	-4.375	78.123	-0.003
406.250	156.250	-3.750	156.260	0.011
484.375	234.375	-3.123	234.566	0.191
562.500	312.500	-2.498	312.727	0.228
640.625	390.625	-1.874	390.738	0.113
718.750	468.750	-1.249	468.839	0.089
796.875	546.875	-0.624	546.939	0.064
875.000	625.000	0.000	625.000	0.000
953.125	703.125	0.624	703.050	-0.075
1031.250	781.251	1.248	780.977	-0.273
1109.375	859.375	1.872	858.964	-0.411
1187.500	937.500	2.497	937.187	-0.314
1265.625	1015.625	3.124	1015.494	-0.131
1343.750	1093.750	3.752	1094.022	0.272
1421.875	1171.875	4.373	1171.607	-0.268
1500.000	1250.000	4.998	1249.704	-0.296

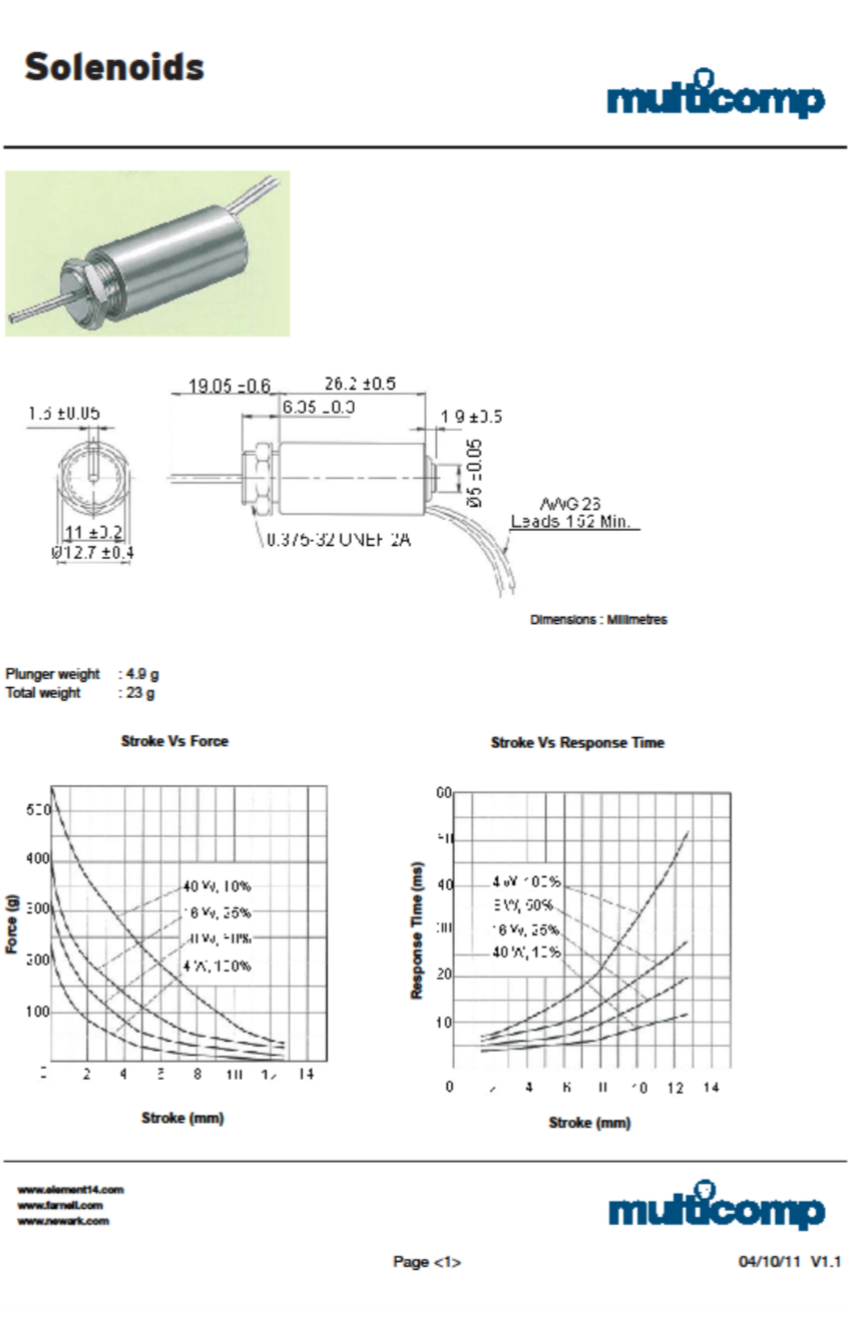
Uncertainty in Distance to Target 12.7 nm plus 12.9 nm/mm of range
Environmental Conditions: Temperature: 24.0 °C Humidity: 37 %RH
Mechanical Calibrator: ID# 130 **Signal Acquisition:** ID# 192
Calibration Procedure ID: T016-0000 **Calibration Spec ID:** 1501

This certificate conforms to ISO 10012-2003, Section 7.1.4
All Lion Precision calibrations are NIST traceable.
Detailed traceability information available upon request.

Standard Calibration Report rev06
Lion Precision 7166 4th Street North Oakdale, MN 55128 USA
Phone: (651) 484-6544 • Fax: (651) 484-6824 • support@lionprecision.com • www.lionprecision.com

Technician: Mao Lee

Fig. A.1 Sensor specification data



Solenoids

multicomp

19.05 ±0.6
26.2 ±0.5
6.35 ±0.3
1.9 ±0.5
1.5 ±0.05
Ø5 ±0.05
11 ±0.2
Ø12.7 ±0.4
AWG 23
Leads 152 Min.
0.375-32 UNEF 2A

Dimensions : Millimetres

Plunger weight : 4.9 g
Total weight : 23 g

Stroke Vs Force

Force (g)
500
400
300
200
100
40 W, 10%
8 W, 35%
4 W, 100%
2 4 6 8 10 12 14

Stroke (mm)

Stroke Vs Response Time

Response Time (ms)
60
40
20
10
0 4 6 8 10 12 14

Stroke (mm)

www.element14.com
www.farnell.com
www.newark.com

multicomp

Page <1>

04/10/11 V1.1

Fig. A.2 Solenoid Specification